Periodic surface-morphologies through temporal modulating the drying rate during evaporation of colloidal suspensions.

Essa Shawail

THÈSE

Pour obtenir le grade de

DOCTEUR DE L'UNIVERSITÉ GRENOBLE ALPES

Spécialité : 2MGE : Matériaux, Mécanique, Génie civil, Electrochimie

Arrêté ministériel : 25 mai 2016

Présentée par

Essa SHAWAIL

Thèse dirigée par **Yahya RHARBI**, chargé de recherches

préparée au sein du **Laboratoire Rhéologie et Procédés** dans **l'École Doctorale I-MEP2 - Ingénierie - Matériaux, Mécanique, Environnement, Energétique, Procédés, Production**

Structuration périodique de la surface par séchage modulé dans le temps d'une suspension colloïdale

Periodic surface-morphologies through temporal modulating the drying rate during evaporation of colloidal suspensions.

Thèse soutenue publiquement le **2 mars 2021**, devant le jury composé de :

Monsieur YAHYA RHARBI
CHARGE DE RECHERCHE HDR, CNRS DÉLÉGATION ALPES, Directeur de thèse
Monsieur MICKAEL ANTONI
PROFESSEUR DES UNIVERSITES, UNIVERSITE AIX-MARSEILLE - MEDITERRANEE, Rapporteur
Monsieur JACQUES LENG
CHARGE DE RECHERCHE HDR, CNRS DÉLÉGATION AQUITAINE, Rapporteur
Madame NADIA EL KISSI
DIRECTRICE DE RECHERCHE, CNRS DÉLÉGATION ALPES, Présidente

Acknowledgments

To the immortal soul of my father and my family I dedicate this thesis. First of all, I would like to thank my thesis supervisor, Yahya Rharbi, for the trust and the support he has given me during his supervision of my thesis. I thank him warmly for his advice and encouragement in difficult times. As well as for the wonderful guidance he has given me throughout this work. I also address my warmest gratitude to the members of the jury who evaluated this thesis work, Professor MICKAEL ANTONI, Professor at Aix-Marseille Univ, CNRS, MADIREL, Dr. Jacques LENG, Researcher at CNRS at Laboratoire du Futur, and Dr. Nadia El Kissi, Research Director at Laboratoire Rheologie et Procedes in Grenoble. I would also like to thank Mr. Frédéric Bossard, director of the Rheology and Processes Laboratory in Grenoble. I also extend my deep gratitude to the Libyan embassy. I would like also to mention the great pleasure I had to work within the LRP and I thank all the members, particularly the administrative team: François, Sylvie and Louise for their welcome, their permanent smiles which gave me encourage. I would like also to thank all the members of the technical team Mrs. H. Galliard, Dedi, Eric, Mohamed and Fréderic for their help. A big thanks also to Mr. Albert Magnin, Director of Research at Laboratoire Rheologie et Procedes in Grenoble. A big special thank you for Youness Soumane and Hajar Mamad for their help "thank you my brothers". Finally, thanks to all the members of Laboratoire Rheologie et Procedes in Grenoble.

Abstract

The fabrication of ordered morphologies by drying colloidal suspensions is a challenge for many emerging technologies. These structures can be achieved by directed convective-assembly leading to controlled particle deposition at the drying front. In this work, we propose a user-friendly method based on convective assembly for generating periodic surface morphologies through time-modulating the evaporation rate. We show that the advancing and arrest of the drying front can be tuned through the variation of the evaporation rate in certain colloidal suspensions, and we demonstrate that this mechanism can be used to govern particle deposition on demand. Periodic surface structures are made in polystyrene, polybutylacrylates suspensions, and their blends using this method. A model was developed to predict these structures by taking into consideration the dynamic of the drying front as well as the mechanism of particle deposition. The roles of surfactant, ionic strength, and particle size on surface periodicity were also investigated. We show that adding aliquots of SDS surfactant drastically affects both the dynamic of the drying front and the resulting surface morphologies.

Résumé

La fabrication de morphologies ordonnées par évaporation de suspensions colloïdales est un défi pour de nombreuses technologies émergentes. Ces structures peuvent être obtenues via un assemblage convectif dirigé conduisant à un dépôt de particules contrôlé au front de séchage. Dans ce travail, nous proposons une méthode conviviale basée sur l'assemblage convectif pour générer des morphologies périodiques de surface en modulant dans le temps le taux d'évaporation. Nous montrons que l'avancée et l'arrêt du front de séchage peuvent être réglés par la variation du taux d'évaporation dans certaines suspensions colloïdales, et nous démontrons que ce mécanisme peut être utilisé pour régir le dépôt de particules à la demande. Des structures de surface périodiques sont réalisées par une vitesse de séchage modulée dans le temps dans des suspensions de polystyrène et de polybutylacrylates et leurs mélanges. Ces structures ont été prédites via un modèle prenant en compte la dynamique du dépôt de particules et du front de séchage. Les rôles du surfactant, de la force ionique et de la taille des particules sur la périodicité de surface ont également été étudiés. Nous montrons que l'ajout d'aliquotes de surfactant SDS affecte considérablement la dynamique du front de séchage sous une vitesse de séchage modulée ainsi que les morphologies de surface résultantes.

Contents

Chapter 1

General introduction and Literature review

Contents

1.1 General introduction

Making periodic surface structures in polymer films is a critical step for numerous emerging technologies like microelectronics [1], photonics band-gap [2], optical components [3], self-cleaning surfaces [4], inkjet printing [5], coating [6], chemical and biosensors [7], data storage [8], solar energy [9], nanotechnology and medical diagnostic techniques [10], lab-on-ship [11]. Thus numerous surface patterning methods were investigated for making periodic structures like lithography [12], controlled printing [13], chemical modification of the surface [14], controlled drying [15], electrostatic deposition [16], spin-coating [17], Langmuir-Blodgett [18], fingering instabilities [19], spontaneous dewetting [20] and Self -Assembly, Transfer, and Integration [21], ect. Evaporation of colloidal suspensions was also suggested as a promising method in this field. Motivated by its

high application potential, it gathered attention from numerous research groups during the last few decades, leading to several derived methods: dip coating [22, 23], or stick slip during dip coating [24, 25], colloids self assembly [26–30], template-directed colloidal self-assembly [31–33], controlled doctor blade movement [34, 35].
Yet, beyond its apparent simplicity, this process involves challenging tasks since it requires meticulous control of colloidal deposition at targeted locations via controls of all physical aspects involved throughout the drying mechanism. Indeed, drying colloidal suspensions involves several synergic effects such as colloidal interactions [36], colloidal dynamics, aggregation and flocculation [37, 38], matter transfer [39], heat transfer [40], in-plane and out of plane concentration gradient [41], thermal and solutal Marangoni effects [42, 43], surface effects [44], adhesion [45], slippage [46, 47]. These nested aspects make drying colloidal suspension a complex process, which is still not fully understood. Therefore, comprehending all these aspects can provide a significant breakthrough for making periodic surface morphologies by design.
Concentration heterogeneities during drying is one of the critical aspects of structure making by evaporation. Indeed, when solvent evaporates the colloidal concentration increases heterogeneously leading to both vertical and in-plane concentration profiles [41]. The vertical concentration gradient can generate solutal Marangoni effect which adds up to the thermal one resulting from temperature gradient due to surface cooling during water evaporation [40, 42, 43] yielding surface patterns [48]. Drying rate in sessile drops or small film is usually higher on the drop border. Witten et al. [39] have shown that because the drying rate is higher at the triple line, capillary flow induces particle displacement and accumulation at the triple line leading to coffee ring effect as well as a radial displacement of the triple line from the border to the center. The details of the triple line dynamic during drying can be described by the capillary flow and the horizontal gradient of evaporation rate [41]. The effects of different parameters on the triple line dynamics have been investigated including the surface roughness [49], chemical heterogeneities of the surface [50], capillary pressure, surface-tension gradients, wetting forces and thin-film viscous forces [51].
Yet, controlling and tuning on demand the dynamic of the triple line is not trivial, particularly the moving and arrest mechanisms. Therefore, the challenge in this field is to control the movement and the arrest of the drying front on-demand to generate well ordered structures. Thus few methods were suggested to achieve this like dip coating in the stick slip condition, Doctor blade, lithographic mask. All these convective methods exploit the convective flow imposed by evaporation to drive the particles towards the drying front where they accumulate. For example, dip coating with either liquid [52] or substrate withdrawal [24] or doctor blade [34, 53], leads either to uniform or structured surfaces depending on the drying regime. In both Landau-Levich and capillary regimes [54], uniform films with modulated thickness can be achieved by controlling evaporation rate, triple line speed, the suspension and substrate properties.

The triple line can undergo a stick-slip mechanism at a certain conditions within the capillary regime of the dip coating leading to ordered structures [24, 25]. This results from the balance between capillary flow which brings the fluid towards the triple line and the capillary forces which controls the line retraction [25]. Periodic surface structure can be also achieved by controlled triple line displacement via periodic movement of doctor blade [35] or by using a lithographic mask bearing an array of holes [55]. Though these processes can produce ordered structures at small scales, they require meticulous technical conditions, which could handers their potential to become viable large scale industrial processes. Therefore, it remains a need for a technique to produce ordered surface morphologies using less critical conditions.

This work proposes a fast and simple method for producing ordered surface morphologies via evaporating polymeric colloidal suspensions by time modulating the drying rate. The moving and the arrest of the drying front can be tuned on demand using time modulated drying rate in controlled physical chemistry conditions. This was found to yield a fine control of the moving and arrest of the drying front and consequently the magnitude of particle deposition in each regime. This process can take place for different types of colloidal particles such as polystyrene, poly-butylacrylate and their blends. The dynamic of the drying front is monitored in the different drying regimes and correlated with surface morphologies. A simple drying model was developed to account for the observed surface morphology by taking into account the dynamic of the drying front under periodically modulated drying rate. The general tendency of the observed moving and arrest of the drying front and the resulting surface morphologies were predicted using such model. The roles of surfactant, ionic strength and particle size on surface periodicity were also investigated. We have studied how these parameters affect the drying front dynamic as well as the resulting surface morphologies under a modulated drying rate.

This thesis is divided into four chapters:

1. In the first chapter, we give an overview of the literature on drying colloidal suspensions, triple line dynamics and we describe some techniques used to control particle deposition during drying.

2. In the second chapter, we describe:(i) The synthesis procedure of the polymer suspensions used in this thesis including polystyrene, polybutylacrylates. (ii) The cleaning methods of the suspension and the characterization procedures of the particles were described: the dynamic light scattering (DLS) to measure the particle size , (Differential Scanning Calorimetry - DSC) to measure the glass transition temperature and conductimetry titration to quantify the number of sulfate groups at the surface of the particles. The particle surface characterisation was also described including zeta potential.(iii) The drying system used to generate the periodic drying rate was described. (iv) Finally, the methods for the morphological characterization of the films were presented.

3. In the third chapter, we present a user-friendly method based on convective assembly for generating periodic surface morphologies through time-modulating the evaporation

rate. We show that the advancing and the arrest of the drying front can be tuned by the variation of the evaporation rate in certain colloidal suspensions, and we demonstrate that this mechanism can be used to govern particle deposition on demand. Periodic surface structures are made by time-modulated drying rate in polystyrene and polybutylacrylates suspensions and their blends. These structures were predicted via a model that takes into consideration the dynamics of the particle deposition at the drying front. Furthermore, we investigate the effect of particle size, and concentration on the formation of the periodic patterns during drying.

4. In chapter Four, the roles of surfactant on the dynamic of the drying front and the resulting 3D surface morphology was investigated. We show that adding aliquots of sodium dodecyl sulfate (SDS) affects the drying front dynamic under a modulated drying rate as well as the resulting surface morphology. The patterns period was found to decrease with increasing [SDS] and exhibit the same tendency as the surface tension. Furthermore, the onset and the first line of drying front was found to advance with a velocity, which decrease with increasing [SDS]. On the other, the second line of the drying front was found to advance rapidly during airflow and recedes back to the onset line once the airflow stops. These dynamics were found to follow a similar tendency of the surface tension which suggests that the surface tension plays a significant role in this process. In this chapter also, we explore the role of salt (potassium chloride, KCl) on the formation of the periodic patterns. In particular, we want to understand how the screening of electrostatic repulsions between particles affects the particle deposition under the periodic airflow.

1.2 Literature review studies

1.2.1 Drying and thin film formation

Drying a film of colloidal suspensions or polymer solution yields solid film. This process is central for a wide spectrum of applications in everyday life and plays a crucial role in many industrial technologies such as buildings, automobiles, nanotechnology, electronic components, photovoltaic cells, wear and corrosion protection, optical components, self-cleaning surfaces etc. One of the major use of films formation through solvent drying is in coating technologies such as architectural or automotive. These films should have an ideal surface structure in order to enhance their durability and prevent dirt and biofilm accumulation. Therefore, these applications require meticulous manufacturing conditions in order to develop controlled surface quality with a specific visual aspect.
Even if film formation by drying is an ancient process it remains a scientific challenge and involves numerous physical mechanisms and generates wide spectrum of film morphologies [56]. It is a complex process which depends on several interconnected parameters such as (i) drying kinetic, (ii) the rheology of the polymer or the colloidal particles (hard or soft), (iii) the conditions and the geometry of drying, (iv) the structure and the aggregation of the particles or polymer chains throughout the consolidation process etc [57, 58]. The drying kinetic during film formation from concentrated suspension is composed of two regimes (Figure 1.1): (1) the evaporation rate is constant in first drying period because the particles does not strongly influence the solvent diffusion within the film and consequently the evaporation rate is mainly dominated by the solvent diffusion coefficient and the vapor pressure [59].

$$J \sim D_s C_{sat} \tag{1.1}$$

Where C_{sat} is the saturated water vapor pressure, D_s is water diffusion coefficient in air. (2) When the particle concentration becomes important, solvent diffusion is reduced due to tortuously and to the eventual formation of top skin, which leads to reduction of the evaporation rate [60].

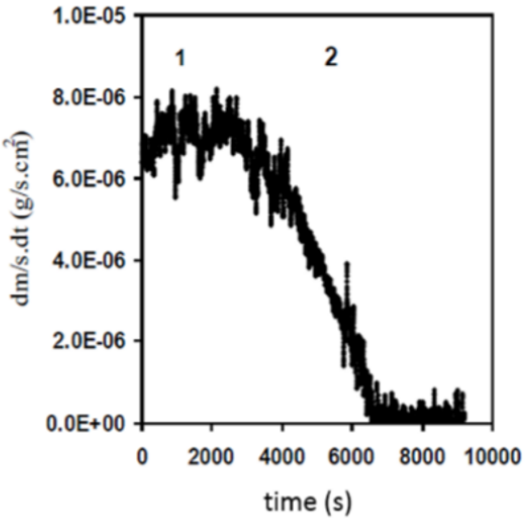

Figure 1.1: Drying kinetics of colloidal suspension. (1) The drying rate is constant. (2) The drying rate is decreasing. Figure taken from Ref. [67].

Depending on the material properties and the drying conditions, drying colloidal suspensions or polymer solution yields various surface morphologies such as wrinkling, buckling, corrugation, cracking or delamination. For example hard colloidal suspensions such as silica or glassy latex yields periodic cracks and delamination, while soft particles generates crack-free films [61, 62]. This mechanism is important for water born coating technology where uniform and crack free polymer films are made by drying latex suspension. In this case when the suspension is dried below the particles glass transition temperature T_g, cracks dominate the film because particles can not deform to close the menisci between them (Figure 1.2) which generates large capillary stresses on the film free surface which causes the film to crack and delaminates (Figure 1.3). This problem has been the subject of several publications by Allain et al [63], Routh et al [64], Pauchard et al [65]. On the other hand, when drying latex suspensions above T_g, the particles deforms leading to stress relaxation which inhibits craks formation. Generally, film formation from colloidal particles is regarded as a mechanical problem with three stages: concentration, particle deformation, coalescence (Figure 1.4) [58, 60].

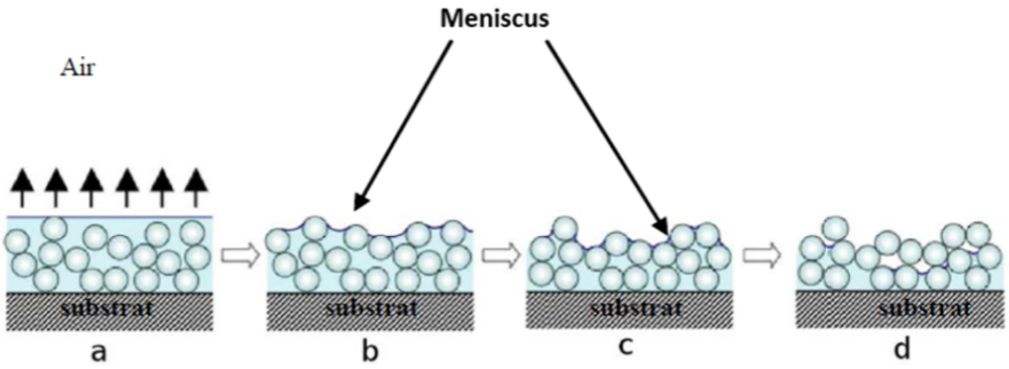

Figure 1.2: The film formation phases: (a) Loss of water by evaporation. (b) Appearance of meniscus at the gel-air interface and particle concentration. (c) Beginning of gel consolidation. (d) Decrease in the amount of solvent penetration of the meniscus into the structure [66]

.

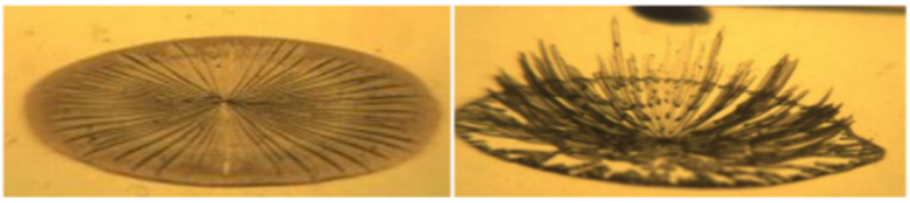

Figure 1.3: Images show cracks and delamination in polmer films.[67]

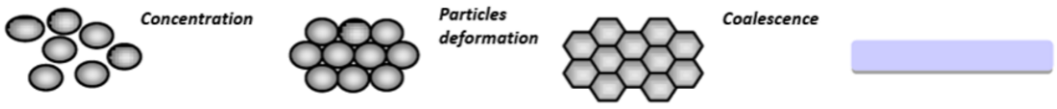

Figure 1.4: Diagram illustrates the three stages of film formation by drying soft particles.

Even if the film does not crack or delaminate in the case of soft particles or polymer solution, surface corrugation can appear in certain drying conditions. For example Guerrier et al [56] investigated the surface corrugations during drying the Polyisobutylene PIB / toluene solutions (Figure 1.5). Pauchard and Allain [68] explained the corrugated surface by mechanical instabilities model. They proposed that the fast drying yields a dry skin on the film surface, which buckles once the solvent underneath evaporates. On the other hand, Bassou et al [48] studied the mechanisms leading to surface corrugation during the free surface evaporation of polystyrene in toluene solutions. They found that the drying of solvent from polystyrene/toluene solutions leads to well-ordered corrugated patterns with wavelength increasing linearly with increasing film thickness (Figure 1.6). They attributed this to the solutal Marangoni effect.

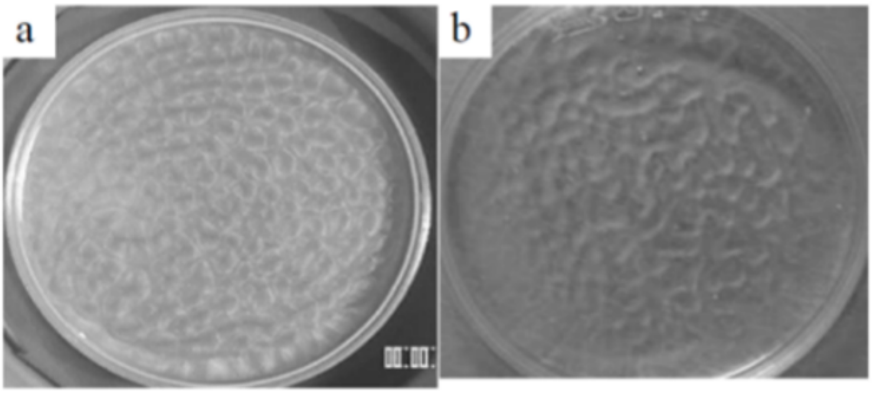

Figure 1.5: a) Cell development convective during the drying of a PIB / toluene solution. b) Surface folds observed at the end of the drying PIB / toluene solution [69].

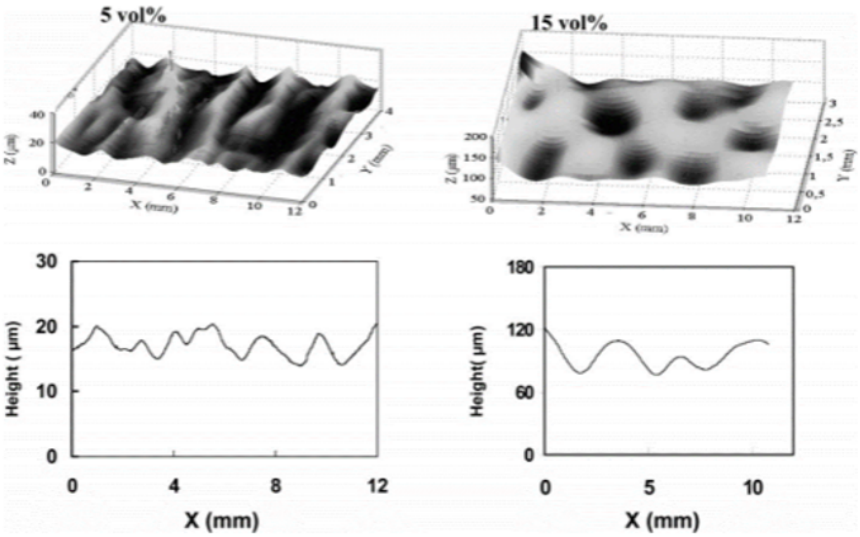

Figure 1.6: (Top) Three-dimensional morphology profiles of the surface corrugation of films prepared by the evaporation of polystyrene in toluene solutions at 5 and 15 vol %. (Bottom) Two-dimensional profiles of surface corrugation of films prepared by the evaporation of polystyrene in toluene solutions at 5 and 15 vol %. Images taken from Ref [48].

1.2.2 Drying sessile drop of colloidal suspension

The last few decades have seen a recrudescence of studies dealing with drying small sessile drop thanks to the richness of the physical mechanisms occurring in this geometry, to the morphological diversity of dried film as well as their application potential. Indeed drying sessile drop involves additional physical aspects to the film formation due to the triple line singularity (suspension/air/solid) and therefore several aspects of film formation were revisited due to this singularity i) drying kinetic, ii) flux and matter transfer, iii) concentration gradient, iv) wetting, v) surface structuration [70]. The triple line singularity affects primarily the drying kinetic. While the mass loss in large film is proportional to the surface area and dominated with diffusion coefficient and vapor pressure

$$J \sim A D_s C_{sat} \tag{1.2}$$

Where C_{sat} is the saturated water vapor pressure, D_s is water diffusion coefficient in air and A is the surface area of the film. The presence of triple line singularity change drastically the drying kinetic and generate lateral gradient of drying rate. It was suggested that the mass loss is infinite at the triple line and decreases while approaching the drop

center. This can be described by using [39]

$$J \sim \frac{1}{(R-r)^{\lambda}} \tag{1.3}$$

Where R is the drop radius and r is the radial position in the drop. Experimentally the drying rate measured gravemetrically can give some hints about the radial dependence of the drying rate [71]. Averaging the drying rate over all the surface area, leads to an average value dependent on the drop radius instead of the drop surface area.

$$J \sim D_s C_{sat} R \tag{1.4}$$

Where R is the drop radius.
The drying mechanisms of sessile drops were investigated few decades ago in order to understand the physics of the triple line dynamic [72]. One early study proposed several drying modes [72]: (i) The constant contact radius (CCR) mode, where the triple line is immobilized and remains constant while the contact angle decreases.(ii) The constant contact angle (CCA) mode, where the contact angle remains constant and the triple line shrinks towards the center. In fact, drying sessile drop is more complex because the lateral drying rate gradient can lead to a concentration gradient and consequently to a lateral flux and matter transfer. The interest in such a physical process has drawn a wide interest since Deegan et al [39] published their famous work on the coffee ring. They have shown that because the drying rate is higher at the pinned triple line, the solvent moves from the centre of the drop towards the droplet edge (Figure 1.7). Eventually, the particles are driven towards the pinned triple line imposed by the capillary flow and causes the accumulation of particles there leading to coffee ring effect (Figure 1.8). The understanding of this process can provide physical insights about the underlying mechanism of droplet evaporation which is important for several applications. Therefore, numerous studies have been carried out in order to explain the dynamic of the pinning and depinning [73–80].
The triple line dynamic was found to be enhanced by the surface wettability and contact angle hysteresis (CAH)[81]. Orejon et al [82] found that increasing the particles concentration prolonged the pinning duration. The balance between pinning and depinning forces has also been investigated [82, 83].

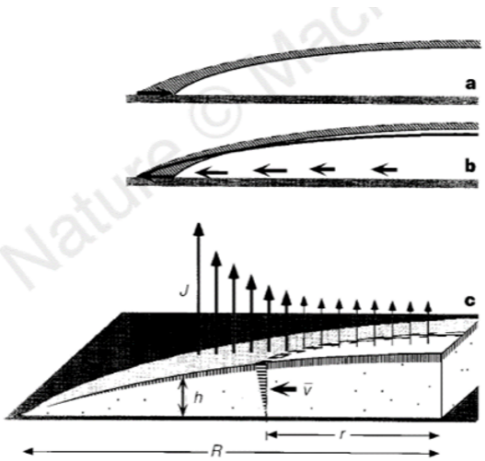

Figure 1.7: Mechanism of drying.(a) the border moves towards the center. (b) outward flow dominates as the triple line pinned. (c) defines the quantities responsible for flow. Images taken from Ref. [39].

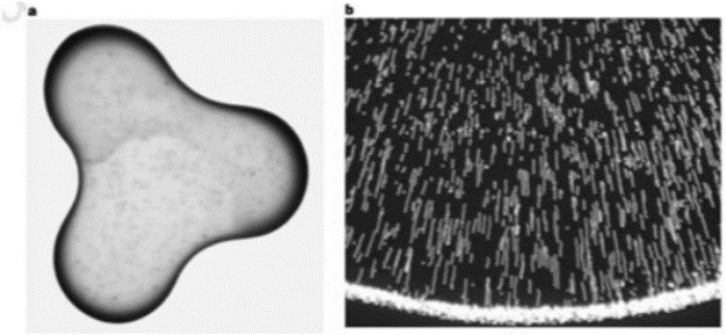

Figure 1.8: Migration of particles towards the pinned triple line during coffee drop evaporation. Image modified from Ref. [39].

The nature of substrates was found to play an important role in the dynamic of the triple line [84–87]. Indeed, drying of a droplet on the hydrophilic surface is attributed to the self-pinning phenomenon while drying on the hydrophobic surface exhibits three distinct stages: constant contact area, constant contact angle, and mixed stage [39, 88–90]. Surface roughness can also influence the surface morphology of the dried film [87]. The heating or cooling of the substrate was found to generate different surface morphologies. Drying at room temperature or heated surface leads to strong capillary flow resulting in coffee ring patterns. However, a cooled substrate generates Marangoni flow resulting in reverse particles deposition [91]. Hu and Larson [42, 92] have shown

that the flow inside the droplet can affect the drying process mechanism. They reported that Marangoni flow generated by the surface tension gradient during evaporation can reverse the flow towards the center resulting in particles deposition at the central region (Figure 1.9) [42]. Xu and Luo [40] have shown that rapid drying reduces the temperature at the triple line, which results in a temperature gradient, leading to Marangoni eddy flow.

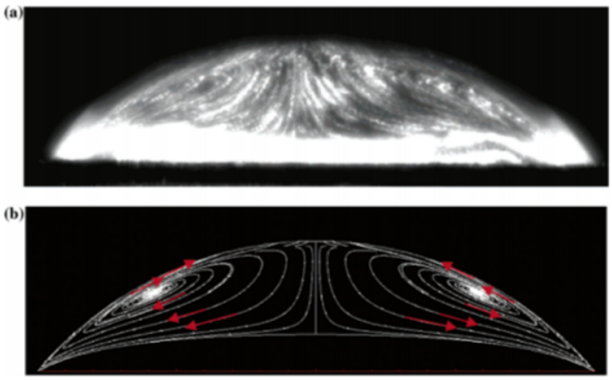

Figure 1.9: Marangoni flow during drying octane droplet, (a) experimental results and (b) bottom is the analytical solution. Images taken from Ref [42].

The particle interactions during the different consolidation stages, drastically affect the drying process of the sessile drop. Indeed, the combinations of both the attractive van der Waals and the repulsive electrostatic forces between particles can play a dominant role in inducing particles stability. This scenario becomes even more complex with the presence of solvents, salt, surfactant etc [93–95]. Bhardwaj et al [36] modified the particle-particle and particle-substrate interactions by varying the solution pH and investigated their effect on the dried surface morphology. They found a uniform deposition patterns at low pH and they attributed it to the attractive interaction between the particles and the substrate. At medium pH, they found random particle deposition and attributed it to the fragile interaction between the particles and substrate. At high pH, they observed ring-like-pattern and correlated it to the strong particle-substrate repulsive interaction. The effect of multiple particle sizes on the surface morphology of the dried film has also been investigated. Jung et al [96] found that during drying colloidal suspensions containing different particles sizes, the small particles move towards the triple line while the large particles move to the center. Wong et al [97] investigated the drying mechanism of drops containing three different particles size. They observed three separate rings at the triple line where the smaller one deposit at the outer ring and the bigger one in the inner ring. Lee et al [98] have shown that increasing the particles concentration and particles size lead to uniform surface structure, while the low concentration with small particle size lead to coffee ring .

1.2.3 Drying front in sessile drop.

When drying concentrated solution of sessile drop, the triple line becomes the drying front, which is the interface between suspension/air/dried film. Routh and Russel [99] reported that the drying front is influenced by different parameters including dispersion viscosity, initial film thickness, and particle size as well as the surface tension. Another study has shown, that during the drying, two distinct fronts were observed [100]: a first front near the edge followed by a second front close to fracture front (Figure 1.10). They showed that if central region is flooded with water, the zone between the two fronts re-disperses, while, the material behind the second front remains solid. This explains that the first front corresponds to fluid zone and it is reversible, while the second front represents an aggregated irreversible zone. Kaplan and Mahadevan [101] proposed a model to understand the physical parameters that control the drying processes of sessile drop containing colloidal suspension. They investigated the dynamic of the drying front via a multiphase model to characterize the transition between rings and uniform deposition.

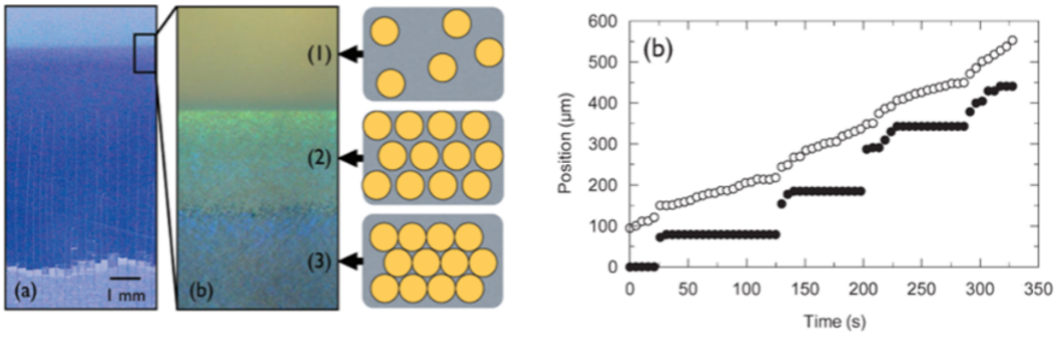

Figure 1.10: (Left) Evaporation profile of a colloidal suspension. (Right) appearance of the propagation of the drying fronts (○) = aggregation, (●) = fracture. Images taken from Ref [100].

1.2.4 Methods for making periodic surface structure during drying.

Making periodic surface morphologies on demand is crucial for many applications. For example, photonic band gaps which are regarded as one of the most interesting topics in various application such as a creation of high quality periodic dielectric structures in 2D or 3D, optical sensing, quantum optics, etc [102]. The self-cleaning surface that could be used in the diverse application including solar energy [103], smart devices [104], anti-fogging [105], etc. Controlling such structures require developing method to drive either the colloidal organisation on the substrate or to control particle deposition on demand. Integrating such process in large-scale fabrication requires meticulous technical

conditions, which could hinder their potential scale up to become a valuable industrial process. Thus, numerous surface patterning methods were proposed for making periodic structure.

1.2.4.1 Two-dimensional crystallization

Denkov et al [106] investigated the mechanism of particles deposition during drying large latex particles. They have shown that the particles are dragged to each other imposed by the capillary force, which acts between the particles as soon as the height of the liquid becomes lower than the diameter of the particles. This force drives the particles to assembly in the meniscus region leading to create the two-dimensional network (Figure 1.11).

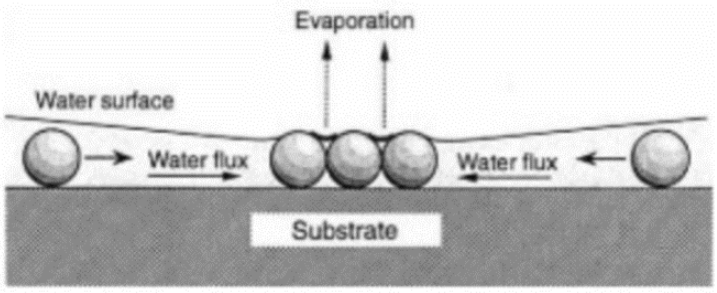

Figure 1.11: Diagram of particle assembly that driven towards the regions of faster evaporation by water flow. From Denkov [106].

Spin coating strategy was also investigated as a tool for controlling crystallisation of colloidal particles on a substrate [29, 107, 108]. This relies on controlling the spinning acceleration process during casting a thin film on a substrate. Chen et al [109] utilized this technique in order to generate ordered colloidal crystal film by using polystyrene PS particles with different size ranging from 200 nm to 1300 nm (Figure 1.12). Subsequently, as soon as the film thickness decreases below the particle size, capillary forces the particles together, yielding ordered structures. Many parameters can play a major role in this process, including viscosity, particle size, and the surface tension.

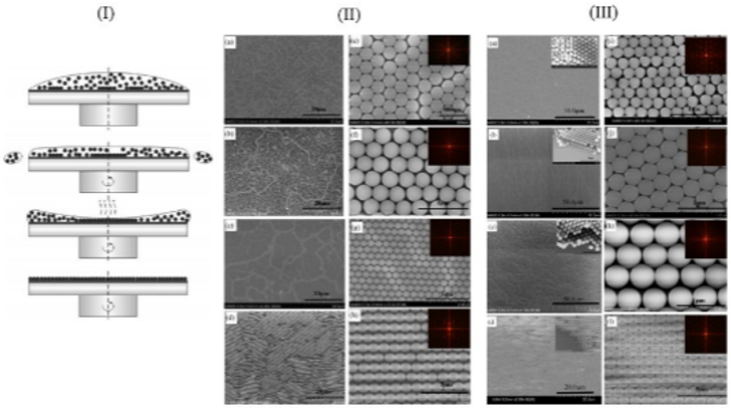

Figure 1.12: Exhibits: (I) Schematic illustration of procedure of colloidal crystal films structure. (II) Self assembly of PS particles with different diameter (a, e: 223 nm; b, f: 347 nm; c, g: 509 nm d, h: 1300 nm) in low (a–d) and high (e–h) magnification. (III) Structure of bilayer films with different diameter . ((a, e): 223 nm; (b, f): 347 nm; (c, g): 509 nm; (d, h): 1300 nm) in low (a–d) and high (i–l) magnification. Image adapted from Ref. [109].

1.2.4.2 Electrostatic and Electrophoretic directed assembly

Electrostatic directed assembly has been employed to organise charged particles on substrate using electrostatic forces [110]. Chen et al [111] investigated the deposition of charged particles by using patterned polyelectrolyte substrate. They managed to fabricate patterned arrays by applying the technique of self-assembly driven by electric-fields. Walker et al [112] reported that two coupled parameters namely, colloidal surface charge and ionic charge clouds can affect the nature of colloidal assembly in such a system. However, the complexity of this technique is caused by the high charges of particles which lead to a complicated process during deposit the particles on a substrate [29]. Teulon et al [16] used this approach to fabricate patterns of micrometer-sized particles via coupling electrostatic field and convective self-assembly (Figure 1.13). Their mechanism is based on moving a charged substrate at a constant speed and dragging a drop of a colloidal suspension within an immobilized blade. In such a process, the electrostatic repulsion and convective flow was found to play a significant role in the particles deposit.

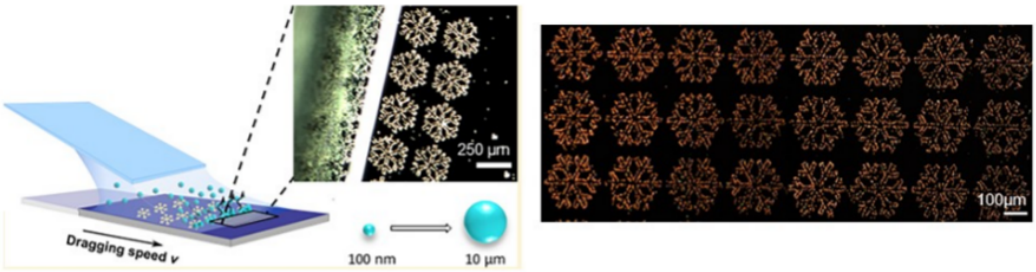

Figure 1.13: (Left) Schematic representation of electrostatic directed assembly process on charged patterns by convective flow. (Right) An optical image shows an example of directed assembly of $1\mu m$ latex particles on charged patterns using convective nanoxerography. Image modified from Ref. [16].

The electrophoretic deposition (EPD) strategy relies on the deposition of colloidal particles that migrate in a liquid onto an electrode under an electric field [113]. Tran et al [113] have established a rapid EPD process to fabricate the colloidal crystal film with aqueous ethanol (EtOH) colloidal suspension. The colloidal crystal of PS particles was fabricated on either indium tin oxide (ITO) coated glass (ITO/glass) or an ITO coated PET (polyethylene terephthalate) sheet (ITO/PET) which was used as substrate/anode and stainless-steel plate as the electrode/cathode. The electrodes were immersed in the colloidal suspension and withdrawn while applying to them an alternate current inducing the negatively charged PS particles to move towards the anode (Figure 1.14). Measurement of film thickness showed that the lower withdrawing rates lead to uniform EPD colloidal crystal film, however, increasing this rate lead to an inhomogeneous film (Figure 1.15).

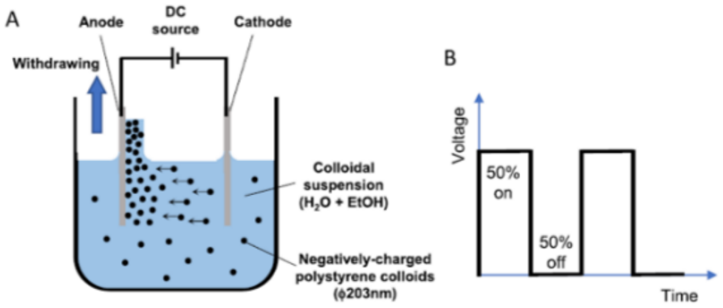

[h]

Figure 1.14: A: Schematic diagram of EPD process: Anode: ITO/glass or ITO/PET, and Cathode: Stainless steel sheet; B: Schematic of pulse voltage program. Images taken from Ref [113].

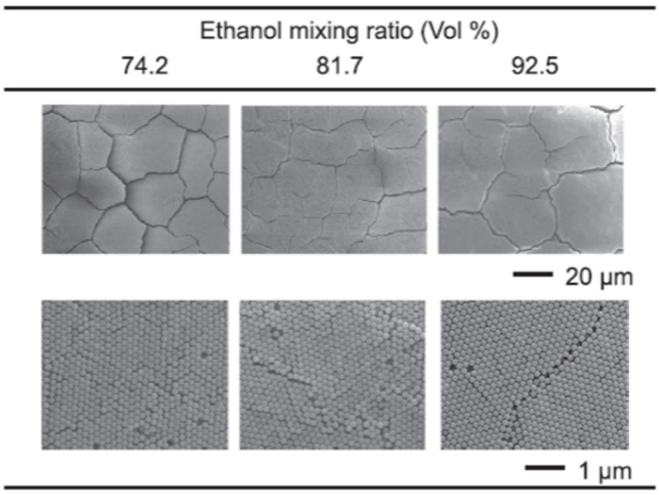

Figure 1.15: Surface SEM images of films obtained using EPD suspensions with different solvent ratios of EtOH and H2O with an applied voltage of 5 V/cm for 5 min. Images taken from Ref [113].

1.2.4.3 Langmuir-Blodgett assembly (ALB)

Designing well-ordered structure can be obtained by Langmuir-Blodgett Assembly. Li and Gilchrist [18] fabricated continuous multilayer structures of particles on substrate (Figure 1.16). The mechanism of the process is based on the balance between the viscous drag and capillary forces as well as control over the particles mass flow rate at slow speed and contact angle 20^0. The particles are driven towards the interface of the meniscus imposed by surface tension and are brought together by capillary forces resulting in thin film formation. The particle deposition is affected by the suspension volume fraction and suspension flow rate. Indeed, at a high drying rate, discontinuous multilayer deposition is resulted because of the flow instability and Marangoni flows as they noted.

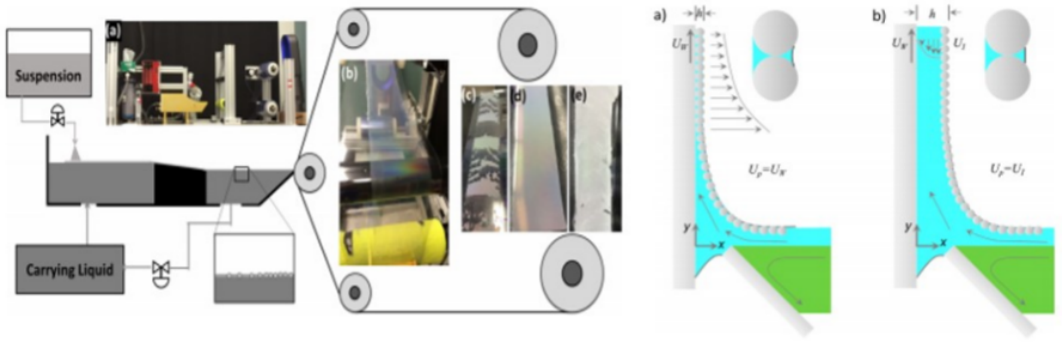

Figure 1.16: (Left) Diagram of ALB. Images of (a) ALB device, (b) films on the web, (c) discontinuous, (d) monolayer, and (e) multilayer. (Right) Mechanism of particles deposition onto the substrate. Image taken from Ref. [18].

1.2.5 Patterning of colloidal suspension via convective assembly.

The convective self-assembly has been applied as a facile and simple technique to create and control the particles deposition on a large scale. The strategy relies on driving the particles by the capillary flow towards the drying front where they accumulate.

1.2.5.1 Dip-coating

Dip coating is a feasible and scalable technique for generating large structured surface area [114]. One way to reach this is by immersing a substrate into suspension and withdraw it with a controlled velocity [22, 115, 116]. In such a process, several structures can be formed depending on the velocity, drying rate and properties of the suspension (Figure 1.17, 1.18 and 1.19) [23, 24, 54]. In general the film thickness strongly depend on the the substrate velocity (Figure 1.18) [54]. This comes from two different mechanisms namely, Landau-Levich regime for high withdraw velocity and capillary regime resulting from low withdraw velocity. Gans et al [23] observed and measured the average film thickness in the different coating regimes via varying the velocity of the substrate withdrawal as well as the volume fraction of the suspension (Figure 1.19). They have shown three different regimes: (i) At low withdrawal speed, there is almost no particles deposition. (ii) Increasing withdrawal speed leads to a large number of particles deposit on the coating regime however, the structure is not homogeneous. (iii) A higher withdrawal speed leads to a large thickness with a uniform structure.

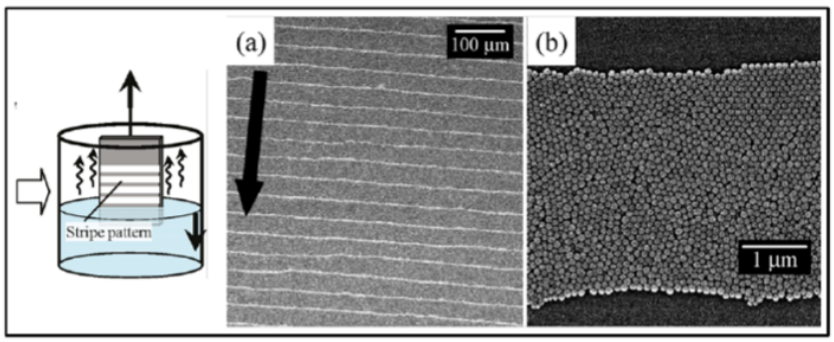

Figure 1.17: Periodic deposition of colloidal particles fabricated by dip-coating system on the glass substrate. Image taken from Ref. [24].

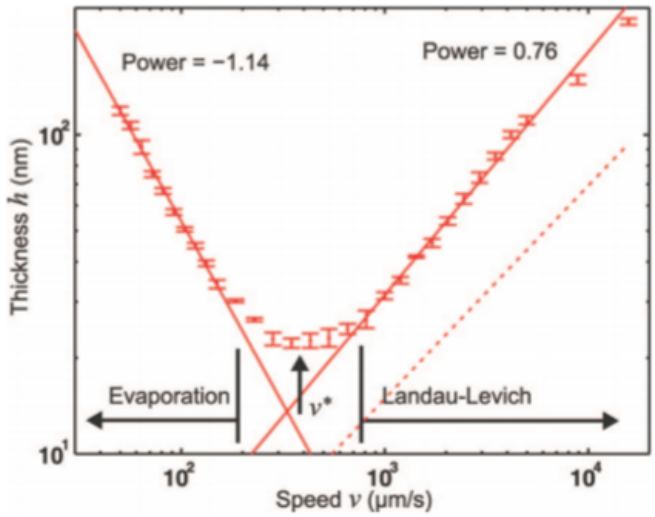

Figure 1.18: (v) shape curve - modulated film thickness as a function of substrate withdrawal in a dip-coating. Image taken from Ref. [54].

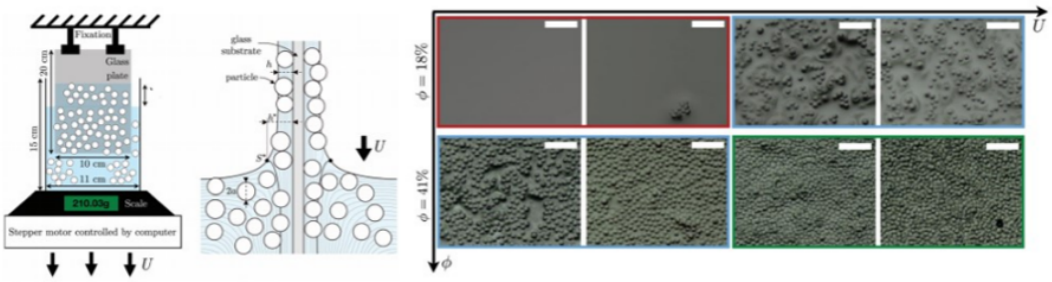

Figure 1.19: (Left) Schematic diagram of the formation procedure of dip coating. (Right) Images exhibit three different coating regimes depends on the withdrawal velocity U with $\phi = 18\%$ and $\phi = 41\%$ of PS particles of diameter 2a = 140 mm : liquid only (red), heterogeneous coating (blue) and multilayer of particles (green). Images adapted from Ref. [23].

1.2.5.2 Stick slip motion of the triple line

At low withdrawal velocity in the dip coating regime, stick-slip motion of the triple line could take place yielding a regular patterns on the substrate [82]. Such phenomenon results from the synergy between capillary flow which brings the fluid towards the drying front and the capillary forces which govern the triple line retraction. Bodiguel et al [25] investigated the stick-slip between two glass plates with the purpose of creating regular strips by pumping the particles suspension out of the reservoir under controlled temperature and humidity (Figure 1.20).

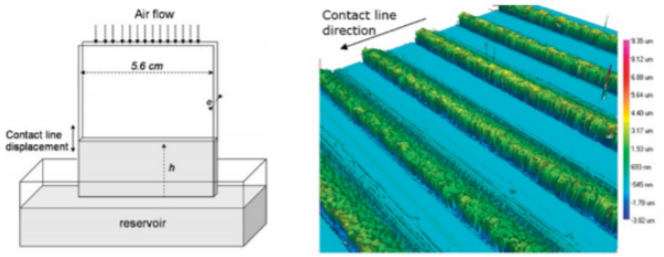

Figure 1.20: (Left) Schematic illustration of the experimental setup. (Right) The periodic structure obtained after the completion of drying under conditions of imposed average speed = 1 $\mu m/s$, particle volume fraction = 1.41%, humidity 90%,T = 25^0 C, v_{evap}= $0.06 \mu m s^{-1}$. Images taken from Ref.[25].

Wang and Wu [83] Presented molecular dynamics simulation in order to investigate the stick-slip motion during drying droplet using nano-Pillard surface (Figure 1.21). Their simulation is based on investigating the pinning force at the triple line and how it influences the drying mechanism of nano-fluid droplets. They suggested that two forces act at the triple line during drying: the first one is the liquid/liquid interaction forces which push the triple line towards the center; and the second is the solid-liquid interaction forces which attract the triple line to pin on the surface. They have shown that once the triple line arrests, the contact angle decreases dramatically leads to an increase in the depinning force acts on the triple line.

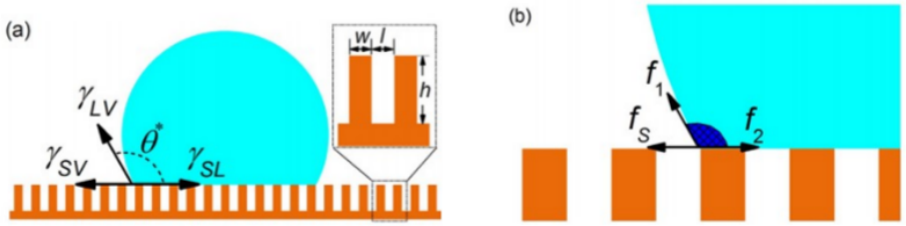

Figure 1.21: (Left) Schematic representation of a sessile droplet on the pillared substrate. (Right) Microscopic perspective of the forces exerted on the triple line where the blue region illustrates the liquid zone in the proximity of the triple line. Images adapted from Ref. [83].

1.2.5.3 Drag coating (Doctor blade)

A periodic structure surface of colloids suspension can be achieved by periodic movement of the triple line via drag coating. Sakamoto et al [35] used this technique in order to fabricate structured lines on the surface via moving substrate periodically at a constant speed (Figure 1.22). The process mechanism depends on the balance between the concentration of particles and the moving distance of the substrate. The stripes width was found to increase with increasing the concentration of particles. The wettability was found to play an important role, for example, when the contact angle increases, the major pinning forces in the meniscus are reduced leading to no deposit on the substrate. However, this group noted that the optimal deposition of particles occurs only with low contact angle. By using ethanol as solvent, they have shown that the defects in the final deposit were reduced due to the low surface tension and low contact angle.

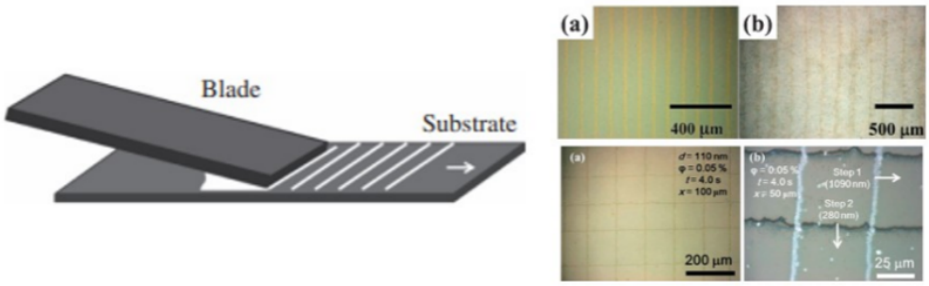

Figure 1.22: (Left) Diagram of the blade-coating process. (Right) Optical microscopic images of stripe structure and network pattern obtained by blade-coating. Images adapted from Ref. [35].

1.2.5.4 Lithographic mask

Lithographic method consists of drying a suspension through a mask containing a patterns of holes to produce structured surface patterns. This method has been used to create surfaces with well-defined structure via controlling a wide range of parameters including solvent evaporation flux, concentration, surface tension, capillary force, temperature, humidity, etc [117]. Regular pattern arrays were obtained by drying a suspension through a mask containing an hexagonal array of micro-sized holes (Figure 1.23) [55].

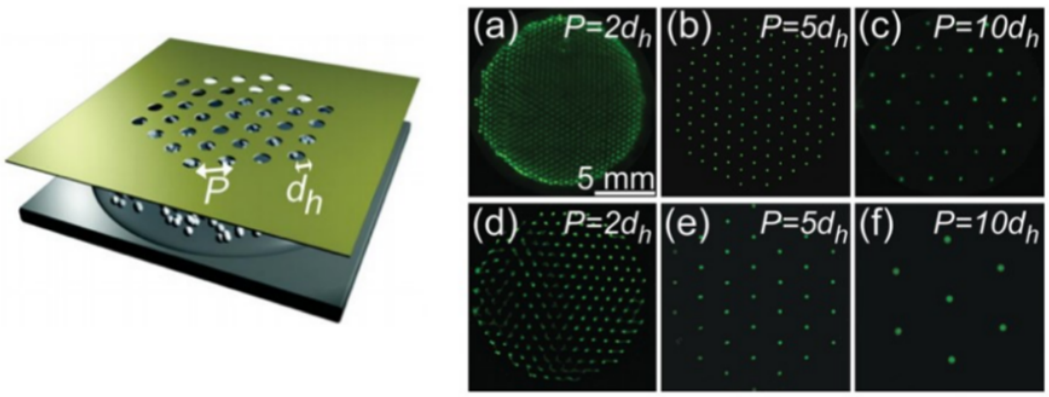

Figure 1.23: (Left) Schematic illustration showing the apparatus of the mask design, including the pitch P and hole diameter d_h.(Right) The obtained patterned formation of the dried films under masks with (a)–(c) $d_h = 250\ \mu m$ and (d)–(f) $d_h = 500\ \mu m$ and varying P. Images modified from Ref. [55].

1.2.6 Particles structures using patterned substrate

The particles deposition into desired structures can also be achieved by using different patterned substrate like silicon, glass. Asbahi et al [118] applied this technique to produce 1D and 2D arrays where the shape of the nanoscale traps on the substrate was designed to be close to the particle diameter (Figure 1.24). In this process, as the evaporation is continuous, the liquid level decreases towards the substrate. Therefore, the particles are driven into the traps imposed by capillary forces that dominates once the height of the meniscus becomes closer to the substrate. The precise position of the particles deposition was obtained by dragging the particles at low velocity from 0.1 to 0.5 mm/min as well as by combining the mechanism of the direct self-assembly and the capillary force at the drying front.

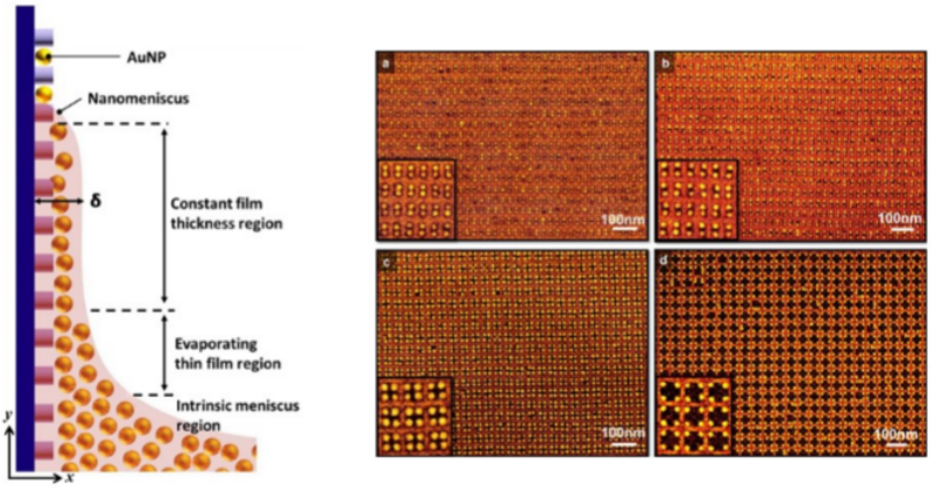

Figure 1.24: (Left) Schematic representation of processing steps of direct the self-assembly of nanoparticles during evaporation. (Right) SEM images exhibiting the obtained arrays of AuNP as self-assembled on HSQ coated Silicon substrates patterned with controllable gaps . Images adapted from Ref. [118].

Yet, the above processes require meticulous technical conditions, which could hinder their potential scale up to become a valuable industrial processes. Therefore, there is still a need for a fast, simple easy to implement method to produce ordered surface morphologies with mildly controlled conditions. This work proposes a fast and simple method for producing ordered surface structures via evaporation of polymer colloidal suspensions by time modulating the drying rate.

Bibliography

[1] Cathleen M Crudden, J Hugh Horton, Mina R Narouz, Zhijun Li, Christene A Smith, Kim Munro, Christopher J Baddeley, Christian R Larrea, Benedict Drevniok, Bheeshmon Thanabalasingam, et al. Simple direct formation of self-assembled n-heterocyclic carbene monolayers on gold and their application in biosensing. *Nature communications*, 7(1):1–7, 2016.

[2] Kapil Debnath, Thalia Dominguez Bucio, Abdelrahman Al-Attili, Ali Z Khokhar, Shinichi Saito, and Frederic Y Gardes. Photonic crystal waveguides on silicon rich nitride platform. *Optics express*, 25(4):3214–3221, 2017.

[3] LK Teh, NK Tan, CC Wong, and S Li. Growth imperfections in three-dimensional colloidal self-assembly. *Applied Physics A*, 81(7):1399–1404, 2005.

[4] Wen-Tao Cao, Wei Feng, Ying-Ying Jiang, Chang Ma, Zi-Fei Zhou, Ming-Guo Ma, Yu Chen, and Feng Chen. Two-dimensional mxene-reinforced robust surface superhydrophobicity with self-cleaning and photothermal-actuating binary effects. *Materials Horizons*, 6(5):1057–1065, 2019.

[5] Emine Tekin, Berend-Jan de Gans, and Ulrich S Schubert. Ink-jet printing of polymers–from single dots to thin film libraries. *Journal of Materials Chemistry*, 14(17):2627–2632, 2004.

[6] Hyoungsoo Kim, François Boulogne, Eujin Um, Ian Jacobi, Ernie Button, and Howard A Stone. Controlled uniform coating from the interplay of marangoni flows and surface-adsorbed macromolecules. *Physical review letters*, 116(12):124501, 2016.

[7] Wageesha Senaratne, Luisa Andruzzi, and Christopher K Ober. Self-assembled monolayers and polymer brushes in biotechnology: current applications and future perspectives. *Biomacromolecules*, 6(5):2427–2448, 2005.

[8] Hung H Pham, Ilya Gourevich, JUNG KWON Oh, James EN Jonkman, and Eugenia Kumacheva. A multidye nanostructured material for optical data storage and security data encryption. *Advanced Materials*, 16(6):516–520, 2004.

[9] Robert A Taylor, Patrick E Phelan, Todd P Otanicar, Chad A Walker, Monica Nguyen, Steven Trimble, and Ravi Prasher. Applicability of nanofluids in high flux solar collectors. *Journal of Renewable and Sustainable Energy*, 3(2):023104, 2011.

[10] Yongjoon Choi, Jeongin Han, and Chongyoup Kim. Pattern formation in drying of particle-laden sessile drops of polymer solutions on solid substrates. *Korean Journal of Chemical Engineering*, 28(11):2130–2136, 2011.

[11] Cédric Boissière, David Grosso, and Eric Prouzet. Inorganic nanomaterials synthesis using liquid crystals. *Encyclopedia of Inorganic Chemistry*, 2006.

[12] Huaixia Zhao, Jiajia Xu, Guangyin Jing, Lizbeth Ofelia Prieto-López, Xu Deng, and Jiaxi Cui. Controlling the localization of liquid droplets in polymer matrices by evaporative lithography. *Angewandte Chemie International Edition*, 55(36):10681–10685, 2016.

[13] Bo Weng, Roderick L Shepherd, Karl Crowley, AJ Killard, and Gordon G Wallace. Printing conducting polymers. *Analyst*, 135(11):2779–2789, 2010.

[14] Lanhe Zhang, Yen Nguyen, and Wei Chen. "coffee ring" formation dynamics on molecularly smooth substrates with varying receding contact angles. *Colloids and Surfaces A: Physicochemical and Engineering Aspects*, 449:42–50, 2014.

[15] Tadashi Kajiya, Wataru Kobayashi, Tohru Okuzono, and Masao Doi. Controlling the drying and film formation processes of polymer solution droplets with addition of small amount of surfactants. *The Journal of Physical Chemistry B*, 113(47):15460–15466, 2009.

[16] Lauryanne Teulon, Yannick Hallez, Simon Raffy, Francois Guerin, Etienne Palleau, and Laurence Ressier. Electrostatic directed assembly of colloidal microparticles assisted by convective flow. *The Journal of Physical Chemistry C*, 123(1):783–790, 2018.

[17] Yuanyi Zhang, Colton A D'Ambra, Reika Katsumata, Ryan L Burns, Mark H Somervell, Rachel A Segalman, Craig J Hawker, and Christopher M Bates. Rapid and selective deposition of patterned thin films on heterogeneous substrates via spin coating. *ACS applied materials & interfaces*, 11(23):21177–21183, 2019.

[18] Xue Li and James F Gilchrist. Large-area nanoparticle films by continuous automated langmuir–blodgett assembly and deposition. *Langmuir*, 32(5):1220–1226, 2016.

[19] Mayuresh Kulkarni, Subhadarshinee Sahoo, Pankaj Doshi, and Ashish V Orpe. Fingering instability of a suspension film spreading on a spinning disk. *Physics of Fluids*, 28(6):063303, 2016.

[20] Chih-Ting Liu, Chia-Chan Tsai, Chien-Wei Chu, Mu-Huan Chi, Pei-Yun Chung, and Jiun-Tai Chen. Dewetting of polymer thin films on modified curved surfaces: preparation of polymer nanoparticles with asymmetric shapes by anodic aluminum oxide templates. *Soft matter*, 14(15):2772–2776, 2018.

[21] Laurent Malaquin, Tobias Kraus, Heinz Schmid, Emmanuel Delamarche, and Heiko Wolf. Controlled particle placement through convective and capillary assembly. *Langmuir*, 23(23):11513–11521, 2007.

[22] Moniraj Ghosh, Fengqiu Fan, and Kathleen J Stebe. Spontaneous pattern formation by dip coating of colloidal suspensions on homogeneous surfaces. *Langmuir*, 23(4):2180–2183, 2007.

[23] Adrien Gans, Emilie Dressaire, Bénédicte Colnet, Guillaume Saingier, Martin Z Bazant, and Alban Sauret. Dip-coating of suspensions. *Soft matter*, 15(2):252–261, 2019.

[24] Satoshi Watanabe, Koji Inukai, Shunsuke Mizuta, and Minoru T Miyahara. Mechanism for stripe pattern formation on hydrophilic surfaces by using convective self-assembly. *Langmuir*, 25(13):7287–7295, 2009.

[25] Hugues Bodiguel, Frédéric Doumenc, and Béatrice Guerrier. Stick- slip patterning at low capillary numbers for an evaporating colloidal suspension. *Langmuir*, 26(13):10758–10763, 2010.

[26] Jun Xu, Jianfeng Xia, Suck Won Hong, Zhiqun Lin, Feng Qiu, and Yuliang Yang. Self-assembly of gradient concentric rings via solvent evaporation from a capillary bridge. *Physical review letters*, 96(6):066104, 2006.

[27] Junhu Zhang, Yunfeng Li, Xuemin Zhang, and Bai Yang. Colloidal self-assembly meets nanofabrication: From two-dimensional colloidal crystals to nanostructure arrays. *Advanced materials*, 22(38):4249–4269, 2010.

[28] Myunghwan Byun and Zhiqun Lin. Self-assembly of highly ordered structures enabled by controlled evaporation of confined microfluids. In *Evaporative Self-Assembly of Ordered Complex Structures*, pages 295–349. World Scientific, 2012.

[29] Valeria Lotito and Tomaso Zambelli. Approaches to self-assembly of colloidal monolayers: A guide for nanotechnologists. *Advances in colloid and interface science*, 246:217–274, 2017.

[30] Karam Nashwan Al-Milaji, Ray Richard Secondo, Tse Nga Ng, Nathaniel Kinsey, and Hong Zhao. Interfacial self-assembly of colloidal nanoparticles in dual-droplet inkjet printing. *Advanced Materials Interfaces*, 5(10):1701561, 2018.

[31] Dayang Wang and Helmuth Möhwald. Template-directed colloidal self-assembly–the route to 'top-down'nanochemical engineering. *Journal of Materials Chemistry*, 14(4):459–468, 2004.

[32] Qingfeng Yan, Ao Chen, Soo Jin Chua, and XS Zhao. Nanosphere lithography from template-directed colloidal sphere assemblies. *Journal of nanoscience and nanotechnology*, 6(6):1815–1818, 2006.

[33] JE Elek, XA Zhang, B Dai, Z Xu, and C-H Chang. Fabrication of three-dimensional hierarchical nanostructures using template-directed colloidal assembly. *Nanoscale*, 7(10):4406–4410, 2015.

[34] Hongta Yang and Peng Jiang. Large-scale colloidal self-assembly by doctor blade coating. *Langmuir*, 26(16):13173–13182, 2010.

[35] Ryuichi Sakamoto, Yoshiki Hataguchi, Ryosuke Kimura, Katsumi Tsuchiya, and Yasushige Mori. Stripe and network formation of particle arrays fabricated by convective self-assembly. *Chemistry Letters*, 41(10):1207–1209, 2012.

[36] Rajneesh Bhardwaj, Xiaohua Fang, Ponisseril Somasundaran, and Daniel Attinger. Self-assembly of colloidal particles from evaporating droplets: role of dlvo interactions and proposition of a phase diagram. *Langmuir*, 26(11):7833–7842, 2010.

[37] Arnaud Lesaine, Daniel Bonamy, Cindy Rountree, Georges Gauthier, Marianne Impéror-Clerc, and Veronique Lazarus. Role of particle aggregation on the structure of dried colloidal silica layers. *Soft Matter*, 2020.

[38] Simon Biggs, Michael Habgood, Graeme J Jameson, et al. Aggregate structures formed via a bridging flocculation mechanism. *Chemical Engineering Journal*, 80(1-3):13–22, 2000.

[39] Robert D Deegan, Olgica Bakajin, Todd F Dupont, Greb Huber, Sidney R Nagel, and Thomas A Witten. Capillary flow as the cause of ring stains from dried liquid drops. *Nature*, 389(6653):827–829, 1997.

[40] Xuefeng Xu and Jianbin Luo. Marangoni flow in an evaporating water droplet. *Applied Physics Letters*, 91(12):124102, 2007.

[41] Robert D Deegan. Pattern formation in drying drops. *Physical review E*, 61(1):475, 2000.

[42] Hua Hu and Ronald G Larson. Marangoni effect reverses coffee-ring depositions. *The Journal of Physical Chemistry B*, 110(14):7090–7094, 2006.

[43] F Doumenc and B Guerrier. Self-patterning induced by a solutal marangoni effect in a receding drying meniscus. *EPL (Europhysics Letters)*, 103(1):14001, 2013.

[44] Sujata Tarafdar, Yuri Yu Tarasevich, Moutushi Dutta Choudhury, Tapati Dutta, and Duyang Zang. Droplet drying patterns on solid substrates: From hydrophilic to superhydrophobic contact to levitating drops. *Advances in Condensed Matter Physics*, 2018, 2018.

[45] Byung Mook Weon and Jung Ho Je. Self-pinning by colloids confined at a contact line. *Physical review letters*, 110(2):028303, 2013.

[46] Martin ER Shanahan. Simple theory of" stick-slip" wetting hysteresis. *Langmuir*, 11(3):1041–1043, 1995.

[47] YingQi Li, HengAn Wu, and FengChao Wang. Effect of a single nanoparticle on the contact line motion. *Langmuir*, 32(48):12676–12685, 2016.

[48] N Bassou and Yahya Rharbi. Role of benard- marangoni instabilities during solvent evaporation in polymer surface corrugations. *Langmuir*, 25(1):624–632, 2009.

[49] M Ulmeanu, M Zamfirescu, and R Medianu. Self-assembly of colloidal particles on different surfaces. *Colloids and Surfaces A: Physicochemical and Engineering Aspects*, 338(1-3):87–92, 2009.

[50] Benjamin Sobac and David Brutin. Triple-line behavior and wettability controlled by nanocoated substrates: influence on sessile drop evaporation. *Langmuir*, 27(24):14999–15007, 2011.

[51] G Guéna, C Poulard, and AM Cazabat. The leading edge of evaporating droplets. *Journal of colloid and interface science*, 312(1):164–171, 2007.

[52] Yasushi Mino, Satoshi Watanabe, and Minoru T Miyahara. Colloidal stripe pattern with controlled periodicity by convective self-assembly with liquid-level manipulation. *ACS applied materials & interfaces*, 4(6):3184–3190, 2012.

[53] Hongta Yang and Peng Jiang. Self-cleaning diffractive macroporous films by doctor blade coating. *Langmuir*, 26(15):12598–12604, 2010.

[54] Maël Le Berre, Yong Chen, and Damien Baigl. From convective assembly to landau- levich deposition of multilayered phospholipid films of controlled thickness. *Langmuir*, 25(5):2554–2557, 2009.

[55] Daniel J Harris, Hua Hu, Jacinta C Conrad, and Jennifer A Lewis. Patterning colloidal films via evaporative lithography. *Physical review letters*, 98(14):148301, 2007.

[56] Y Gorand, F Doumenc, B Guerrier, and C Allain. Instabilités de plissement lors du séchage de films polymeres plans. *Rhéologie*, 3:22–29, 2003.

[57] Joseph L Keddie. Film formation of latex. *Materials Science and Engineering: R: Reports*, 21(3):101–170, 1997.

[58] Y Holl. In les latex synthétiques: Elaboration. *Propriétés, Applications*, 2006.

[59] Jennifer A Lewis. Colloidal processing of ceramics. *Journal of the American Ceramic Society*, 83(10):2341–2359, 2000.

[60] PA Steward, J Hearn, and MC Wilkinson. An overview of polymer latex film formation and properties. *Advances in colloid and interface science*, 86(3):195–267, 2000.

[61] Henri Bénard. Les tourbillons cellulaires dans une nappe liquide. *Rev. Gen. Sci. Pures Appl.*, 11:1261–1271, 1900.

[62] X Fanton and AM Cazabat. Spreading and instabilities induced by a solutal marangoni effect. *Langmuir*, 14(9):2554–2561, 1998.

[63] C Allain and L Limat. Regular patterns of cracks formed by directional drying of a collodial suspension. *Physical review letters*, 74(15):2981, 1995.

[64] Wai Peng Lee and Alexander F Routh. Why do drying films crack? *Langmuir*, 20(23):9885–9888, 2004.

[65] Ludovic Pauchard, Berengere Abou, and Ken Sekimoto. Influence of mechanical properties of nanoparticles on macrocrack formation. *Langmuir*, 25(12):6672–6677, 2009.

[66] Mourad Chekchaki. *Détermination théorique et expérimentale des contraintes mécaniques induisant les fractures lors du séchage de suspensions colloïdales*. PhD thesis, 2011.

[67] Abdulgadir Ahmed Abusaksaka. *Structuration et défauts de surface et de volume lors du séchage de suspensions colloïdales*. PhD thesis, 2013.

[68] L Pauchard and C Allain. Buckling instability induced by polymer solution drying. *EPL (Europhysics Letters)*, 62(6):897, 2003.

[69] Guillaume Toussaint, Hugues Bodiguel, Frédéric Doumenc, Béatrice Guerrier, and Catherine Allain. Experimental characterization of buoyancy-and surface tension-driven convection during the drying of a polymer solution. *International Journal of Heat and Mass Transfer*, 51(17-18):4228–4237, 2008.

[70] D Brutin and V Starov. Recent advances in droplet wetting and evaporation. *Chemical Society Reviews*, 47(2):558–585, 2018.

[71] Odile Carrier, Noushine Shahidzadeh-Bonn, Rojman Zargar, Mounir Aytouna, Mehdi Habibi, Jens Eggers, and Daniel Bonn. Evaporation of water: evaporation rate and collective effects. *Journal of Fluid Mechanics*, 798:774–786, 2016.

[72] RG Picknett and R Bexon. The evaporation of sessile or pendant drops in still air. *Journal of Colloid and Interface Science*, 61(2):336–350, 1977.

[73] Robert D Deegan, Olgica Bakajin, Todd F Dupont, Greg Huber, Sidney R Nagel, and Thomas A Witten. Contact line deposits in an evaporating drop. *Physical review E*, 62(1):756, 2000.

[74] C Poulard, O Benichou, and AM Cazabat. Freely receding evaporating droplets. *Langmuir*, 19(21):8828–8834, 2003.

[75] G Guéna, C Poulard, and A-M Cazabat. The dynamics of evaporating sessile droplets. *Colloid Journal*, 69(1):1–8, 2007.

[76] N Murisic and L Kondic. Modeling evaporation of sessile drops with moving contact lines. *Physical Review E*, 78(6):065301, 2008.

[77] N Murisic and L Kondic. On evaporation of sessile drops with moving contact lines. *Journal of fluid mechanics*, 679:219, 2011.

[78] Edward Bormashenko, Albina Musin, and Michael Zinigrad. Evaporation of droplets on strongly and weakly pinning surfaces and dynamics of the triple line. *Colloids and Surfaces A: Physicochemical and Engineering Aspects*, 385(1-3):235–240, 2011.

[79] Mebrouk Ait Saada, Salah Chikh, and Lounes Tadrist. Evaporation of a sessile drop with pinned or receding contact line on a substrate with different thermophysical properties. *International journal of heat and mass transfer*, 58(1-2):197–208, 2013.

[80] Jiaxing Huang, Franklin Kim, Andrea R Tao, Stephen Connor, and Peidong Yang. Spontaneous formation of nanoparticle stripe patterns through dewetting. *Nature materials*, 4(12):896–900, 2005.

[81] KS Birdi and DT Vu. Wettability and the evaporation rates of fluids from solid surfaces. *Journal of adhesion science and technology*, 7(6):485–493, 1993.

[82] Daniel Orejon, Khellil Sefiane, and Martin ER Shanahan. Stick–slip of evaporating droplets: substrate hydrophobicity and nanoparticle concentration. *Langmuir*, 27(21):12834–12843, 2011.

[83] FengChao Wang and HengAn Wu. Molecular origin of contact line stick-slip motion during droplet evaporation. *Scientific reports*, 5:17521, 2015.

[84] Pavlo Takhistov and Hsueh-Chia Chang. Complex stain morphologies. *Industrial & engineering chemistry research*, 41(25):6256–6269, 2002.

[85] Laura Grandas, Christelle Reynard, Robert Santini, and Lounès Tadrist. Etude expérimentale de l'évaporation d'une goutte posée sur une plaque chauffante. influence de la mouillabilité. *International journal of thermal sciences*, 44(2):137–146, 2005.

[86] Dong Hwan Shin, Seong Hyuk Lee, Jung-Yeul Jung, and Jung Yul Yoo. Evaporating characteristics of sessile droplet on hydrophobic and hydrophilic surfaces. *Microelectronic Engineering*, 86(4-6):1350–1353, 2009.

[87] Yueh-Feng Li, Yu-Jane Sheng, and Heng-Kwong Tsao. Evaporation stains: suppressing the coffee-ring effect by contact angle hysteresis. *Langmuir*, 29(25):7802–7811, 2013.

[88] Xiaohua Fang, Bingquan Li, Eric Petersen, Yuan Ji, Jonathan C Sokolov, and Miriam H Rafailovich. Factors controlling the drop evaporation constant. *The Journal of Physical Chemistry B*, 109(43):20554–20557, 2005.

[89] Xiaohua Fang, Bingquan Li, Jonathan C Sokolov, Miriam H Rafailovich, and Dina Gewaily. Hildebrand solubility parameters measurement via sessile drops evaporation. *Applied Physics Letters*, 87(9):094103, 2005.

[90] Lei Jiang, Yong Zhao, and Jin Zhai. A lotus-leaf-like superhydrophobic surface: a porous microsphere/nanofiber composite film prepared by electrohydrodynamics. *Angewandte Chemie*, 116(33):4438–4441, 2004.

[91] Jung-Hoon Kim, Sang-Byung Park, Jae Hyun Kim, and Wang-Cheol Zin. Polymer transports inside evaporating water droplets at various substrate temperatures. *The Journal of Physical Chemistry C*, 115(31):15375–15383, 2011.

[92] Hua Hu and Ronald G Larson. Analysis of the microfluid flow in an evaporating sessile droplet. *Langmuir*, 21(9):3963–3971, 2005.

[93] Jacob N Israelachvili. *Intermolecular and surface forces*. Academic press, 2011.

[94] J Lyklema, HP Van Leeuwen, and M Minor. Dlvo-theory, a dynamic re-interpretation. *Advances in colloid and interface science*, 83(1-3):33–69, 1999.

[95] Shinrtosuke Usui. Dlvo theory of colloid stability. In *Electrical Phenomena at Interfaces*, pages 101–118. Routledge, 2018.

[96] Jung-Yeul Jung, Young Won Kim, and Jung Yul Yoo. Behavior of particles in an evaporating didisperse colloid droplet on a hydrophilic surface. *Analytical chemistry*, 81(19):8256–8259, 2009.

[97] Tak-Sing Wong, Ting-Hsuan Chen, Xiaoying Shen, and Chih-Ming Ho. Nanochromatography driven by the coffee ring effect. *Analytical chemistry*, 83(6):1871–1873, 2011.

[98] HH Lee, SC Fu, CY Tso, and Christopher YH Chao. Study of residue patterns of aqueous nanofluid droplets with different particle sizes and concentrations on different substrates. *International Journal of Heat and Mass Transfer*, 105:230–236, 2017.

[99] Alexander F Routh and William B Russel. Horizontal drying fronts during solvent evaporation from latex films. *AIChE Journal*, 44(9):2088–2098, 1998.

[100] Lucas Goehring, William J Clegg, and Alexander F Routh. Solidification and ordering during directional drying of a colloidal dispersion. *Langmuir*, 26(12):9269–9275, 2010.

[101] C Nadir Kaplan and L Mahadevan. Evaporation-driven ring and film deposition from colloidal droplets. *Journal of Fluid Mechanics*, 781, 2015.

[102] Costas M Soukoulis. *Photonic band gap materials*, volume 315. Springer Science & Business Media, 2012.

[103] JA Strauss, PA Soave, RS Ribeiro, and F Horowitz. Absorber and self-cleaning surfaces on modified polymer plates for solar harvesting in the humid (sub) tropics. *Solar Energy*, 122:579–586, 2015.

[104] Seung Goo Lee, Dong Yun Lee, Ho Sun Lim, Dae Ho Lee, Shichoon Lee, and Kilwon Cho. Switchable transparency and wetting of elastomeric smart windows. *Advanced materials*, 22(44):5013–5017, 2010.

[105] Qianqian Shang and Yonghong Zhou. Fabrication of transparent superhydrophobic porous silica coating for self-cleaning and anti-fogging. *Ceramics International*, 42(7):8706–8712, 2016.

[106] Nikolai D Denkov, OD Velev, PA Kralchevsky, IB Ivanov, Hideyuki Yoshimura, and Kuniaki Nagayama. Two-dimensional crystallization. *Nature*, 361(6407):26–26, 1993.

[107] David B Hall, Patrick Underhill, and John M Torkelson. Spin coating of thin and ultrathin polymer films. *Polymer Engineering & Science*, 38(12):2039–2045, 1998.

[108] Deying Xia, Abani Biswas, Dong Li, and Steven RJ Brueck. Directed self-assembly of silica nanoparticles into nanometer-scale patterned surfaces using spin-coating. *Advanced Materials*, 16(16):1427–1432, 2004.

[109] Jian Chen, Peitao Dong, Di Di, Chaoguang Wang, Haoxu Wang, Junfeng Wang, and Xuezhong Wu. Controllable fabrication of 2d colloidal-crystal films with polystyrene nanospheres of various diameters by spin-coating. *Applied Surface Science*, 270:6–15, 2013.

[110] Johannes Schmitt, Gero Decher, Walter J Dressick, Susan L Brandow, Robert E Geer, R Shashidhar, and Jeffrey M Calvert. Metal nanoparticle/polymer superlattice films: fabrication and control of layer structure. *Advanced Materials*, 9(1):61–65, 1997.

[111] Kevin M Chen, Xueping Jiang, Lionel C Kimerling, and Paula T Hammond. Selective self-organization of colloids on patterned polyelectrolyte templates. *Langmuir*, 16(20):7825–7834, 2000.

[112] David A Walker, Bartlomiej Kowalczyk, Monica Olvera de La Cruz, and Bartosz A Grzybowski. Electrostatics at the nanoscale. *Nanoscale*, 3(4):1316–1344, 2011.

[113] Giang TH Tran, Masaki Koike, Tetsuo Uchikoshi, and Hiroshi Fudouzi. Fabrication of polystyrene colloidal crystal film by electrophoretic deposition. *Advanced Powder Technology*, 31(8):3085–3092, 2020.

[114] Jaemyung Kim, Franklin Kim, Kwonnam Sohn, Laura J Cote, and Jiaxing Huang. Patterning and assembling nanomaterials by dip coating. In *Evaporative Self-Assembly Of Ordered Complex Structures*, pages 189–233. World Scientific, 2012.

[115] Guillaume Berteloot, Adrian Daerr, François Lequeux, and Laurent Limat. Dip coating with colloids and evaporation. *Chemical Engineering and Processing: Process Intensification*, 68:69–73, 2013.

[116] Sergio Palma and Henri Lhuissier. Dip-coating with a particulate suspension. *Journal of Fluid Mechanics*, 869, 2019.

[117] Robert A Hughes, Eredzhep Menumerov, and Svetlana Neretina. When lithography meets self-assembly: a review of recent advances in the directed assembly of complex metal nanostructures on planar and textured surfaces. *Nanotechnology*, 28(28):282002, 2017.

[118] Mohamed Asbahi, FuKe Wang, Zhaogang Dong, Joel KW Yang, and Karen SL Chong. Directed self-assembly of sub-10 nm particle clusters using topographical templates. *Nanotechnology*, 27(42):424001, 2016.

Chapter 2

MATERIALS AND METHODS

Contents

The polymerization of the particles used and experimental setups are addressed in this chapter, including the quantitative and qualitative characterization of the obtained polymer particles, as well as the drying method chosen for this study.

2.1 Synthesis of polymer particles by polymerization emulsion

Latexes are colloidal dispersions of polymer particles in water, which is widely used in various industrial sectors such as coating, adhesives, paper, biomedical and varnishes field, etc. These particles are stabilized by a surfactant adsorbed to their surface. Emulsion polymerization (Figure 2.1) [1] is a radical polymerization process consisting of polymerizing monomers dispersed in an emulsion. The process is conducted in a closed batch reactor where the reactants are added to the reactor at the beginning of the reaction, which includes water, the surfactant, the monomers, and the initiator. In such a process, the dissolved oxygen triggers the formation of free radicals ROM_XOO^- in the aqueous phase. Hence, removing this inhibitor before reaching the reaction temperature is crucial to prevent side reaction. It is, therefore, necessary to purge the reactor and work under an inert atmosphere of nitrogen or argon. Stirring must be carried out in order to obtain a homogeneous temperature of the reaction.

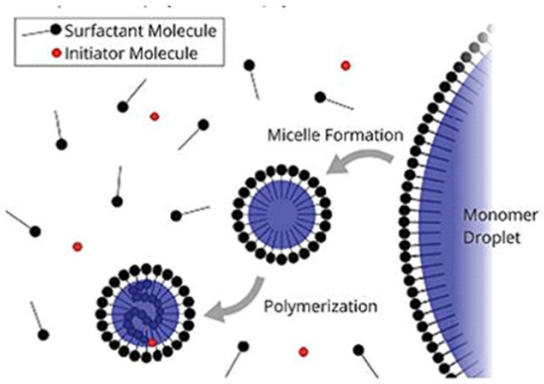

Figure 2.1: Schematic diagram of emulsion polymerization. Image taken from Ref [1]

2.2 Materials and experimental synthesis apparatus

2.2.1 Materials used

In this study, the polystyrene particles and the polybutylacrylate particles are obtained from styrene and Butyl acrylate monomers by emulsion polymerization. The components used to undergo the radical polymerization are described herein.

2.2.1.1 Monomer

The main monomers used in emulsion polymerization are: styrene (St, 99%, Aldrich) and butyl acrylate (BA, 99 % Aldrich). The monomers have different chemical and physical properties and different structures. The characteristics of these monomers are shown in Table 1.

Name	Styrene	Butyl acrylate
Chemical formula	C_8H_8	$C_7\ H_{12}\ O_2$
Abbreviation	sty	pba
Molar mass (g/mol)	104.15	128.2
Boiling point (^0C)	145.2	145
Density at 20 (^0C) (kg/m^3)	906	890
Glass transition temperature of the polymer (^0C)	100	-49

Table 1. Characteristics of styrene and Butyl acrylate monomer used.

2.2.1.2 Dispersion medium

Water is used as a dispersion medium in emulsion polymerizations. Water is used due to its low viscosity and can provide a perfect heat transfer.

2.2.1.3 Emulsifier

The most commonly used emulsifier in this process is sodium dodecyl sulfate (SDS, Aldrich, 99%), it is an anionic surfactant. SDS is preferred in many emulsion polymerization systems for controlling the particle size and to stabilize the latex particles in the dispersion. The characteristics of surfactant are illustrated in Table 2

Name	Sodium Dodecyl Sulfate
Chemical formula	$C_{12}H_{25}\ N_a\ O_4$ S
Abbreviation	SDS
Molar mass (g/mol)	288.38
Formation at ambient temperature	Solid

Table 2. Physico-chemical characteristics of surfactant.

2.2.1.4 Initiator

The initiator used in this process is potassium persulfate (KPS, Aldrich, 98%). The characteristics of KPS are shown in Table 3.

Name	Potassium persulfate
Chemical formula	$K_2S_2O_8$
Abbreviation	KPS
Molar mass (g/mol)	270.32
Formation at ambient temperature	Solid
Decomposition temperature (^0C)	starts from 60

Table 3. Physico-chemical characteristics of the initiator.

2.2.2 Experimental setup

The synthesized latex is prepared in a closed batch reactor. Monomers, surfactant, and water are mixed at the reaction condition in a standard three-neck round flask (500 mL) equipped with a magnetic stirrer, a reflux condenser with nitrogen flow, and an oil bath under controlled temperature (Figure 2.2). The initiator is added when the mixture reached the desired temperature and the agitation is performed continuously with speed

control for the whole period of the reaction.

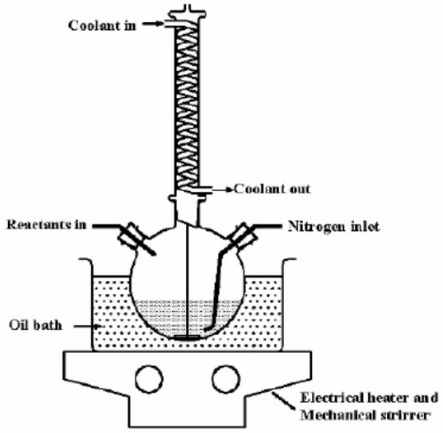

Figure 2.2: Polymer emulsion polymerization set up.

2.3 Experimental procedure for the synthesis of particles

All the particles are synthesized by conventional emulsion polymerization using a batch reactor at 80^0 C. Firstly, the dispersion of surfactants in water is degassed by a continuous flow of nitrogen for 20 $\sim$ 30 min in order to get rid of the oxygen present in the aqueous medium. After that, a sufficiently high shear is ensured by constant stirring. When the monomer and the initiator are fully dissolved in water, they are injected into the reactor. The nitrogen pressure should be kept at a low value to prevent inhibition of the polymerization reactions. Then, 10% of the initial amount of the initiator is injected at the end of the synthesis in order to complete the conversion of the residual monomer. The process of polymerization is carried out at 300 rpm while the period of synthesis is ranged from 4h to 12h. The latex particles of PS and PBA are synthesized at about 10% weight respect to the mass of water. The surfactants introduced in this process have a direct impact on the size of the resulting polymer particles: Figure 2.3 shows the relation between the quantity of surfactant and the size of particles resulting from the polymerization [2]. Indeed, the particles diameter decreases when the amount of SDS increases.

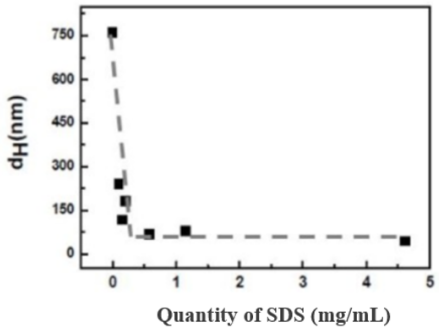

Figure 2.3: Influence of [SDS] on the diameter of the synthesized particles. Curve taken from Ref [2]

2.3.1 The concentration of solid content

The solid fraction is measured by calculating the dry extract. A cup is filled with 5ml of colloidal suspension and then placed in an oven to evaporate. The mass concentration of the solution is evaluated by weighing the cup and its content before and after evaporation.

2.4 Characterization of the synthesized polymers

2.4.1 Particle characterization

2.4.1.1 Particle Size Characterization

The characterization of the particle size (D) was obtained by dynamic light scattering (DLS) (Figure 2.4). The apparatus is a Malvern Zétasizer 5000 consisting of a multi-angle goniometer ($8^o - 150^0$) thermostatically controlled ($15^0\ C - 50^0\ C$), a 5 Mw He-Ne laser operating at 633nm, and a multi-bit correlator 7132 (allowing the analysis of intensity fluctuations whose characteristic time is between:$0.2\mu s$ and $3600\mu s$). The overall scattered intensity is measured using a 400 μm 90^0 pinhole. These light fluctuation times allow to calculate the scattering coefficients of the particles, from which an average value of the hydrodynamic radius can be extracted. The analysis of correlation functions is done by cumulating method which gives an average diameter and a size distribution, as well as by the CONTIN program. This method allows the estimation of particle size distribution in the range from nano- to micrometers.

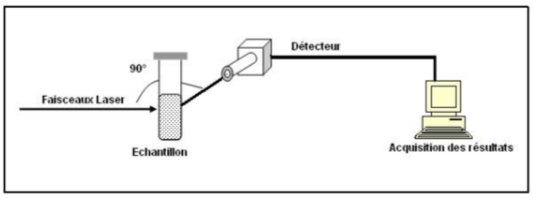

Figure 2.4: Quasi-elastic light scattering spectrometer

2.4.1.2 Glass transition temperature T_g of polymers

Differential Scanning Calorimetry (DSC) is used to study the physical state changes like crystallization or glass transition temperatures in materials such polymers [3, 4]. The DSC set-up consists of a measurement chamber which contains two crucibles where they are heated: a sample crucible and an empty crucible (Figure 2.5, left). The sample crucible containing the material being investigated while the empty crucible is used as a reference. A heat flow is induced by a thermocouple to heat both crucibles. The glass transition temperature T_g is determined on a Mettler Toledo 823, coupled to an intercooler cooling system under an inert nitrogen atmosphere with a flow rate of 80 ml/min. The system is calibrated using Indium and Zinc. Samples of approximately 5 mg in powder form were weighed precisely and placed in drilled aluminum crucibles. The DSC measurement curve is a convenient technique for calculating the T_g for polymer such as polystyrene according to the diagram below (Figure 2.5, right). Table 4 shows a summary of the particle diameters, T_g and dry extracts for the suspensions used.

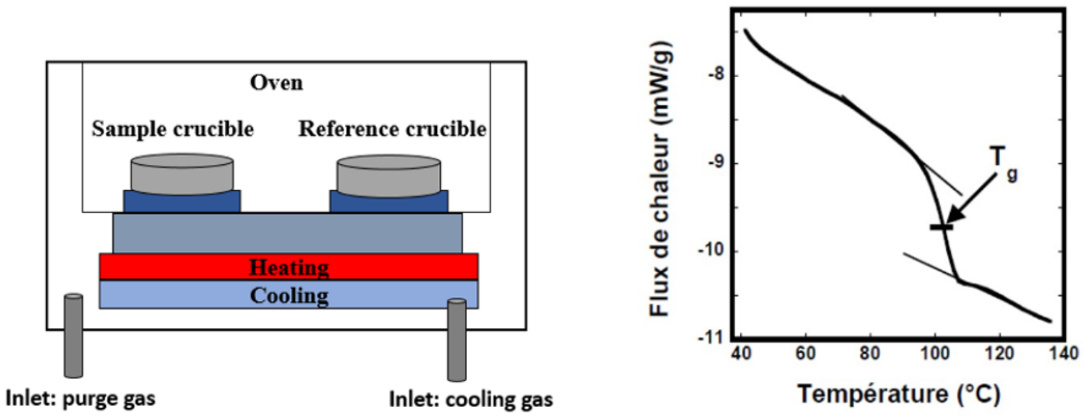

Figure 2.5: (Left) (Diagram of Differential Scanning Calorimetry - DSC). (Right) Diagram of the glass transition of PS polymer

Polymer	Name of sample	Diameter (nm)	$T_g\ ^0C$	% Dry extract
Polystyrene	PS	97.5	100	9.4
Polybutylacrylate	PBA	64	-49	9.01

Table 4. Particle diameters, T_g and dry extracts of the suspensions used.

2.4.1.3 Molar mass distribution

Every polymer type has its own molar mass distribution. It is a fundamental parameter in the characterization of polymer particles. Therefore, achieving the desired polymer properties requires controlling the process conditions including molecular weight distribution and temperature [5]. The molar mass distribution of a polymer can be obtained by gel permeation chromatography (GPC) analytical method. This technique provides an excellent system to determine the molar mass distribution. The system consists of a Waters 590 (GPC) apparatus equipped with a Waters 410 differential refractometer and a Waters 745 data module. THF solvent after being filtered through 0.45 mm Millipore filters is used at a flow rate of 1 ml / min through ulrastyragel columns with a size exclusion of 500, 10^3 and 10^4 A^0. The GPC device was calibrated by using polystyrene standards which have a well-defined molar mass distribution, supplied by the Waters Company. $\sim 3\ mg$ of polymer powder is dissolved in 1 ml of THF. THF was used as a pure solvent, which already filtered through Millipore 0.45 filters. The numbered samples are placed in the machine's injection system, the injection volumes for the measurements are $5\mu l$, and the measurements are made at ambient temperature.

2.4.2 Surface charge characterization of colloidal particles

2.4.2.1 Ion exchange procedure

During the latex emulsion polymerization, adding SDS surfactant and the KPS initiator create $[SO4^-]$ ions on the particles surface leading to the stabilization of the particles in the solution. The presence of these ions on the particles surface prevents the measurement of the charge density of the particles. Therefore, it is necessary to remove these ions from the particles surface by washing in order to make the pH of the latex solution neutral. Hence, the ion exchange resins composed of mixture of cationic and anionic resins ($HCR-S[H^+]\ and\ SBR[OH^-]:1:1$ ($Dowex^\wedge\ Marathon^\wedge$ MR-3, Aldrich) is used for that purpose. The process relies on the capture of sodium and potassium cations $[K^+, Na^+]$ as well as the sulfonates anions $[SO2^-]$ by the resin, eventually producing $[H^+, OH^-]$ ions leading to water formation. This process was done by i) mixing the suspensions with about 5 to 10 wt % resin, ii) agitating for 20-30 minutes, iii) and then filtering to remove the resin by using small syringes with a hole diameter smaller than the resin beads diameter. The procedure of washing is repeated for several times in order to ensure that the surfactant, which was added during the preparation of

the emulsion, is completely removed. After each step of washing, the conductivity was monitored until it reaches a constant value.

2.4.2.2 Conductometric titration

The cleaned latex is almost free of surfactant and likely to be stabilized with sulfate groups. Those are coming from the persulfate decomposition or some SDS remaining on the particles surface. Therefore, a titration with NaOH was carried out in order to quantify the sulfate groups on the particles surface. Before describing the experimental protocol, we briefly recall that conductivity provides an indication of the ion concentration on the particles surface as well as their mobility. The conductometric titration was carried out with a NaOH solution of concentration 2.10^{-4} mol / L. The principle of this method is based on the gradual adding of a NaOH titrating solution, using a graduated burette to the cleaned latex diluted at some percent by weight. The H^+ ions are gradually replaced by Na^+ ions until chemical equilibrium is reached. Figure 2.6 illustrates the experimental setup.

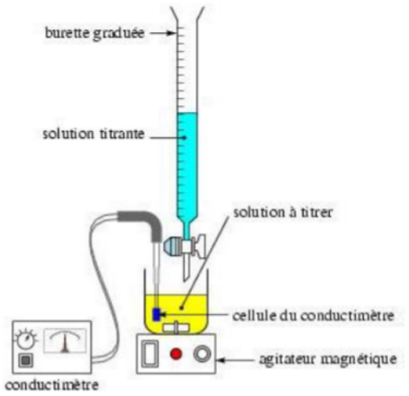

Figure 2.6: Experimental apparatus for conductimetric titration.

Before adding NaOH, the conductivity is high because of the presence of highly mobile hydrogen ions. When NaOH is added the conductivity is decreased (Figure 2.7). This decrease in the conductivity is because of the replacement of the more mobile H^+ ions by the less mobile Na^+ ions. Then the conductivity is increased due to the increase of concentration of free ions of Na^+ and OH^-.

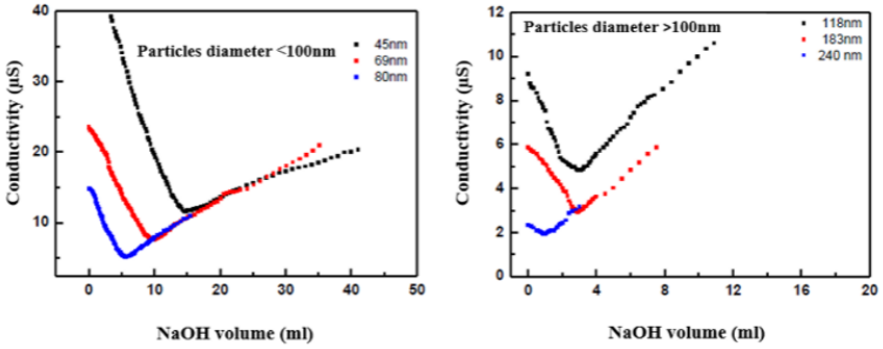

Figure 2.7: Conductumetric titration of different PS particle sizes. Curves modified from Ref.[2]

The minimum point on the curves corresponds to the neutralization of strong acids sulfate [6]. This equivalence point is governed by the equilibrium [7]:
R - O - $SO_3^-H^+ + NaOH \rightarrow R - O - SO_3^-Na^+ + H_2O$

Indeed, the equivalent conductivity σ at 25^0 C for H^+ ions is 350 $cm^2\ \Omega^{-1}\ mol^{-1}$ and for Na^+ is 50.1 $cm^2\ \Omega^{-1}\ mol^{-1}$ while for OH^- is 199.1 $cm^2\ \Omega^{-1}\ mol^{-1}$. For each particle size, the surface charge is calculated from the conductometric titration , using the equation below [8]:

$$Charge(moles/g) = \frac{V_{e,NaOH} C_{NaOH}}{m_0 \phi} \tag{2.1}$$

Where m_0 is the initial mass of the titrated latex (g),
$V_{e,NaOH}$ is the volume of NaOH at the equivalence point (mL).
ϕ is the Mass fraction (%).
C_{NaOH} is the concentration of NaOH = 10^{-1} mol / L

Figure 2.8 shows the surface charge as a function of the surface to volume ratio (3 / R) for all particles. It is clear that the surface charge increases when the particles size decreases. This shows that small particles have a higher surface charge than big particles.

2.4.2.3 Elemental analysis technique

The elemental analysis was used to quantify the overall amount of sulfate group on the washed particles . The process relies on heating the samples above 1000^0C and analyzing the resulting elements. Figure 2.8 highlights the amount of sulfur versus the surface to volume ratio (3 / R) in conductivity titration and in elemental analysis. The

total amount of sulfur follows the same tendency as for conductivity titration. This result suggests that the sulfate groups are located only on the surface of the particles. Conductimetric titration can only determine the amount of sulfate present at the surface of the particles, however, the elemental analysis provides information on the total amount of sulfate groups that are present near and on the surface of the particles. This may explain the small difference between the two curves. This result indicates that the SDS surfactant and the KPS salt ions are indeed removed from the particle surface.

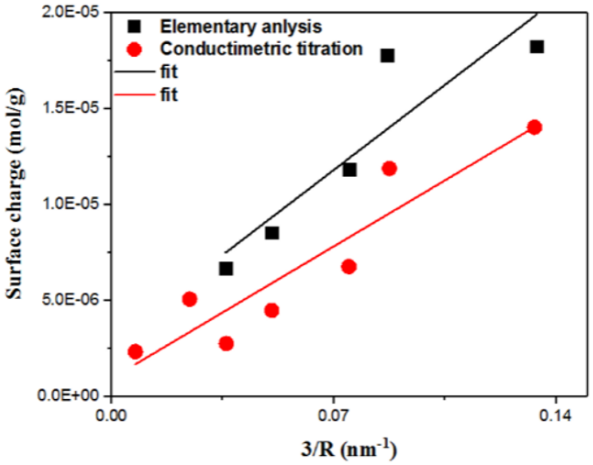

Figure 2.8: Comparison of the results of elemental analysis and titration conductivity of the amount of sulphate groups on the surface of the different particles synthesized. Curves modified from Ref [2].

2.4.3 Characterization of the electric potential of the particles

Zeta potential is a physical property exhibited by the net surface charge carried by the nanoparticles. The zeta potential of colloidal particles is measured by evaluating their movements in a known electric field. The colloids are placed in an electrophoresis chamber consisting of two compartments containing an electrode and a connection chamber. The applied voltage between the two electrodes produces a uniform electric field in the connection chamber and the charged particles move towards one of these electrodes [9].

2.4.3.1 The electric potential of particles in the absence and presence of salt

Figure 2.9 illustrates the results of Zeta potential measurements for PBA and PS particles. The result shows that the absolute value of Zeta potential increases when the particle diameter decreases. The Zeta potential value of polystyrene particles is lower than the PBA.

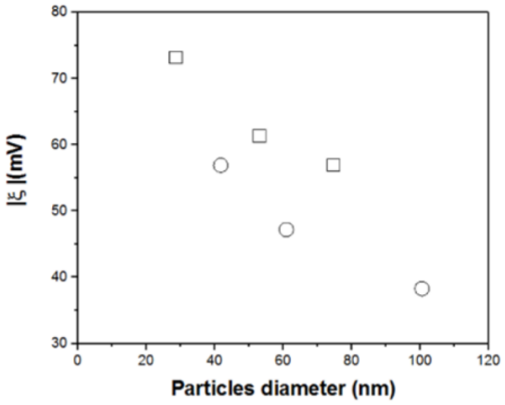

Figure 2.9: Evolution of the Zeta potential as a function of the particles size PBA (□), PS(○). Curves modified from Ref [9]

However, during the formation of the film in presences of salt, the evaporation of the water leads to an increase in the concentration of electrolytes initially contained in the suspension. This enhances the electrostatic interaction between the particles. Therefore, the study of the effect of salt on the particles stabilities is necessary. From figure 2.10, it can be seen that the polystyrene particles exhibit the same tendency of decrease in Zeta potential as PBA particles with respect to the ionic strength. However, PS is much more sensitive to variations in NaCl concentration than PBA. In the case of polystyrene particles, the decrease is rapid even for low salt concentrations. It is obvious that the final value of ξ reached in the presence of NaCl is lower in the case of polystyrene compared to PBA.

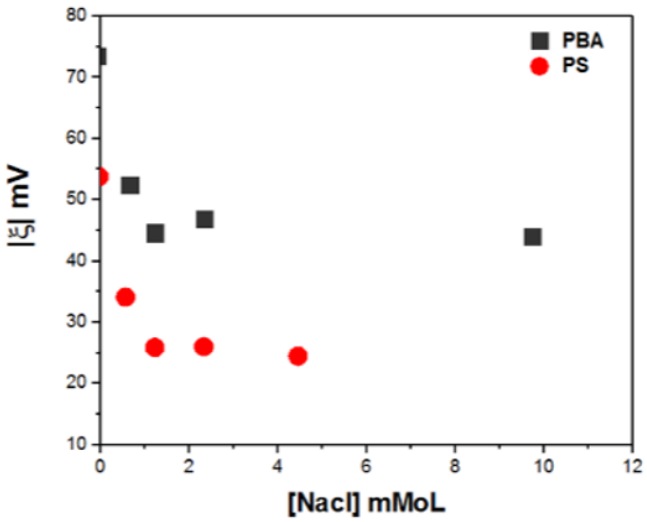

Figure 2.10: Evolution of the Zeta potential of the PS latex and ξ (PBA) vs. [NaCl]. Curves modified from Ref [9]

2.4.4 Surface tension measurement

Surface tension measurement is an important parameter in science, in particular, coatings, adhesive application, since it is directly related to the forces acting on the interface between air and liquid, and to the physical state behavior of liquids. The technique consist in taking the geometrical profile of a drop just before it collapses from a capillary tube. The Digidrop GBX apparatus is used to measure the surface tension of the droplet (Figure 2.11 left). This instrument can measure interfacial tension by the pendant drop method (Figure 2.11 right). The procedure is based on capturing the images of a liquid drop hanging from a dosing needle during its growth until its detachment. The software automatically calculates the surface tension in a spreadsheet. Several measurements were taken in each experiment. However, the calculation is only performed for the last ten images. This process was repeated several times at ambient conditions. Table 5 shows a comparison between the values of surface tension in water and for a suspension, with and without SDS.

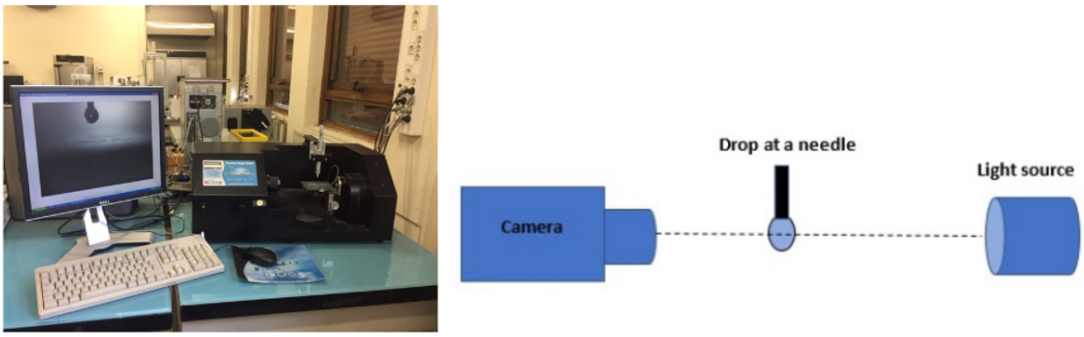

Figure 2.11: (Left) Digidrop GBX apparatus. (Right) Schematic setup for the pendant drop method

Surfactant	Surface tension (mN.m^{-1})	
[SDS] mmol/L	Pure water	(PS / PBA) mixture
0	72	71
3.5	62	68
6.9	47	58
10.4	41	45
13.8	39	35
17.3	37	34
24	34	33

Table 5. Surface tension in water and suspension

2.5 Suspension and substrate surface

The contact angle plays a major effect on the behavior of the triple line and the deposit pattern during drying [10]. This part describes the technique used to measure this parameter

2.5.1 Contact angle measurement

The Digidrop GBX optics apparatus is used to measure the contact angle of the droplet between the liquid surface and the solid substrate. The principle of this method is based on the analysis of a video image coming from a CCD sensor. The apparatus consists of the following parts (Figure 2.12)
. a solid substrate where the sample is placed
. a micro drop regulator to deposit a precise volume of a suspension on the substrate
. a light source

. a mobile CCD camera and a macro lens on the horizontal axis to focus the images
. The image analysis and processing system to determine the contour of the drop
. A software system to measure the contact angle
The taken images undergo a number of digital treatments in order to improve their quality. The software can then analyze the digitized image of the drop and determines its geometric characteristics. The baseline, that means the horizontal axis connecting the two points of the drop edge can be set automatically by the software or manually by the user. This is an important feature in the measurement of contact angles because it allows to determine the value of these angles more precisely. In most cases, the surface state of the sample causes a dissymmetry of the drop shape, therefore, the contact angles on the right and on the left will change. The software offers a measurement method that takes this asymmetry into account and automatically calculates the values of the left angle, the right angle, and their average value. The measurement of the contact angle on the solid substrate for cleaned PS, PBA, and their blends are given in Table 6. As for the contact angle of (PS / PBA) mixture with different concentration of SDS, they are shown in Table 7.

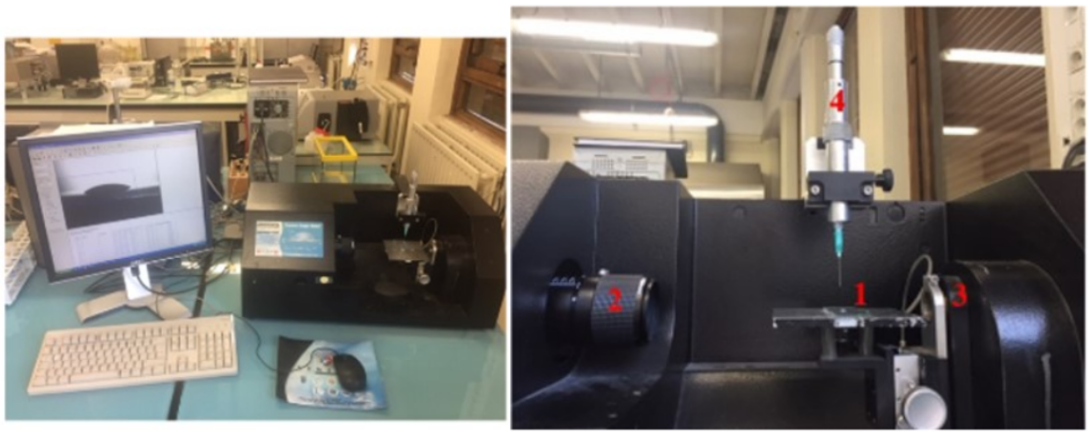

Figure 2.12: ((Left) Digidrop GBX apparatus. (Right) (1) Solid substrate (2) CCD camera (3) Light source (4) Micro drop regulator.

Suspension	Contact angle
PS	11.7
PBA	5.7
Mixture of (PS/PBA)	19.5

Table 6. Contact angle for clean suspensions of PS, PBA, and their mixture.

Surfactant concentration (mmol/L)	Contact angle
0	19.9
3.5	17
6.9	15.8
13.8	11.9
17.3	8.4
24	4.8
31	3.4

Table 7. Contact angle measured for (PS / PBA) mixture with different concentration of SDS.

2.6 Drying method

2.6.1 Samples preparation.

Samples used in this study contain nanoparticles with different sizes such polystyrene PS with hard particles (64 nm 10% w), poly butyl acrylate PBA with soft particles (97,5 nm 10% w), and PS with hard particles (280.1 nm 10% w). These suspensions were washed separately before mixing by using Dowex resins in order to remove the surfactant. Glass microscope slides were used in these experiments with (76 x 26 x 1 mm) dimension. The substrates were cleaned with water and ethanol. The purpose of cleaning is to ensure a certain homogeneity of the substrate, hence, to guarantee a perfect surface condition during evaporation. The same quantity of droplets were deposited on the glass substrate (microscope slide). All the experiments were done at room temperature (23^0C). The temperature is kept constant by air conditioning.

2.6.2 Drying under normal condition

Mass loss during droplet drying was measured using a Mettler balance with a precision of 0.01 mg, connected to a computer with a home-built software (Figure 2.13 left). Droplet of the colloidal suspensions of PS, PBA, and their blends, were deposited on a glass substrate, with the same quantity, and left until the drying is completely finished. The drying kinetics of these suspensions in free air follows the same tendency and exhibits two stages of drying (Figure 2.13 right): (i) a constant drying rate in early times where the dispersed particles do not influence the drying rate velocity, (ii) and a decreasing rate as the concentration of particles in the film becomes higher and this is probably due to skin formation. This process leads to an irregular deposition pattern along the surface, during drying under normal condition.

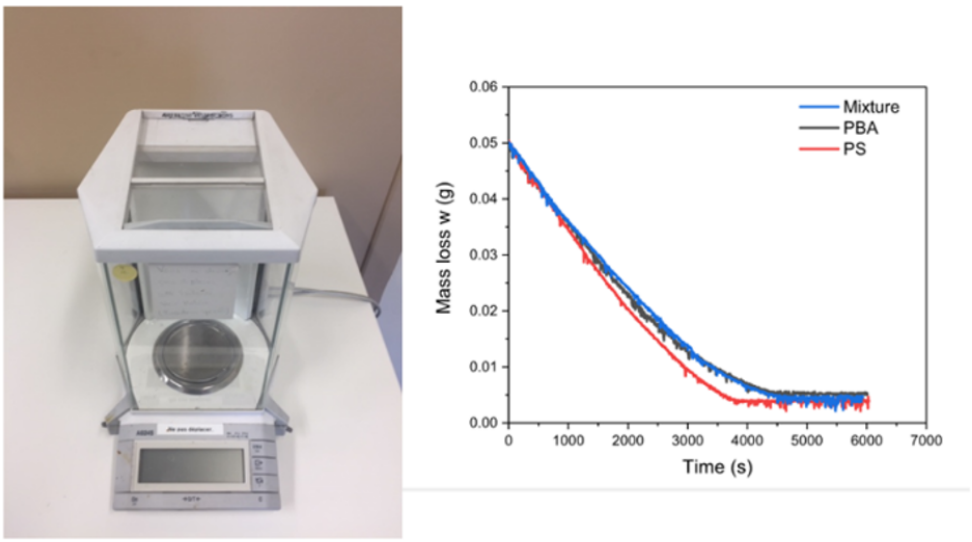

Figure 2.13: (Left) A Mettler balance. (Right) The loss of mass during drying three different colloidal suspensions in free air.

2.6.3 Drying under airflow

In this study we present a novel method for controlling the particle deposition in a periodic manner at the drying front via time modulated drying rate. The experimental setup consists of a small flat fan with a diameter of 3.2 cm and 0.7 cm wide, blowing air on the suspension (Figure 2.14a). A shutter, installed on the fan gate, was periodically closed and opened at different intervals. This was achieved by using a servo motor controlled by Arduino. A Tachometer device was used to measure the rotations of the fan and the distance between the sample and the fan was fixed at $\sim$ 6 cm. Figure 2.14 (b) shows a total time period (τ_p) of 20s, and the fractions of opening and closing periods were 50/50 %. In our experiments the airflow speed is varied between 7.86 and 48.72 cm/s (Figure 2.14c).
The period of airflow is τ_p ($\tau_p = t_{open} + t_{close}$) is varied between (0 and 120s).
The fraction of opening time : $\phi_t^{open} = t_{open}/(t_{open} + t_{close})$.

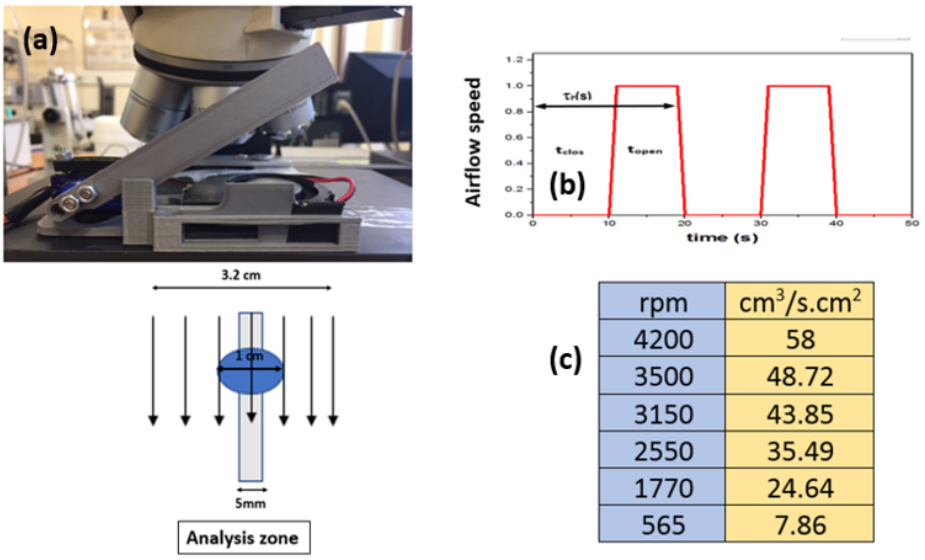

rpm	$cm^3/s.cm^2$
4200	58
3500	48.72
3150	43.85
2550	35.49
1770	24.64
565	7.86

Figure 2.14: (a) A photo of the drying system under a microscope. The system is composed of fan and an arduino controlled shutter. The bottom schema depict the process of drying the sessile drop (1 cm diameter) under a laminar air flow (3.5 cm wide). The long rectangle depicts the zone of interest for the morphology observations and analysis (b) A diagram depicting the periodic opening and closing of the shutter for a time t_{open} and t_{close} for a period of $\tau_p = t_{open} + t_{close}$.

2.6.3.1 Drying under continuous airflow

During measuring the mass loss under airflow, we were able to get some information and it is clear that the dying is faster as expected (Figure 2.15), it is almost half comparing to drying in free air (Figure 2.13 right). Furthermore, with PS it is even third while with PBA, it is even more slower because probably of skin formation. Therefore, drying was undergone by periodic airflow in order to obtain a more accurate value of the mass loss.

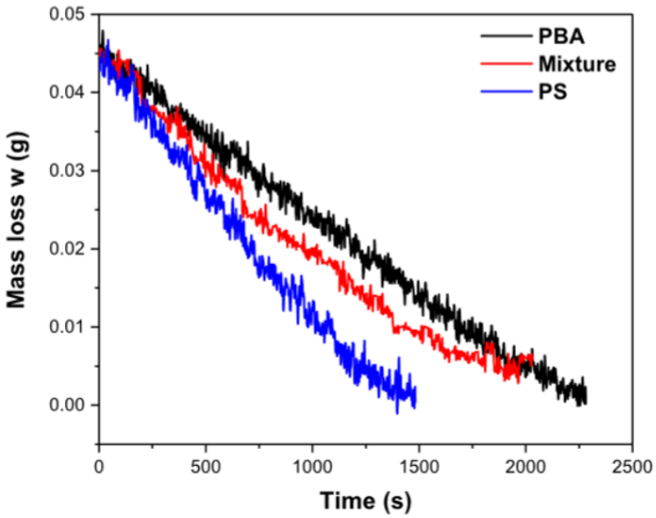

Figure 2.15: Mass loss during drying of PS, PBA, and their mixture under continuous airflow at 7.86 cm/s.

2.6.3.2 Drying under periodic airflow

The method relies on blown air periodically on a drop of colloidal suspension. When periodic drying, the mass loss was monitored only during gate closure periods (Figure 2.16). Blown air on the suspensions of PS, PBA, and their blends leads to a decrease in the mass loss with a similar tendency. Increasing ϕ_t^{open} with a constant τ_p was found to slightly increase the drying rate (Figure 2.17a), While, increasing τ_p with a constant ϕ_t^{open} (50%) was found to lead to an almost similar drying rate (Figure 2.17b).

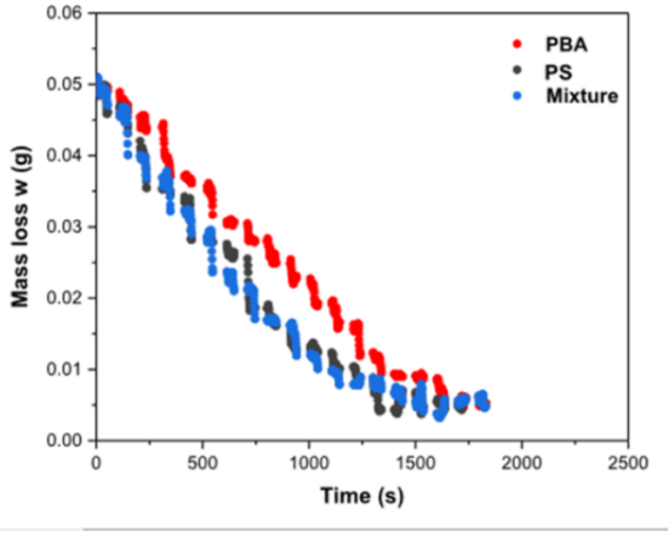

Figure 2.16: Mass loss during drying different colloidal suspensions under periodic airflow. (t_{open}/ t_{close}: (50/50%)) and τ_p: 20s at 7.86 cm/s.

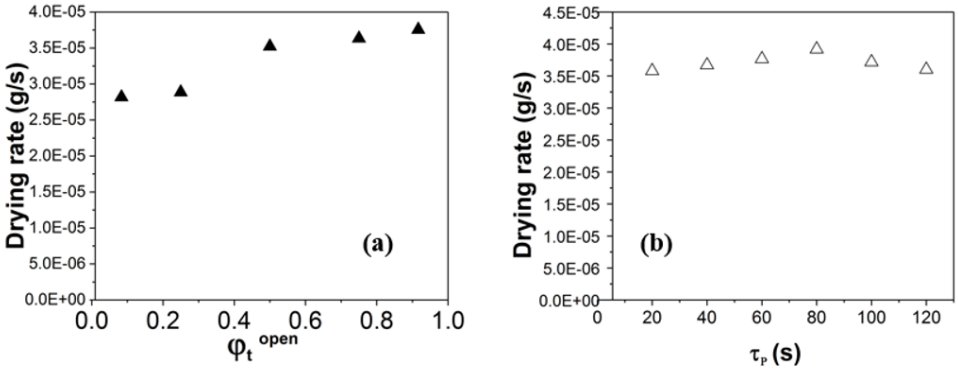

Figure 2.17: (a) Increasing ϕ_t^{open} with a constant τ_p leads to a slight increase in the drying rate. (b) While, increasing τ_p with constant ϕ_t^{open} (50%) leads to almost a similar drying rate.

2.6.4 Observation and analysis method of patterns

2.6.4.1 Observation

The Stripe patterns were observed with an optical microscope (LEICA, DMLM) during drying using 5x, 10x objectives and a digital Motic camera (Figure 2.18). The light source intensity was reduced in order to minimize heating of the samples. The image analysis was performed using Image J software and a home developed program in Matlab.

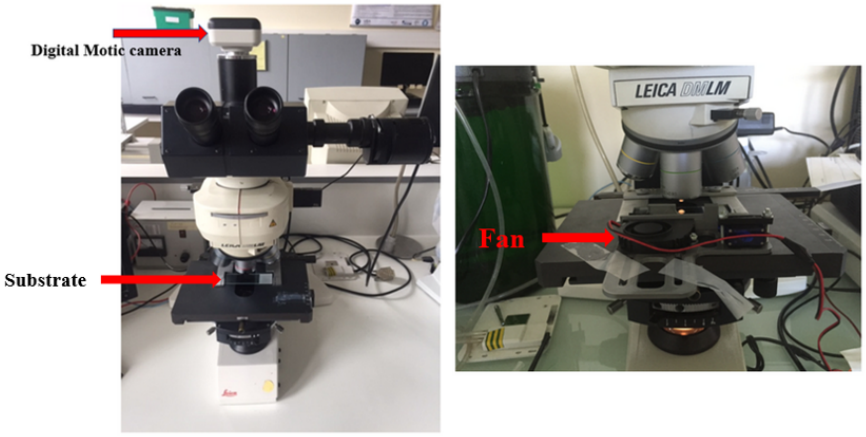

Figure 2.18: Optical microscope (LEICA, DMLM) linked to a digital Motic camera. (Left) Position of substrate. (Right) Position of fan during drying.

2.6.4.2 Program for analysing the drying front

This program was developed in order to follow the border of the drying front in each image during drying . The first image in the series is scanned to select the droplet edge and determine the position of the triple line by baseline, that means the symmetric line connecting the two points of the droplet edge. The boundary is then saved. Calculations are then carried out by following the advance of drying front in each image. These results are saved in column vectors. The first column corresponds to time and the second one shows the increment in the distance value as the drying front retreats inward. From these results, various parameters were calculated such as drying front velocity. The principle of this program is illustrated in Figure 2.19.

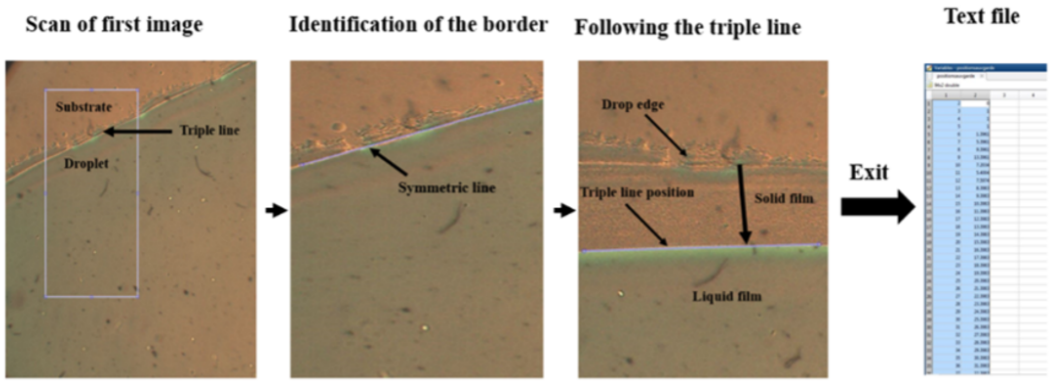

Figure 2.19: Diagram of the image processing program

2.7 Characterization of the 3D profiles by Profilometer

A contact profilometer device SM7 was used to characterize the film thickness (Figure 2.20). The measurement was carried out on intact films. The stress on the film was minimized in order to reduce the damage to the film. Due to the low resolution of the profilometer ($10\mu m$), we were unable to obtain accurate results for the purposes of our study. Figure 2.20 (a) shows the surface profile of a glass substrate measured with the SM7. From this profile, the roughness of the plate is estimated around $10\mu m$, while its real value is around 200 nm. This difference is attributed to the lack of precision of the SM7, due to the mechanical part of the device which limits the resolution. Therefore, a modification was done in order to provide a nanometric resolution (200 nm). The inset image circled in red (Figure 2.20) shows the modification made to the SM7 detection probe: a micrometric screw was adapted to the head of the original probe. This new device, enabled to obtain profiles with a resolution of the order of 200 nm (Figure 2.20b), comparable to the real roughness of the glass plate.
The obtained 3D profiles, shown in Figure 2.21, highlight periodic peaks resulting from the accumulation of particles at the pinned drying front, during periodic airflows. The height profiles of films depend on the period of opening and closing time as well as the migration of the particles towards the drop edge. These processes are enhanced by various parameters such as surfactant, ionic strength, and particle size and concentration. All of these processes will be explained in more detail in the following chapters.

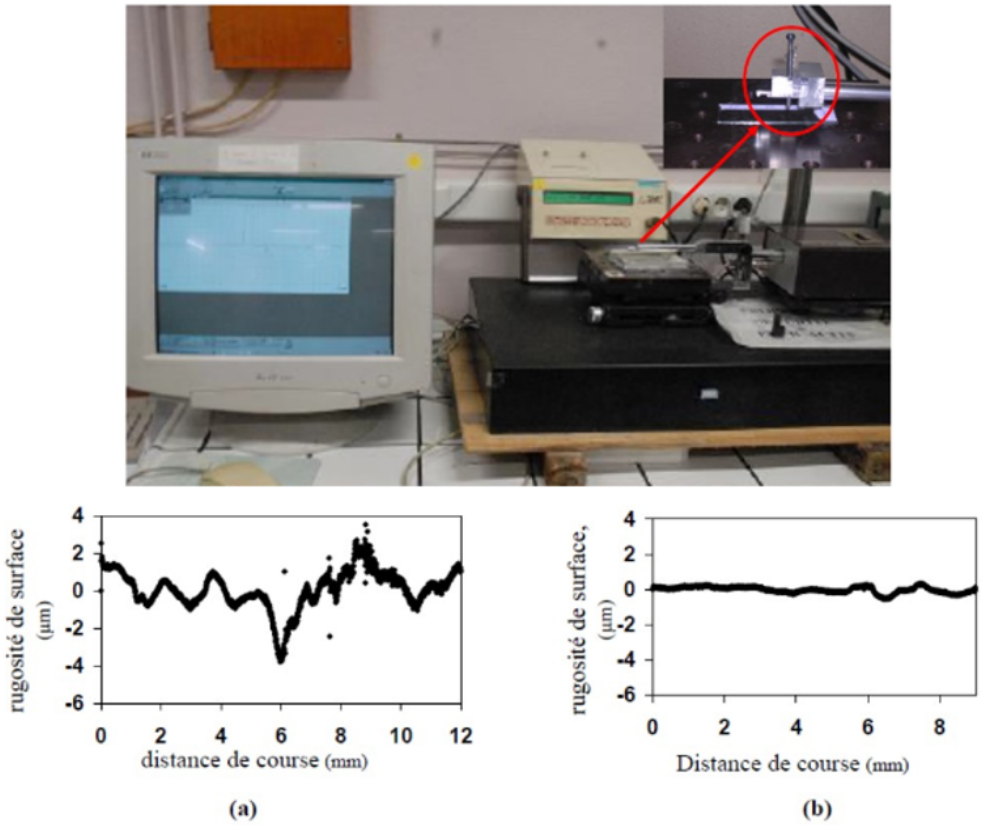

Figure 2.20: (Above) SM7 profilometer linked to a computer. (Below) (a) Substrate profile obtained by SM7 before modification, and (b) after modification of the detection prob.

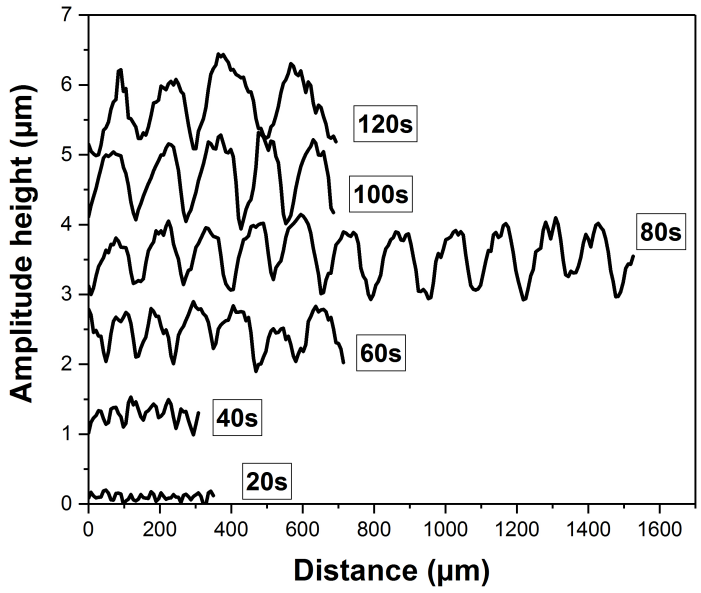

Figure 2.21: Height profiles of films made of (50/50%) PS(64nm)/PBA(97.5 nm) blends under periodic airflow for different time period τ_p from 20s to 120s. The height profile was measured using contact a profilemeter. The $t_{open}/\,t_{close}$ was set to 50/50%. The drying was carried out on glass substrate at room temperature 23^0C and humidity ratio of 34%. The blend concentration was 10 wt%. from bottom to top τ_p was 20 s, 40 s, 60s, 80 s, 100 s and 120 s. The profiles are estimated by taking the film surface as a baseline and shifted for clarity.

Bibliography

[1] Abdelaziz Nasr Moawed Bakr El-hoshoudy. Emulsion polymerization mechanism. *Recent Research in Polymerization*, page 1, 2018.

[2] Chourouk Mathlouthi. *Étude des propriétés thermodynamiques et dynamiques des polymères confinés en géométrie nanoparticules*. PhD thesis, 2016.

[3] W Steinmann, S Walter, M Beckers, G Seide, and T Gries. Thermal analysis of phase transitions and crystallization in polymeric fibers. *Applications of Calorimetry in a Wide Context-Differential Scanning Calorimetry, Isothermal Titration Calorimetry and Microcalorimetry*, pages 277–306, 2013.

[4] Lanhe Zhang, John A Marsiglio, Tian Lan, and John M Torkelson. Dramatic tunability of the glass transition temperature and fragility of low molecular weight polystyrene by initiator fragments located at chain ends. *Macromolecules*, 49(6):2387–2398, 2016.

[5] Martin E Sacks, Soo-il Lee, and Joseph A Biesenberger. Effect of temperature variations on molecular weight distributions-batch, chain addition polymerizations. Technical report, STEVENS INST OF TECH HOBOKEN NJ DEPT OF CHEMISTRY AND CHEMICAL ENGINEERING, 1972.

[6] Y Rharbi, B Cabane, A Vacher, M Joanicot, and F Boué. Modes of deformation in a soft/hard nanocomposite: A sans study. *EPL (Europhysics Letters)*, 46(4):472, 1999.

[7] Jeannine Stone-Masui and André Watillon. Characterization of surface charge on polystyrene latices. *Journal of Colloid and Interface Science*, 52(3):479–503, 1975.

[8] Jacob N Israelachvili. *Intermolecular and surface forces*. Academic press, 2011.

[9] Mohamed Yousfi. *La dynamique et Transition Vitreuse des Polymères Confinés dans des Domaines Nanométriques: dans les Nanomélanges et dans les Nanoparticules sur Substrat*. PhD thesis, 2010.

[10] Lanhe Zhang, Yen Nguyen, and Wei Chen. “coffee ring” formation dynamics on molecularly smooth substrates with varying receding contact angles. *Colloids and Surfaces A: Physicochemical and Engineering Aspects*, 449:42–50, 2014.

Chapter 3

Periodic surface-morphologies through temporal modulating the drying rate during evaporation of colloidal suspensions

Contents

3.1 Introduction

This third chapter is presented in the form of a scientific publication. In this chapter we develop a new a fast and simple method for producing ordered surface morphologies via evaporation of polymer colloidal suspensions by time modulating the drying rate. The moving and the arrest of the drying front can be tuned on demand using modulated drying rate in controlled physical chemistry. This process can take place for different types of colloidal particles such as polystyrene, poly-butylacrylate and their blends. The role of the drying conditions, the blend composition and particles size on the periodic patterns was investigated. The dynamic of the drying front is monitored in the different drying regimes and correlated with surface morphologies. A simple drying model was developed to account for the observed surface morphology by simulating the dynamic of the drying front under periodically modulated drying rate.

3.2 Periodic surface-morphologies through temporal modulating the drying rate during evaporation of colloidal suspensions

Essa shawail[a], *Yahya Rharbi*[a,b]
(a) Univ.Grenoble Alpes - LRP, F-38041 Grenoble, FRANCE
(b) CNRS, LRP , F-38041 Grenoble, FRANCE
Corresponding Author Email: yahya.rharbi@univ-grenoble-alpes.fr

Keywords: Colloidal suspension, drying front, surface patterning, evaporation, triple line.

Abstract

Making by design ordered morphologies from colloidal suspension is a challenge for numerous emerging technologies. Driving particle deposition in a periodic manner at the drying front during evaporation via the control of convective assembly is a promising method in this field. In this work, we propose an user-friendly convective method for assembling periodic 3D surface structures through modulating the evaporation rate. We show that the moving and the arrest of the drying front can be tuned via the control of the evaporation rate in certain colloidal suspensions and we demonstrate that this can be used to govern particles deposition on demand. Long-range periodic arrays are made by time modulated drying rate in a series of suspensions such as polystyrene, polybutylacrylates and their blends. These structures were predicted via a model which takes into consideration the dependence of the particle deposition and the dynamic of the drying front on the evaporation rate.

Introduction

Controlling the organization of colloidal particles on a solid substrate remains a pivotal challenge for many advanced technologies like photonic band-gap,[1] microelectronics,[2] self-cleaning surface,[3] optical components[4] and lab-on-ship.[5] This has motivated an ongoing decades of research activities to provide the basis for controlling colloids deposition dynamics.[6, 7] Local organization might be achieved to a certain extent via spin coating[8] electrostatic deposition,[9] Langmuir-Blodgett assembly,[10] sedimentation[11] and electro-phoretic deposition,[12] lithographic mask,[13] fingering instabilities,[14] spontaneous dewetting[15] and Self -Assembly, Transfer, and Integration.[16] Convective assembly has emerged as an easy to apply methods for assembling colloidal particles on the drying front during solvent removal by evaporation with a leaser technical complexity.[17–19] In this process the particles are driven towards the triple line where they are accumulated via convective flow induced by evaporation. These fabrication strategies relay on governing the deposition patterns based on the mechanism of coffee ring where preferential deposition of particles is dominated by the synergy between triple line pining and capillary flow.[20] The pinning and arresting of triple line during drying are fundamental in the dynamics of droplet evaporation process.[21, 22] Therefore, the surface patterning can be achieved via fine control of such process when preferential drying takes place on the triple line or on the drying front.[23–26] For example, dip coating with either liquid[27] or substrate withdrawal[18] or doctor blade[28] leads either to uniform or structured surfaces depending on the drying regime. In both Landau-Levich and capillary regimes, uniform films with modulated thickness can be achieved by controlling evaporation rate, triple line speed, the suspension and substrate properties. [29, 30] Here physicochemical of the suspension and the substrate plays a significant role in particles deposition and structuration. Template-directed assembly is an example where the capillary flows close to drying front is used to achieve ordered structures with a critical ordered size and morphology dependent on the template structure.[31] The contact line undergoes a stick-slip mechanism at a certain conditions within the capillary regime of the dip coating leading to ordered structures.[32] This results from the balance between capillary flow which brings the fluid towards the triple line and the capillary forces which controls the line retraction. This process is numerous parameter dependent: colloidal interactions, surface tension, viscosity, substrate polarity, surface roughness, volume fraction, temperature, humidity.[33–38] Periodic stripes of colloids suspension can be formed via periodic moving of the triple line by mechanically moving the substrate, doctor blade or the suspension. In such process the precise position of the triple line is controlled by the mechanism of the particle deposition at the drying front via convective flow.[19] However, integrating such process in large-scale fabrication is a challenging and requires meticulous technical conditions, which could hinders their potential scale up to become a valuable industrial process. Therefore, there is still a need for a fast, simple easy to implement method to produce ordered surface morphologies

with a mildly controlled conditions. This work proposes a fast and simple method for producing ordered surface morphologies via evaporation of polymer colloidal suspensions by time modulating the drying rate. The moving and the arrest of the drying front can be tuned on demand using modulated drying rate in controlled physical chemistry. This process can take place for different types of colloidal particles such as polystyrene, poly-butylacrylate and their blends. The role of the drying conditions, the blend composition and particles size on the periodic patterns was investigated. The dynamic of the drying front is monitored in the different drying regimes and correlated with surface morphologies. A simple drying model was developed to account for the observed surface morphology by simulating the dynamic of the drying front under periodically modulated drying rate. The general tendency of the observed moving and arrest of the drying front and the resulting surface morphologies were predicted using such model.

Experimental

Materials and particle preparation

Particles are prepared using styrene (Aldrich, 99%) and butyl acrylate (BA, 99% Aldrich) monomers and distilled water. Both of the surfactant sodium dodecyl sulfate (SDS, Aldrich, 99%) and the initiator potassium persulfate (KPS, Aldrich, 98%) were used as received. Polystyrene (PS) and butyl polyacrylate (PBA) suspensions were prepared in batch emulsion polymerization. Monomers, surfactant, and water were mixed in a standard three-neck round flask (500 mL) with a condenser under nitrogen flow and heated to 74^0 C and the initiator was added when the mixture reached the desired temperature. The particle size was controlled by varying the amount of SDS surfactant. The solid content of the particles was 10 wt.%. The synthesized latex were cleaned using a mixture of anionic and cationic exchange resins (DOWEX Marathon MR3, Aldrich). The suspensions were mixed with 5 wt. % resin, agitated gently for several minutes, and then filtered to remove the resin. During cleaning, the conductivity was monitored after each cleaning step and the procedure was repeated several times until a constant conductivity value was obtained.

Polymer and Particle Characterization

Particle diameter was measured by dynamic light scattering (DLS) using a Zetasizer (Malvern 5000) device with an angle of 90^0. The particles size were for PS (64 and 280.1 nm) and for PBA 97.5 nm. The Differential Scanning calorimetry measurements (DSC) were carried out using a Mettler-Toledo DSC823 device with heating and cooling speeds 10^0 C / min, in a temperature range from -50^0 C up to 140^0 C. The glass transition temperature (T_g) was evaluated to be 100^0 C for PS and -49^0 C for PBA.

Drying system

The drying system is a home built device equipped with a small flat fan (Figure 3.1a). The fan speed is controlled using PMW signal and monitored using tachometer leading to constant speed from 565 rpm to 4200 rpm. This yields an air flow of $2x10^{-4}$ to $1.6x10^{-3}$ m^3/s. Taking into consideration the opening of the fan (0.7 x 3.2 cm) , the velocity of the air were set 7.86, 24.6, 35.5, 43.9 and 48.72 cm/s. In all the experiments the air flow was limited in order for the sessile drop to remain stable and this set an upper limit of air flow of 48.72 cm/s. The periodic air flow is tuned by periodically opening and closing a shutter on the fan gate using an arduino controlled servo for different time intervals t_{open} and t_{close} which varied between 10s and 60s. The period of airflow is calculated as $\tau_p = t_{open} + t_{close}$ leading to a period between 20 s and 120s. The fraction of opening time is estimated as $\phi_t^{open} = t_{open}/(t_{open} + t_{close})$ leading to ϕ_t^{open} between 10%

to 90%. The drying system was either placed on Mettler balance to measure the drying rate during periodic air flow or on a microscope to observe the evolution of the structure throughout the drying. In all cases the distance between the drop and the fan opening was set to $\sim$ 6 cm. The substrate, glass microscope slides (1x 76 x 26 mm), which were previously cleaned using alcohol and distilled water and left to dry. The glass slide is first placed on the drying system and then a $\sim$ 0.05 ml of the latex suspension were deposited using the glass slide leading to a circular drop of around $\sim$ $1cm$. The drying environment was kept at 23^0C and humidity ratio of 34%. The mass loss during drying was measured using a Mettler balance with precision 0.01 mg connected to a computed with home-built software. When periodic drying the mass loss was monitored during gate closure periods. Several suspensions were used for the drying process PBA (97.5 nm), PS (64 nm) and PS (280.1 nm) as well as their blends. The initial concentration of the suspensions is 10 wt.%. The blends were prepared by mixing the cleaned PBA and one of the two PS suspensions at different fractions between PS/PBA between 0% and 100%. All the following experiments are carried out with PS (64 nm) and its blends except when mentioned.

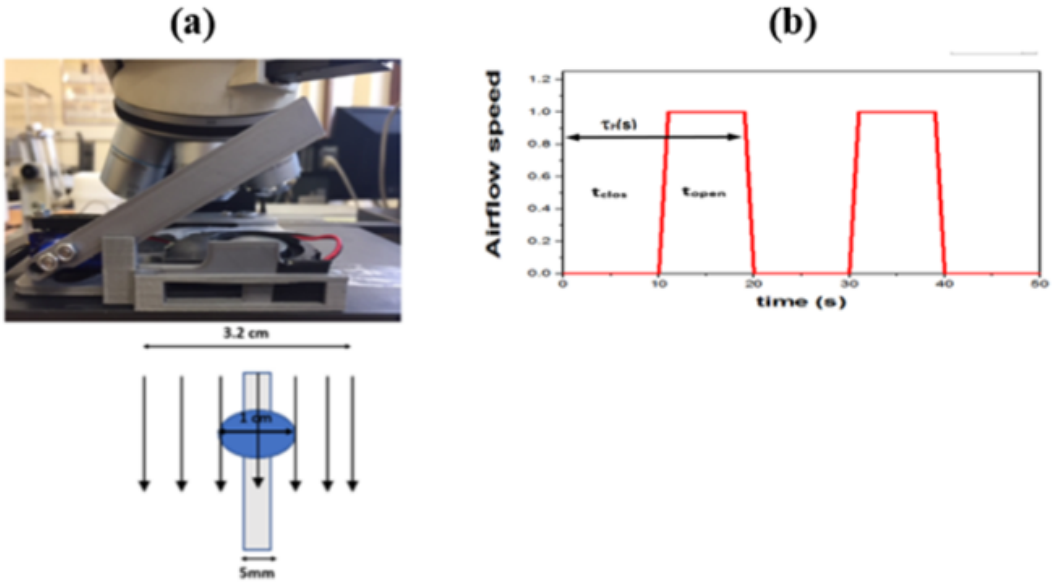

Figure 3.1: (a) A photo of the drying system under a microscope. The system is composed of a fan and an arduino controlled shutter. The bottom schema depict the process of drying the sessile drop (1 cm diameter) under a laminar air flow (3.5 cm wide). The long rectangle depicts the zone of interest for the morphology observations and analysis. (b) A diagram depicting the periodic opening and closing of the shutter for a time t_{open} and t_{close} for a period of $\tau_p = t_{open} + t_{close}$.

Observation and analyses

The patterns formation were observed using an optical microscope (LEICA, DMLM) throughout the drying process using 5x or 10x objectives. The light source intensity was optimised to reduce light heating effect. The image analysis was performed using Image J software and home developed program in the Matlab. A home built Matlab program was used to automatically follow the drying front advance using the Canny method for edge detection. A modified contact profilemeter device SM7 was used to characterize the film thickness profiles. This device give a depth precision down to 100 nm. This was carried out on cracks-free films. The stress on the film was reduced in order to reduce the damage to the film. When films are cracked, a tiny portion of the film was adhered to the glass substrate and the measurement were carried with even slighter stress.

Results

Drying rate in periodic air flow

Figure S3.1 (Supporting Information), shows the time resolved mass loss during drying a sessile drop of PS(64 nm), PBA (97.5 nm) as well as their 50/50% blends PS/PBA in the absence and presence of air flow. The drying kinetic, in the absence of air flow, follows the general tendency of evaporating colloidal suspension with two regimes: a linear dependence of the mass loss vs. time and a constant drying rate in the early time and a deviation from the linear behavior and decreasing drying rate at advanced time. The two distinct drying regimes become even more enhanced when the drying rate increases with increasing air flow. At least in the absence of air flow, drying colloidal suspension can be considered to be controlled by vapor transport across the air boundary layer adjacent to the surface as well as the concentration of water on the interface. At early drying time, the particle concentration is homogeneous across the film leading to a constant evaporation rate which is dominated by vapor transport. Because particle diffusion is slower than water evaporation a concentration gradient develop in the film starting from the film surface leading to crust on the film surface, which inhibits water evaporation and reduces the drying rate. A main observation is that the drying kinetics of PBA deviates from the linear behavior much faster than PS and their blends. One can explain this by the softness of PBA ($T_g = -49$) which form continuous film at room temperature which inhibits water evaporation. In contrast, the PS remains hard and spherical during drying allowing water to evaporate through the porous crust. Interestingly, the PS/PBA (50/50%) is found to follow the same tendency as the PS inferring that in the blends conditions, the drying mechanism is dominated by the hard particles. Increasing the drying rate using air flow enhances the deviation from the linear behavior particularly in the case of PBA and accentuates the difference between the soft PBA and the hard PS particles. The formation of crust is dominated by the ratio of the drying rate and the particle diffusion coefficient which explains the difference between PBA and PS. Figure 3.2 depicts the mass loss under periodic airflow for various periods τ_p as well as the opening t_{open} and closing t_{close} times. In all cases, the drying kinetic is found to lie between the no air flow regime for $\phi_t^{open} = 0\%$ and the full air flow regime $\phi_t^{open} = 100\%$ curves, which suggests that the drying rate E_v oscillates between a low value for t_{close} and a higher one for t_{open}. Figure 3.2a and (S3.2a Supporting Information) suggest that ΣE_v increases rapidly for low t_{open}/t_{close} 10/110s and then slower at higher t_{open}/t_{close} when t_{open} is kept constant Figure 3.2b and (S3.2b Supporting Information). One would expect ΣE_v to increase linearly with increasing ϕ_t^{open} if the evaporation regime relaxed back rapidly after closing or opening. This is not the case here which could suggest that the dynamic of transition between these two regimes of evaporation is slow compared to t_{open} and t_{close} investigated here. This could infers that the evaporation regime return back rapidly during t_{open} as the vapor concentration in the boundary limit is washed out

under air flow. On the other hand, the return to the regime of diffusion limited regime after ceasing air flow t_{close} is slower and therefore E_v remains always higher than that in the absence of air flow at least for t_{open} and t_{close} investigated here leading to the observed ΣE_v. To understand the dynamic of transition between these two regimes of evaporation one needs to evaluate the characteristic time of the transient regime and particularly between air flow to non air flow. A rough estimation of this time was found to yields about 10% of the total drying time [39, 40] which gives few tens of second, which is in the same order of magnitude of t_{close}. During the transient state after ceasing air flow, E_v decreases to approach the value of no air flow but most likely does not reach the steady state within the investigated t_{close} (10s to 60s). This was also comforted by the fact that ΣE_v was found almost independent on τ_p for constant t_{open}/t_{close}.

If one assumes that in the absence of air flow the drying is diffusion controlled, the drying rate can be written as.

$$E_v \sim A D_s C_{sat} \tag{3.1}$$

Where C_{sat} is the saturated water vapor pressure, D_s is water diffusion coefficient in air and A is the area in the case of large drop. In the case of small drop where the drying rate is the triple line dominate evaporation, the drying rate becomes

$$E_v \sim D_s C_{sat} R \tag{3.2}$$

Where R is the drop radius. Once air is blown on the film, the drying becomes forced convection leading to higher evaporation rate. Several empirical equation were proposed to describe the evolution of the drying rate vs air speed. [40] In conclusion the drying rate evolve periodically between two states high evaporation and lower evaporation regimes. However, the present results infers that transition between high E_v to low E_v is not sharp but evolves as transient state toward the steady state and this process is repeated periodically.

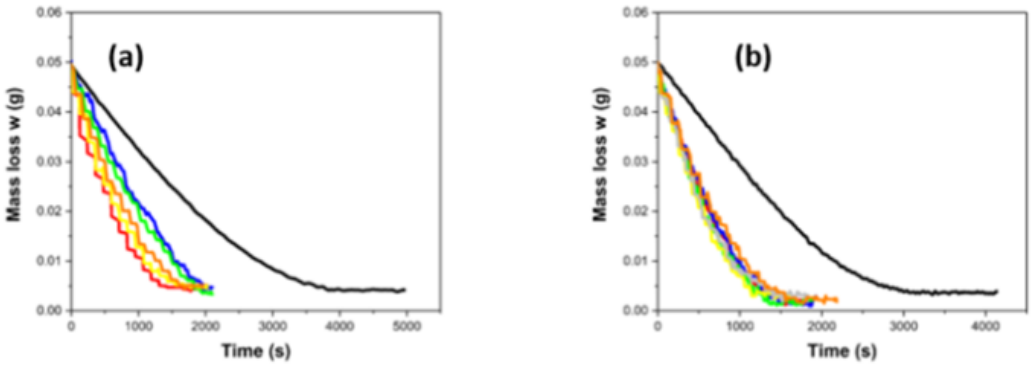

Figure 3.2: Drop weight loss (w) as a function of the drying time in mixture 50% 50% PS(64 nm) /PBA(97.5 nm) in free air and under periodic airflow at flow rate 7.86 cm/s. (a) The τ_p was (120s) and the opening closing time steps were varied : (10s on /110s off) (Blue),(10s off /110s on) (Red) , (60s on/ 60s off) (Orange), (30s on/ 90s off) (Green), (30s off/ 90s on) (Yellow), and in free air (Black). (b) The $t_{open}/\ t_{close}$ was fixed at (50/50%) and time period τ_p was varied from 0 to 120s: 20s (Red), 40s (Blue), 60s (Green), 80s (Yellow), 100s (Gray), 120s (Orange), and in free air (Black).

Shape patterns of the dried film under periodic air flow

During drying concentrated latex suspension under normal condition or under continuous air flow, the drying front moves steadily starting from the edge and result in uniform film without any particular induced structure. In this conditions of high concentration and relatively higher drying rate, the movement of the drying front does not leads to any stick slip resulting morphologies likewise those observed in triple dynamic at certain drying conditions.[41] On the other hand, under periodic air flow, a periodic structure of parallel strips is formed, starting from the film border. This is well seen in the microscopy images and particularly in reflection mode for PS, PBA and their blends. From the first glance the morphology are most likely composed of hills and valley formed during displacement of the drying front. These structures form periodic patterns with a period λ_p which is uniform on the border and in most cases becomes disturbed while approaching the center. In the geometry investigated here, λ_p slightly decreases as one approaches the directions normal to the air flow and in the extreme case it decrease by about 30% (Figure S3.3 Supporting Information). This is expected since the air flow breaks the symmetry of the drop but does not affects the results particularly in the air flow direction. In the following all the analysis are carried out within $\sim 20^0$ of the normal direction where the deviation of λ_p is less than 5%.

Effect of polymer nature

Figure 3.3 shows the periodic structure made under period air flow in different types of suspension hard PS, soft PBA and their blends. The periodic lines stripes superpose with the drying bands that usually forms on the top layer during drying hard colloidal suspension.[42]

Yet the depth and the period of these stripes are much larger than that of the shear bends.[42] One should note that the two structures coexist but do not clearly influence each other inferring that they are caused by different mechanisms. Furthermore, as the periodic patterns appears and evolves during PS (Figure S3.4 Supporting Information), the solidified structure accumulates stress leading the film to crack into millimeter size fibers that delaminates from the substrates (Figure S3.5 Supporting Information). This is expected because consolidation of the hard PS particles ($T_g = 100^0C$) generates capillary pressure on the top layer of the wet films causing it to crack and to delaminate.[43, 44] The parallel stripes also form in the soft PBA particles ($T_g = -49^0C$) for all investigated conditions (Figure S3.6 Supporting Information). However, these stripes appear shallow in both reflection or transmission mode which suggests that their depth is not as pronounced as in the case of PS. This can be explained by the role of the capillary forced in smoothing the surface of soft PBA film. On the other hand, when films were made by drying blends of PS and PBA at the composition in the range of 70/30% to 30/70%, the periodic parallel stripes forms and remains after complete drying with well pronounced depth and without crack, which allows further morphological analysis. For these compositions no crack and no delamination were observed.

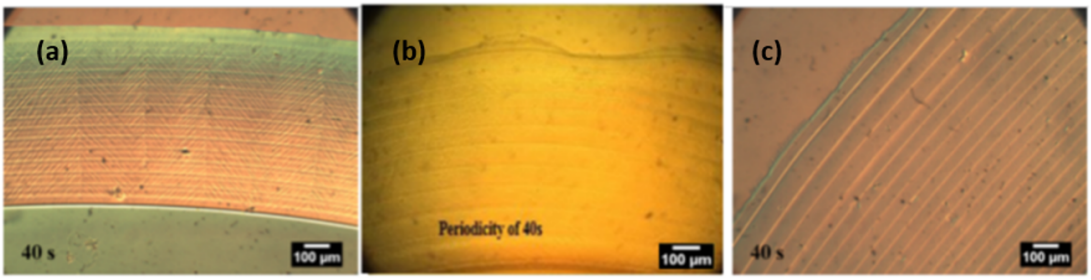

Figure 3.3: Optical microscopy images of stripes pattern of films made by drying sessile drops of three types of suspension (PS, PBA and their blends), under periodic air flow. The periodic airflow is controlled by a fan with arduino controlled shutter. The time period $\tau_p = 40$ s and $t_{open}/\,t_{close}$ was 50/50%. The drying was carried out on glass substrate at room temperature 23^0C and humidity ratio of 34%. (a) Drying a suspension of PS with diameter 64 nm and 10 wt %, (b) a 10 wt % of PBA suspension with diameter 97.5 nm, (c) 50/50% blends of PS (64nm) and PBA (97.5nm) at 10 wt %.

Effect of the drying condition on the periodic patterns

In figure 3.4 we show microscopy images of different films made by drying 50/50% blends of PS/PBA under periodic air flow for different air flow period τ_p and constant ϕ_t^{open} 50/50%. In all the studied cases, a periodic pattern of stripes is observed starting from the film border. The period clearly increases with increasing τ_p. This is well depicted in Figure 3.5 which shows λ_p increases almost in linear tendency with increasing τ_p. From the present experimental conditions one can obtain periodic patterns with period λ_p ranging from $25\mu m$ up to $140\mu m$. The same behavior is observed for the all air flow speed investigated here from 7.86 cm/s to 43.85 cm/s which slight increase of λ_p with increasing air speed. This suggests that these structures are more sensitive to the periodicity of the two drying regimes: the high drying rate and slower one. The depth profile of these periodic patterns is obtained using 3D contact profilemeter particularly for slightly tough films which are less sensitive to abrasion. In Figure 3.6 we show typical depth profiles for the films shown in Figure 3.4. The main information taken from these plots is the depth of the structure which is found to be in μm scale and clearly increases with increasing τ_p from 0.2 μm to 1.1 μm (Figure 3.7a). This infers that decreasing the period λ_p by reducing τ_p makes these structures shallow and converge towards making uniform films at low τ_p.

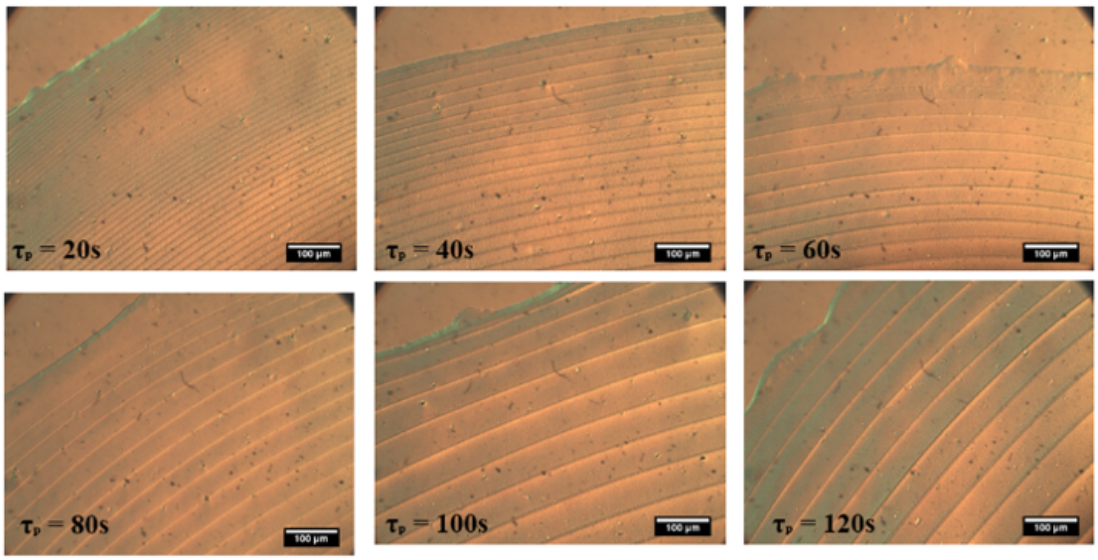

Figure 3.4: Optical microscopy images of stripes pattern of films made by drying sessile drops of 50/50% blends of PS (64nm) and PBA (97.5 nm) under periodic airflow. The periodic airflow is controlled by a fan with arduino controlled shutter. The $t_{open}/\ t_{close}$ was fixed to 50/50% and the time period τ_p was set to 20 s, 40s, 60s, 80s, 100s and 120s. The drying was carried out on glass substrate at room temperature 23^0C and humidity ratio of 34% and airflow rate was 7.86 cm/s. The blends concentration was 10 wt%.

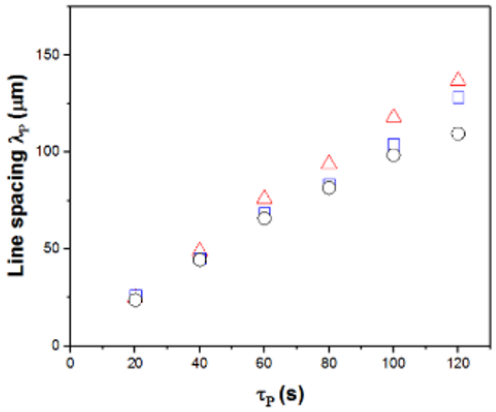

Figure 3.5: Average line spacing (λ_p) of the periodic patterns measured from microscopy images(figure 3.4) of dries films of PS(64nm)/PBA(97.5 nm) blends under periodic airflow plotted vs. τ_p. The films were dried under periodic air flow with fixed $t_{open}/\ t_{close}$ (50/50%) and variable τ_p between 20 s to 120 s. Three air speed values were investigated : 43.85 cm/s(△), 24.64 cm/s (□) and 7.86 cm/s (○).

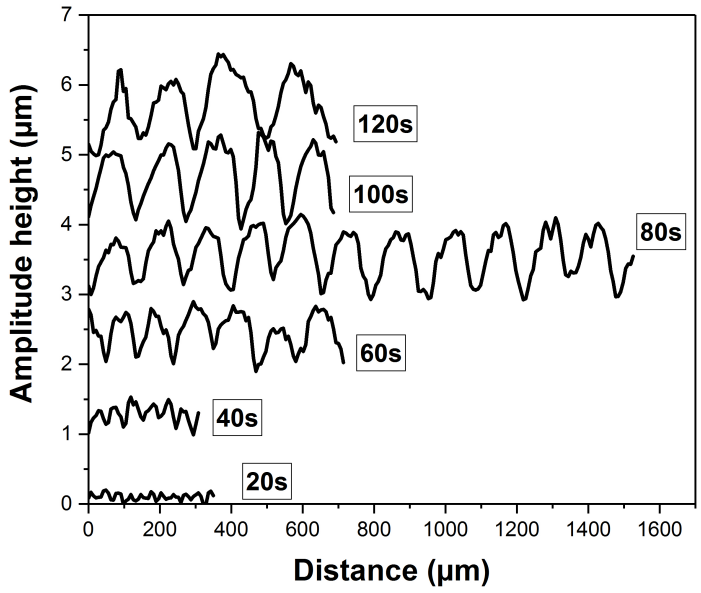

Figure 3.6: Height profiles of films made of (50/50%) PS(64nm)/PBA(97.5 nm) blends under periodic airflow for different time period τ_p from 20s to 120s. The height profile was measured using contact a profilemeter. The $t_{open}/\,t_{close}$ was set to 50/50%. The drying was carried out on glass substrate at room temperature 23^0C and humidity ratio of 34% and airflow rate was 7.86 cm/s. The blends concentration was 10 wt%. From bottom to top τ_p was 20 s, 40 s, 60s, 80 s, 100 s and 120 s. The profiles are estimated by taking the film surface as a baseline and shifted vertically for clarity.

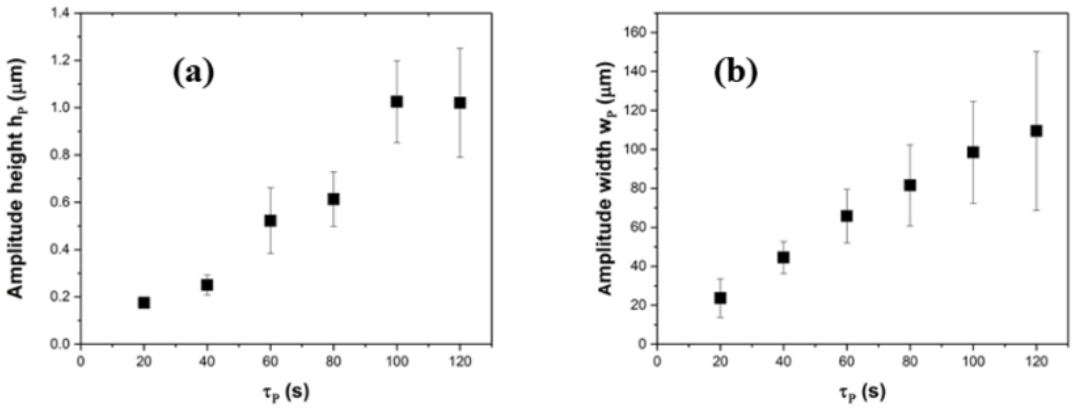

Figure 3.7: (a) Average amplitude and (b) width of the periodic patterns estimated from figure 3.6 and plotted vs. τ_p. The airflow rate was 7.86 cm/s, the $t_{open}/\ t_{close}$ is (50/50%) and the blends dried at room temperature 23^0C and humidity ratio of 34%.

Effect of the blend composition and particle size on the periodic patterns

The effect of blends composition on the periodic patterns was investigated using 2 types of PS/PBA blends containing one soft PBA (97.5 nm) particles and two hard PS particles with different sizes 64 nm and 280.1 nm. In the case of PS(64 nm)/PBA (97.5 nm) the blends composition was found to have a slight effect on the pattern period at least in the range of blend composition where no cracking takes place and where the capillary forces can not smooth the patterns namely from 70/30% to 30/70% (Figure S3.7 Supporting Information). This can be seen in the limited dispersion of $\lambda_p/\lambda_p^{reference}$ vs.τ_p where the sample 50/50% is chosen as the reference sample ($\lambda_p^{reference}$). On the other hand, the presence of the large PS particles 280.1 nm affects drastically the periodic structure under periodic air flow. This is well depicted in Figure S3.8 (Supporting Information), which shows the microscopy images of films made from blends PS 280.1 nm and PBA 97.5 nm with different composition. In all cases, the structure remains slightly periodic for low PS fraction however the period λ_p is found to increases with increasing the PS composition far beyond the error bar of these measurement. Especially beyond 20% PS λ_p becomes highly dependent on PS concentration and eventually looses some aspects of its periodicity (Figure 3.8). It is clear that increasing the concentration of large polystyrene particles has a major effect on periodic structure. These behaviors could result from i) particle polarity, ii) particle softness, iii) particle size, iv) viscosity. Indeed, the PS and PBA have different $T_g(100^0C)$ for PS and (-49^0C) for PBA, different polarity, and sizes. Therefore, the PBA fuses to form a hydrophobic film during drying, the PS particles remain hard and expose their surface electrostatic charges. This could attribute to the drying front a higher polarity and therefore leads to a reduced curvature, which can

affect the capillary flow and the dynamic of the drying front. However, this mechanism occurs in both small and large particles and therefore can not explains the difference between these two types of blends. Furthermore, several studies have pointed out the effect of particle size on the particle deposition at the drying front. Indeed, the small and the large particles can be deposited at different locations on the drying front.[45] This can induce segregation at different length scale from the small particle size blend and different properties of the drying front. This could give some staring hints to explain this process.

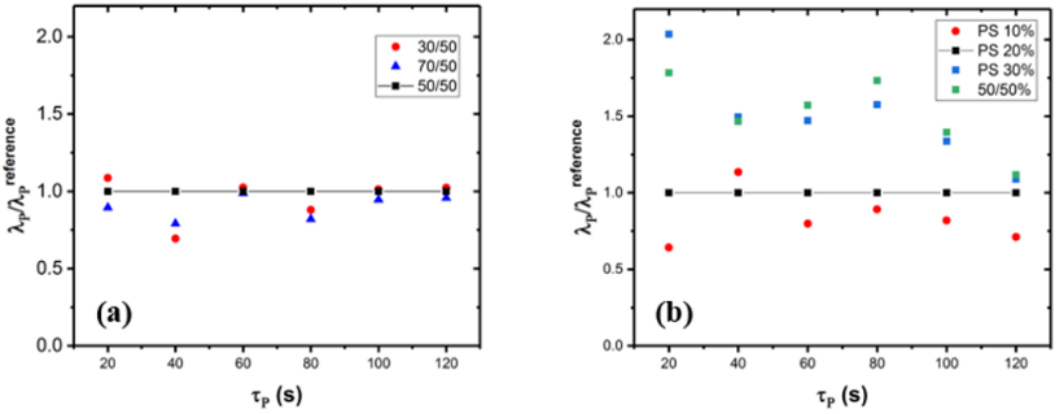

Figure 3.8: Evolution of the ratio of λ_p by $\lambda_p^{reference}$ vs. τ_p for two types of blends a) PS(64nm)/PBA(97.5nm) and b) PS(280.1nm nm)/PBA(97.5nm) and different PS/PBA fractions. $\lambda_p^{reference}$ is chosen as λ_p for the sample the PS/PBA 50/50% in the case of PS(64nm)/PBA(97.5nm) (a) and PS/PBA 20%/80% (b). The films are made by drying blends of PS and PBA with different composition under periodic air flow. The air flow rate was 48.72 cm/s. The $t_{open}/\,t_{close}$ is (50/50%) at room temperature 23^0C and humidity ratio of 34%. (a) $\lambda_p/\lambda_p^{reference}$ for the case PS (64 nm) and PBA (97.5 nm) with different composition of PS and PBA 30%/70%, 50%/50% and 70%/30%. (b) $\lambda_p/\lambda_p^{reference}$ for the case of PS (280.1 nm) and PBA (97.5 nm) with different compositions 10%/90%, 20%/80%, 30%/70% and 50%/50%.

Formation and evolution of the patterns

The formation of surface structure most likely results from the dynamic of pining and depinning of the drying front, which yields a preferential deposition of particles on the drying front.[46] Therefore, understanding these structures can be achieved if one comprehends the dynamic of the drying front during periodic airflow. In the absence of airflow the drying front advances steadily from the border of the drop towards the center. This process is assimilated to the "coffee ring" effect where drying rate is higher at the border than in the center and therefore the suspension becomes more concentrated and eventually goes through the liquid/gel/solid faster on the border. This transition can be visualized in microscopy via change in light absorption, birefringence, turbidity, light reflection.

Indeed, the drying front seen in our visualisation is a zone of a typical width between 65 μm to 117 μm (in the conditions of low airflow speed), depicting the transition between the liquid state and solid state. This area is composed of 2 domains with different aspects separated by 3 lines (Figure 3.9). The first one characterized by a change in the film coloration with a typical width of 26 μm -58.5 μm (in our experimental condition of low air flow speed), starting at an onset line (OL) and ending at a first line (FL). This zone corresponds to the transition between a colloidal gel to a solid film. The second zone is wider area characterized by shear bands lines particularly during air flow regime and extends to about starting at the FL and extending to a second line (SL). When particles are incorporated as tracer in the suspension to characterise the flows, no activity is seen in this zone. In the following we call the onset line the drying front. During drying this transition zone moves towards the center as the drying advances (Figure 3.10). It has been found that the width of drying front in normal drying condition is sensitive to the physical chemistry of the suspension specially the ionic strength and decreases with increasing the ionic strength.[47] when applying periodic air flow, the drying front moves in a periodic way; it advances during air flow and almost arrest when air flow stops (Figure 3.11a and Figure S3.9). The onset line (OL) clearly moves in a periodic way with a fast advances during air flow and slower advance or arrest during no air flow, depending on the experimental condition (Figure 3.11a and Figure S3.9). The first line (FL) also advances in a a periodic manner with a slight difference particularly at higher air speed (Figure S3.9). Although it is clear that the second line advances ahead of the OL, the contrast is not sufficient to resolve its position with the required precision to state on the periodicity of the movement (Figure S3.9). Figure S3.10 shows the time evolution of the width of first zone of the drying front between FL and OL (FL- OL) during periodic airflow as well as the total width of the drying front (SL-OL). Although the data are noisy they are clearly not constant during the periodic air flow, suggesting that these widths evolve during the change of the air flow regimes. This could suggest that there is an evolution of the ionic strength in the vicinity of the drying front during the transition between these two drying regimes. Indeed, the change in the drying regimes leads to

evolution of the vertical and horizontal concentration gradients which could affects the aggregation state of the suspension and consequently the width of the drying front. The dynamic of the advance of this front depends on several parameters such as the ionic strength, the critical concentration for gelation or aggregation, etc.[22, 47] The average speed of the drying front advance (OL) is also calculated for both the moving and stopping step and plotted vs. the opening/closing time period τ_p. Figure 3.11b shows that for all the time period τ_p investigated here, the speed of the fast advancing step (F_{smove}) is much higher than the slow step ($F_{sarrest}$). Moreover, the speed of the advancing part increases with increasing τ_p in a non linear way; it increases faster for higher τ_p values (Figure 3.11b). It is interesting to notice that the drying front speed during free air drying ($F_{freeair}$) is located between (F_{smove}) and ($F_{sarrest}$) suggesting that after air flow stops, the drying front relaxes and moves back to compensate the rapid advances during air flow, which gives the impression of complete drying front stop. The drying front advances (F_{smove}) for PS was found to behave almost the same as the mixture PS/PBA with increasing the τ_p and clearly higher than that of pure PBA (Figure 3.12a). This result suggests that the importance of properties of the polymer particles on the dynamic of drying front. The difference between the PBA suspension and PS and the PS/PBA mixture is polarity of the polymer that could lead to different shapes of the front as well as the gelation concentration and dynamic. These could intervene in the dynamic of the drying front under different drying conditions and therefore it might influence the periodic structure formation. Another explanation could be the softness of the PBA which has a T_g of -49 $°C$ and could form a film at room temperature and exposes the hydrophobic core of the PBA particles in the vicinity of the drying front. When air flow rate A_{fr} was varied between 7.86 cm/s and 43.85 cm/s , the dependence F_{smove} on τ_p was found similar as shown above however the magnitude of F_{smove} was found to be particularly dependent on the magnitude of air speed (Figure 3.12b). For example, F_{smove} ranged from 2.4 μm/s to 3.5 μm/s for $A_{fr} = 7.86\ cm/s$, and from 7.3 μm/s to 27.5 μm/s for A_{fr}= 43.85 cm/s (Figure 3.12b). This result suggests that the importance of the dynamic of the drying front when it exposed to two different drying regimes diffusion controlled and forced convective. The transition between these two regimes controls the way water is transferred and the dynamic of the drying front during this transition.

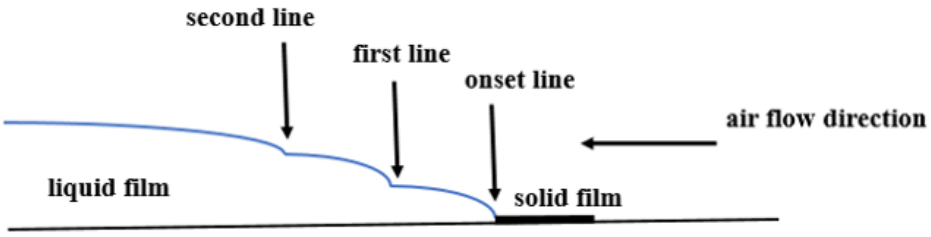

Figure 3.9: Schema shows the zones of the drying front during drying the sessile drop (1 cm diameter) under a laminar air flow (3.5 cm wide). The onset line (OL) close to solid film while second line (SL) close to liquid film and the first line (FL) is located between OL and SL.

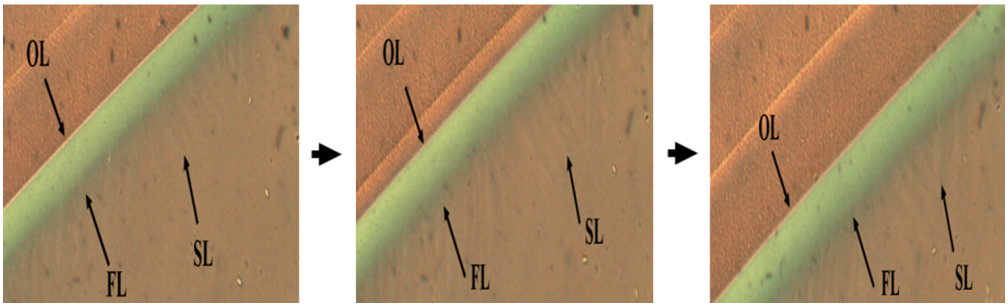

Figure 3.10: The motion of the onset line (OL), first line (FL) and second line (SL) of the drying front during drying a mixture of clean suspension of (PS/PBA) under periodic airflow $\tau_p = 50/50\%$. The drying was carried out on glass substrate at room temperature 23^0C and humidity ratio of 34% and airflow rate was 7.86 cm/s.

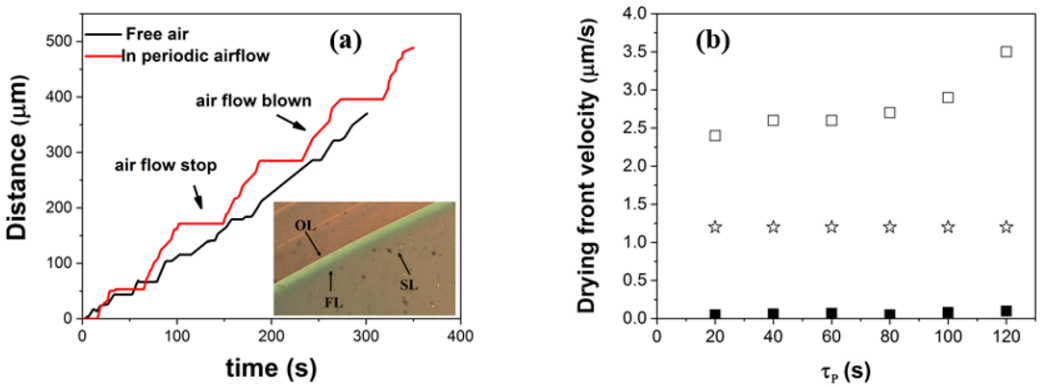

Figure 3.11: (a) Position of the dying front from the border during drying a sessile drop of blend made of 50%/50% PS(64 nm) and PBA (97.5 nm) in free air and under periodic airflow, (black line) and (red line) under periodic air flow with τ_p =80s and t_{open}/ t_{close} is (50/50%). Inset: Optical microscopy image depicting the drying front and the stripes patterns left after complete drying. (b) The average speed of the drying front of the advancing and the stopping parts (F_s) estimated from figure 3.11a : open position (□), close position (■) and free air (☆). The blends are dried under periodic air flow at the air speed of 7.86 cm/s at 23^0C and humidity ratio of 34%.

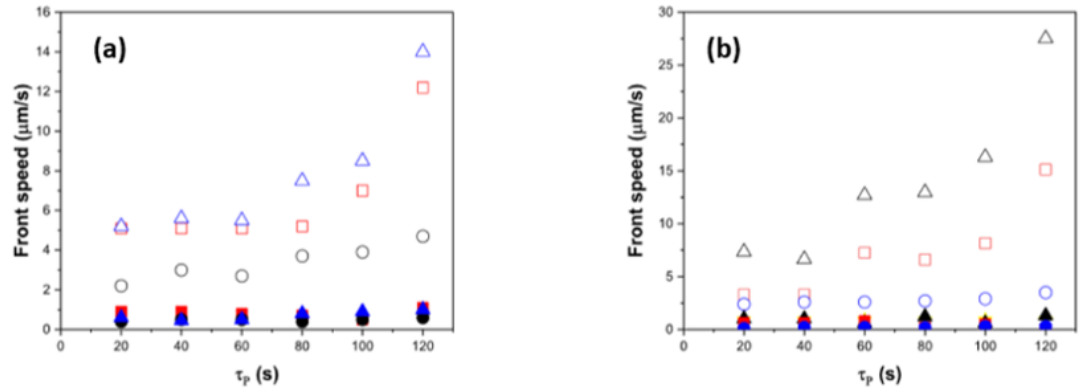

Figure 3.12: (a) The average speed of drying front in different suspensions at flow rate of air 43.85 cm/s. The t_{open}/ t_{close} is (50/50%) at room temperature 23^0C and humidity ratio of 34%. In open position: Mixture (△), PS (□), and PBA (○). While in close position: Mixture (▲), PS (■), and PBA (●). (b) The average drying front speed during drying (PS/PBA) mixture by varying airflow rate. In open position: 43.85 cm/s (△), 24.64 cm/s(□), 7.86 cm/s (○), and free air (★). While in close position: 43.85 cm/s (▲) , 24.64 cm/s (■), *and* 7.86 cm/s(●).

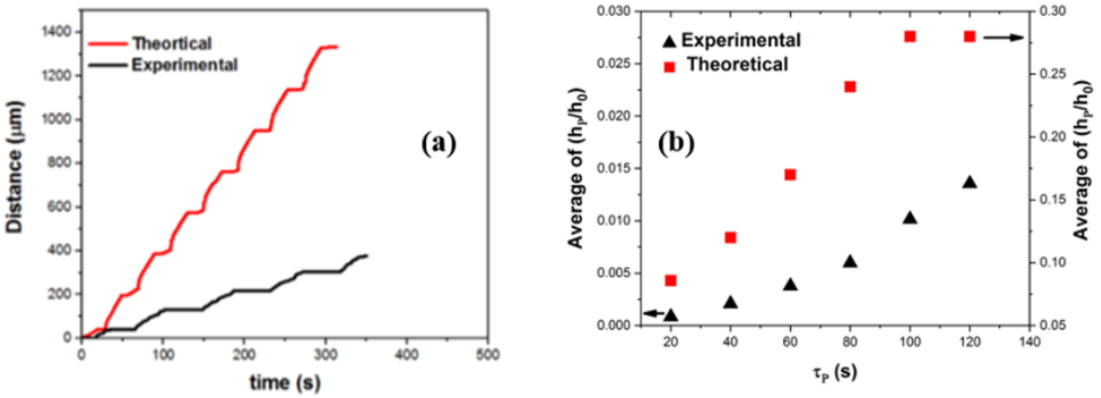

Figure 3.13: (a) black line: position of the dying front from the border during drying a sessile drop of blend made of 50%/50% PS(64 nm) and PBA (97.5 nm) under periodic airflow τ_p =80s and t_{open}/ t_{close} is (50/50%) compared to the calculated one using the model (red line). (b) Average amplitude height h_p divided by the average film height h_0 and plotted vs τ_p for experimental data (▲) and theoretical results(■).

Discussion

The average drying rate reflects the total mass loss of water during evaporation. In the case of no air flow one can assume that the drying to be diffusion limited and therefore the drying rate (E_v) can be written as

$$E_v \sim C_s(r, z)D \tag{3.3}$$

Where $Cs(r, z)$ is the water vapor concentration and D is the water vapor diffusion coefficient in the proximity of the drop surface. This leads to define the drying rate in small drop

$$E_v \sim C_s(r, z)D\frac{1}{\sqrt{(R-r)}} \tag{3.4}$$

Where R is the drop radius and r is the radial position in the drop. On the other hand, when air is blown on the drop, evaporation becomes convective and the average water vapor concentration Cw(r,z, t) on the drop decreases and therefore the drying rate increases as seen in Figure (3.2) and when air is blown periodically on the drop, the average drying rate (E_v) is almost independent of τ_p for similar opening time fraction (ϕ_t^0) but it is only sensitive to ϕ_t^0 for constant τ_p. Keeping the same opening time fraction ϕ_t^0 while varying τ_p should lead to a similar average value of Cw(r,z, t) and therefore a similar value of E_v . The drying front speed (F_s) is found to follow different tendencies compared to drying rate as shown in (Figure 3.12b). While E_v/E_v^0 (E_v^0 is the E_v value in no air flow) remains almost constant with increasing τ_p, the F_s/ F_v^0 (F_v^0 is the F_s value in no air flow case) increases between 7 and 30 times. This can be explained by the fact that the drying rate reflects the total mass loss while the advance of drying front reflects the gradient of concentration in the drop plane. Indeed, the drying front visualized in microscopy is a signature of the transition from a reversible colloidal suspension to a gel-like or irreversible solid. In these suspensions, at low ionic strength the gel/ solid structure occurs at the close packed structure fraction of 0.64.[41] Because the speed of the drying front increases much faster than the average drying rate, one can conclude that, in the presence of periodic air flow, the in-plane concentration gradient becomes more pronounced when air is periodically blown on the suspension. From the first glance, one can explain the periodic surface morphology by alternative deposition of particles at the immobile drying front followed by an advance of this front with a lesser particle deposition. Indeed, the radial drying rate generates a pronounced concentration gradient from the drop front to the center. Once the solid fraction in the proximity of the drying front reaches the close packed fraction 0.64, the suspension freezes at this position and the drying front moves forward to this new position. This is a simplified point of view of what happens in the proximity of the drying front which indeed is more complicated because the dynamic of the liquid/gel/ solid transition depends on the local ionic strength and on the osmotic pressure that tends to equilibrate the concentration of the particles and that of

the ionic entities. The gradient of Cw(r,z,t) during air flow becomes more pronounces due to the directional flow of dry air. In this case, the front dries rapidly enhancing the in-plane concentration gradient and yielding the drying front to move faster toward the center. When air flow stops, Cw(r,z,t) relaxes back to the original state and therefore the drying becomes progressively less heterogeneous in the plane, leading the drying front to stop or to slow down (Figure 3.11b). These results suggest that blowing air periodically enhances the horizontal drying heterogeneities and subsequently enhances the horizontal concentration gradient, which yield the drying front to move faster when air speed is higher. During air flow, the enhanced drying rate gradient creates a capillary flow that induces in-plane particles/solvent flux toward the front. Once air flow stops, the in-plane drying rate gradient is reduced leading to a slower advance of the drying. In the meantime, the liquid flux continues carrying particles to the drying front leading to accumulation of particles in this zone. When air flow starts again, the drying front moves faster toward the center due to the enhanced drying rate gradient while in-plane liquid flux is not enhanced in the same magnitude. This leads to a reduced particles accumulation in the drying front and therefore generates valleys and hills in the dry films. Quantitatively, the formation of hills and valleys in the film can be calculated by estimating the balance between the particles/solvent flux towards the drying front and the advance of this front. The fluid flux is driven by the gradient of capillary pressure that counterbalanced by the suspension viscosity (μ):

$$J_p \sim \frac{1}{\mu}\frac{dP}{dr} \tag{3.5}$$

Where, $P \sim \gamma/\kappa$. The capillary pressure (P), can be directly related to the inverse of the radius of curvature of the drop and the surface tension of air/liquid (γ). The advances of the drying front is related to the magnitude of the horizontal concentration gradient and reflects the movement of the zone where the fluid crosses the close packed structure (0.64). The radial concentration profile was estimated using several assumptions. 1) The vertical concentration gradient was neglected in the first attempt. 2) A calotte was assumed as initial shape of the drop with a contact angle of 19.5°.3) The solid concentration profile $\phi_p(r,t)$ and the height of the profile z(r,t) were estimated at different times (t) and radial position (r) using mass conservation laws.
For solid

$$\frac{d}{dt}(\phi h) = (\phi J_{p(in)}) - (\phi J_{p(out)}) = \frac{d}{dr}(\phi J_p) = \frac{d}{dr}\left(\frac{\phi}{\mu}\frac{d(\gamma/\kappa)}{dr}\right) \tag{3.6}$$

For liquid

$$\frac{d}{dt}(1-\phi)h = \frac{d}{dr}(1-\phi)J_p - E_v(t) = \frac{d}{dr}\left(\frac{(1-\phi)}{\mu}\frac{d(\gamma/\kappa)}{dr}\right) - E_v(t) \tag{3.7}$$

Where ϕ is concentration profile and E_v the evaporation rate. These equations can be resolved numerically if one knows how the local viscosity ($\eta(\phi_p, t)$) dependence on the particle concentration and time as well as the details of liquid flux in the solid zone at the drying front. If one considers a no slip condition at the solid surface, the vertical profile of the flux can be estimated to vary as z^2 and therefore the average vertical flux can be estimated. For the learning purposes, one can assume two extreme cases: 1) under air flow, the lateral capillary flux is neglected compared to the vertical evaporation and the advance of the drying front occurs when volume fraction crosses 0.64. 2) During no air flow, the lateral capillary flux is assumed to dominates. This is achieved by assuming a negligible viscosity in the liquid zone and infinite at the solid/gel transition. The drying front advance is reduced by the lateral capillary flow of the diluted suspension. Using these two simple assumptions one can predicts the periodic advance and stopping during periodic air flow (Figure 3.13). At the end of the drying the predicted height profile of the 3D perioding structure is also predicted with this simple model to a great extent and particularly reproduce the dependence of the height profile on τ_p. However, the details of this prediction in terms of the absolute values of the drying front speed and the height profile requires more details about the evolution of the drying rate gradient, the viscosity dependence on the concentration and time and role of the osmotic pressure.

Conclusion

The present work aims to understand the mechanism of making periodic surface arrays by design using a rapid and user-friendly mechanism which involves a simple time modulation of the drying rate. First the role of evaporation rate on the drying front was investigated in several colloidal suspensions, with finely controlled ionic strength such as polystyrene, polybutylacrylates and their blends. The possibility of tuning the moving and arrest of the drying front, on demand, was investigated using time modulated drying rate. This was found to yield a fine control of the moving and arrest of the drying front and consequently the magnitude of particle deposition in each regime. Through time modulation of the drying rate, 3D periodic surface arrays with controlled period and amplitude were constructed. Finally, the dynamic of the observed drying front and the resulting surface structures were predicted using a simple drying model.

Table of content

Periodic surface-morphologies through temporal modulating the drying rate during evaporation of colloidal suspensions

Essa shawail[a], *Yahya Rharbi*[a,b]
(a) Univ.Grenoble Alpes - LRP, F-38041 Grenoble, FRANCE
(b) CNRS, LRP , F-38041 Grenoble, FRANCE
Corresponding Author Email: yahya.rharbi@univ-grenoble-alpes.fr

Abstract

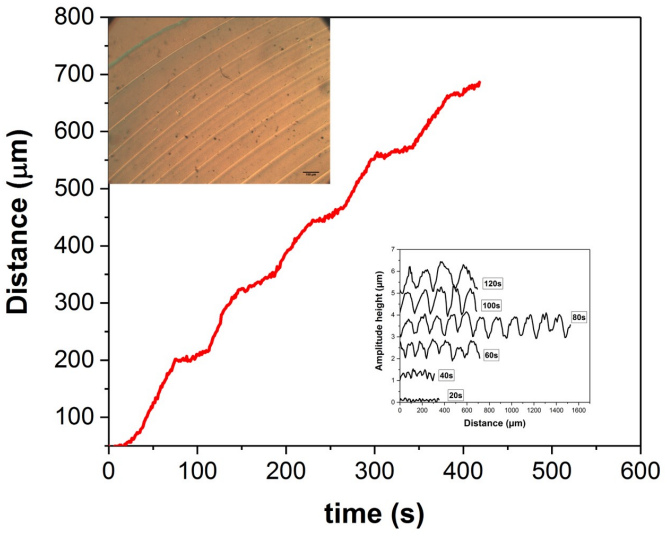

Figure 3.14

Supporting Information

Periodic surface-morphologies through temporal modulating the drying rate during evaporation of colloidal suspensions

Essa shawail[a], *Yahya Rharbi*[a,b]
(a) Univ.Grenoble Alpes - LRP, F-38041 Grenoble, FRANCE
(b) CNRS, LRP , F-38041 Grenoble, FRANCE
Corresponding Author Email: yahya.rharbi@univ-grenoble-alpes.fr

Content

Figures S3.1-S3.9

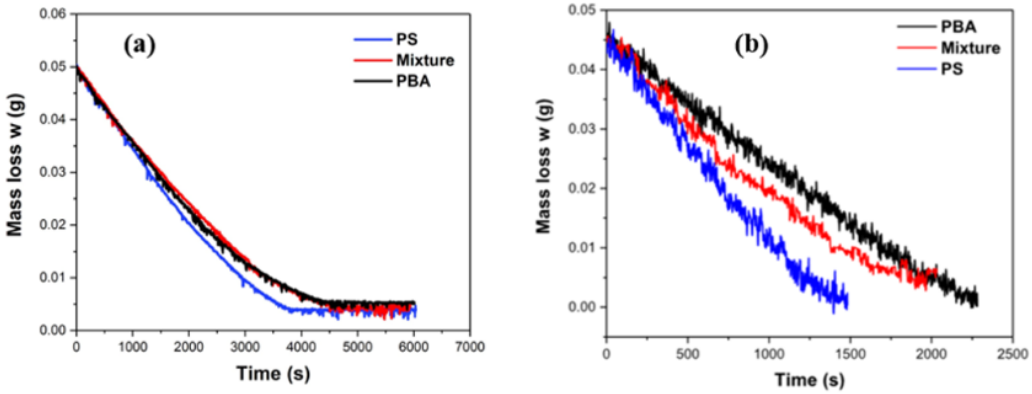

Figure S3.1: (Drop weight loss (w) as a function of the drying time in PS(64 nm) (blue) , PBA (97.5 nm) (black) and their mixture 50% 50% (red) in free (a) and under continuous air flow at the flow rate 7.86 cm/s (b). Drying takes place at 23^0C and humidity ratio of 34%.

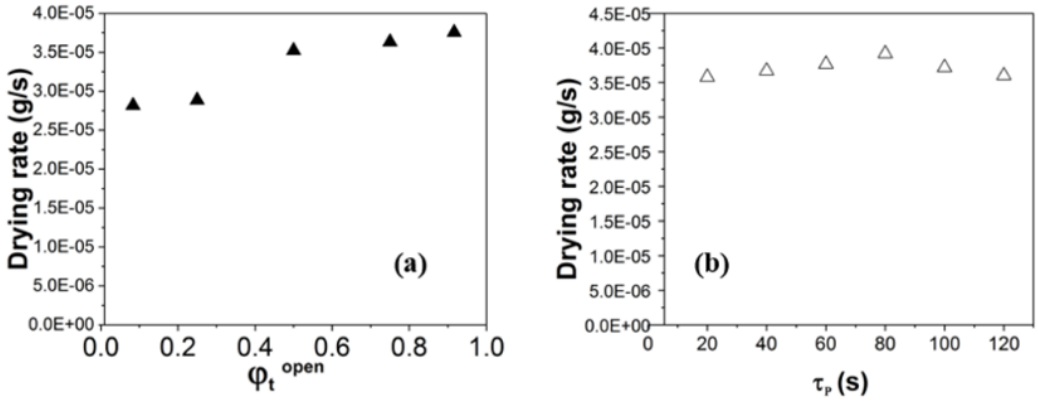

Figure S3.2: Drying rate calculated from the drop weight loss as a function of the drying time in a mixture 50% 50% PS(64 nm) /PBA(97.5 nm) under periodic airflow at the flow rate 7.86 cm/s. (a) The drying rate is plotted vs. ϕ_t^{open} for $\tau_p = 120$s. b) The drying rate plotted vs. τ_p for constant ϕ_t^{open} (50%).

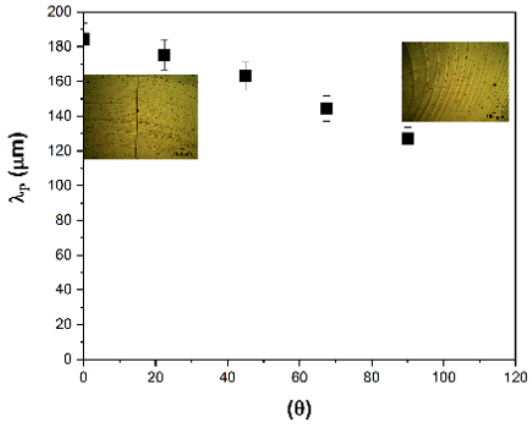

Figure S3.3: Period of the periodic patterns (λ_p) measured at different areas of the dried drop plotted vs. the orientation angle (θ). θ is calculated starting from the direction of the air flow. inset: microscopy images at two positions : (left) air flow direction and (right) perpendicular to the airflow direction.

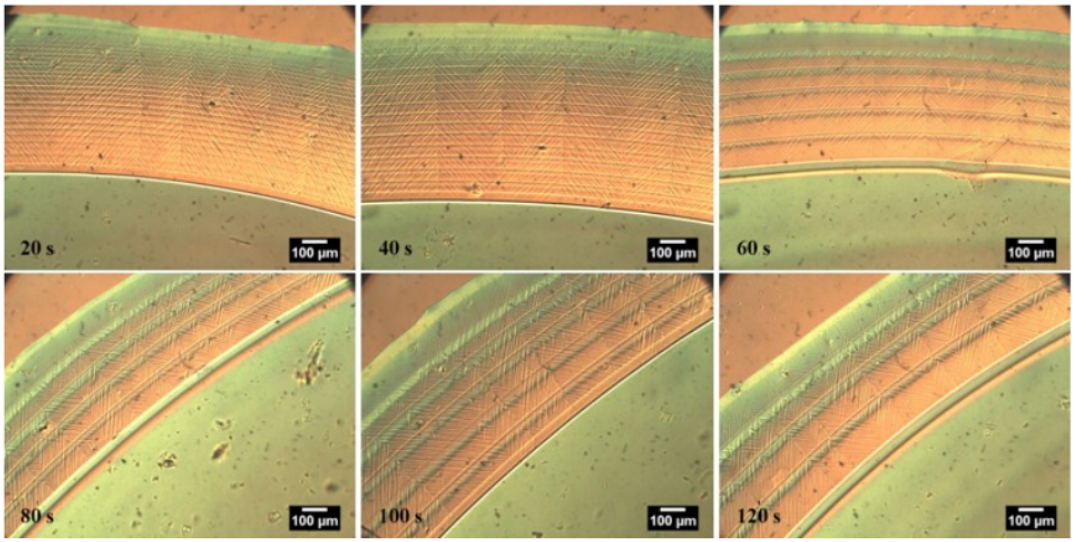

Figure S3.4: Optical microscopy images of stripes pattern of films made by drying sessile drops PS (64nm) under periodic airflow. The periodic airflow is controlled by a fan with arduino controlled shutter. The t_{open}/ t_{close} was fixed to 50/50% and the time period τ_p was set to 20 s, 40s, 60s, 80s, 100s and 120s. The drying was carried out on glass substrate at room temperature 23^0C and humidity ratio of 34% and airflow rate was 7.86 cm/s. The blend concentration was 10 wt%.

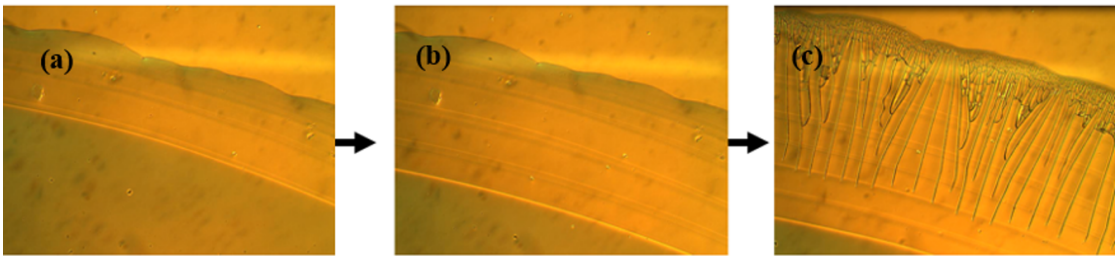

Figure S3.5: Optical microscopy images depicting the different stages of drying a sessile drop of PS (64 nm) under periodic airflow. a) beginning of the drying, b) periodic patterns formation and c) periodic pattern with cracks. The drying takes place at 23^0C and humidity ratio of 34% under air flow speed of 7.86 cm/s and ϕ_t^0 =50%).

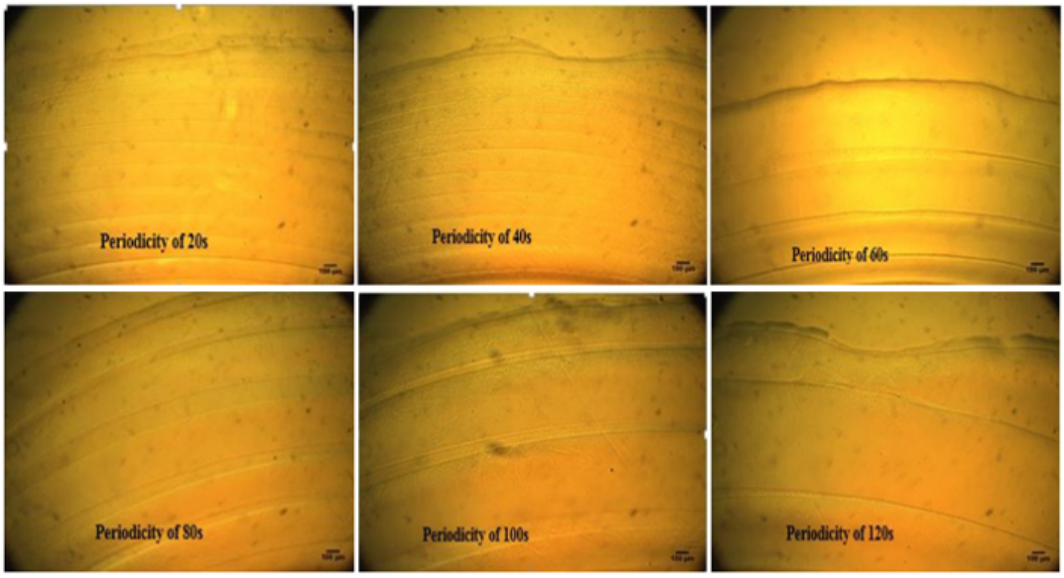

Figure S3.6: Optical microscopy images showing the stripes pattern of films made by drying sessile drops PBA (97.5nm) under periodic airflow. The periodic airflow is controlled by a fan with arduino controlled shutter. The $t_{open}/\ t_{close}$ was fixed to 50/50% and the time period τ_p was set to 20 s, 40s, 60s, 80s, 100s and 120s. The drying was carried out on glass substrate at room temperature 23^0C and humidity ratio of 34% and airflow rate was 7.86 cm/s. The blend concentration was 10 wt%.

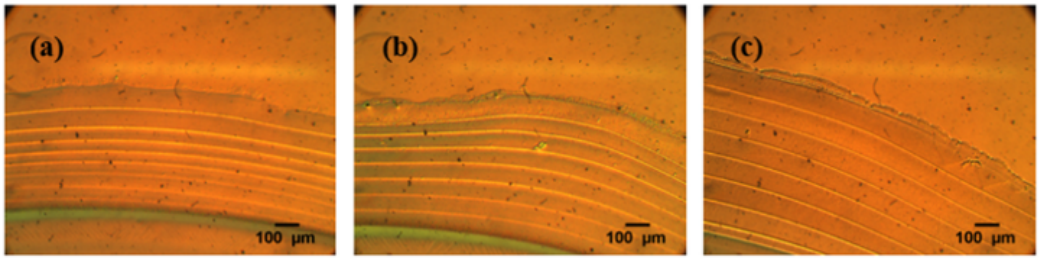

Figure S3.7: Optical microscopy images depicting the stripe patterns resulting from drying under periodic airflow several mixtures of PS(64 nm) and PBA(97.5 nm) at different compositions PS/PBA: (a) 70%/30% , (b) 50%/50% and (c) 30%/70%. The ϕ_t^0: (50/50%), room temperature 23^0C and humidity ratio of 34%.

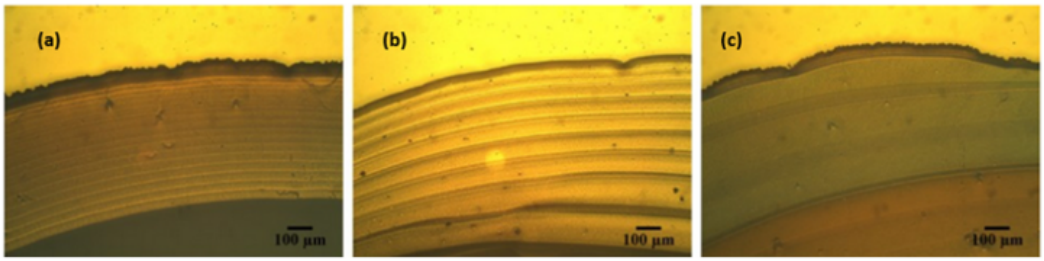

Figure S3.8: Optical microscopy images depicting the stripe patterns resulting from drying under periodic airflow several mixtures of PS(281 nm) and PBA(97.5 nm) at different compositions PS/PBA: (a) 20%/80%, (b) 50%/50% and (c) 80%/20%. The ϕ_t^0: (50/50%), room temperature 23^0C and humidity ratio of 34%.

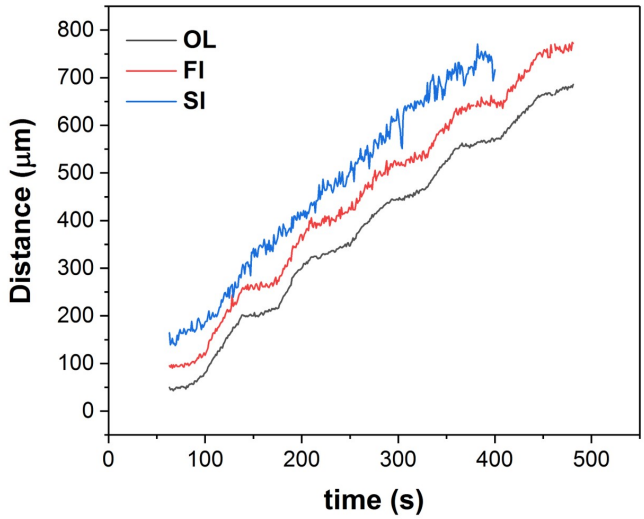

Figure S3.9: The drying front motion of (OL, FL and SL) during drying a mixture 50%/50% PS(64 nm)/PBA(97.5 nm) under periodic airflow at the flow rate 7.86 cm/s. The $\tau_p = 80s$ with a constant ϕ_t^0 of (50/50%) at room temperature 23^0C and humidity ratio of 34%.

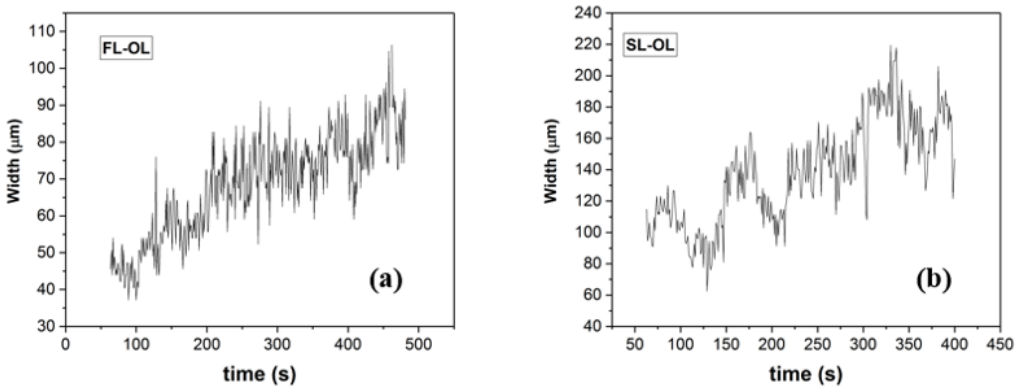

Figure S3.10: The time evolution of the width of drying front during drying a mixture of PS(64 nm)/PBA(97.5 nm) 50%/50% under periodic airflow at the flow rate 7.86 cm/s. (a) The total width of first zone (FL-OL) and (b) the width for the second zone (SL-OL). The ϕ_t^0 of (50/50%) at room temperature 23^0C and humidity ratio of 34%.

Bibliography

[1] Kapil Debnath, Thalia Dominguez Bucio, Abdelrahman Al-Attili, Ali Z Khokhar, Shinichi Saito, and Frederic Y Gardes. Photonic crystal waveguides on silicon rich nitride platform. *Optics express*, 25(4):3214–3221, 2017.

[2] Cathleen M Crudden, J Hugh Horton, Mina R Narouz, Zhijun Li, Christene A Smith, Kim Munro, Christopher J Baddeley, Christian R Larrea, Benedict Drevniok, Bheeshmon Thanabalasingam, et al. Simple direct formation of self-assembled n-heterocyclic carbene monolayers on gold and their application in biosensing. *Nature communications*, 7(1):1–7, 2016.

[3] Wen-Tao Cao, Wei Feng, Ying-Ying Jiang, Chang Ma, Zi-Fei Zhou, Ming-Guo Ma, Yu Chen, and Feng Chen. Two-dimensional mxene-reinforced robust surface superhydrophobicity with self-cleaning and photothermal-actuating binary effects. *Materials Horizons*, 6(5):1057–1065, 2019.

[4] LK Teh, NK Tan, CC Wong, and S Li. Growth imperfections in three-dimensional colloidal self-assembly. *Applied Physics A*, 81(7):1399–1404, 2005.

[5] Cédric Boissière, David Grosso, and Eric Prouzet. Inorganic nanomaterials synthesis using liquid crystals. *Encyclopedia of Inorganic Chemistry*, 2006.

[6] Chongfeng Zhang and Pinar Akcora. Evaporation controlled particle patterns in a polymer droplet. *RSC advances*, 7(30):18321–18326, 2017.

[7] Robert Malinowski, Giovanni Volpe, Ivan P Parkin, and Giorgio Volpe. Dynamic control of particle deposition in evaporating droplets by an external point source of vapor. *The journal of physical chemistry letters*, 9(3):659–664, 2018.

[8] Yuanyi Zhang, Colton A D'Ambra, Reika Katsumata, Ryan L Burns, Mark H Somervell, Rachel A Segalman, Craig J Hawker, and Christopher M Bates. Rapid and selective deposition of patterned thin films on heterogeneous substrates via spin coating. *ACS applied materials & interfaces*, 11(23):21177–21183, 2019.

[9] Lauryanne Teulon, Yannick Hallez, Simon Raffy, Francois Guerin, Etienne Palleau, and Laurence Ressier. Electrostatic directed assembly of colloidal microparticles assisted by convective flow. *The Journal of Physical Chemistry C*, 123(1):783–790, 2018.

[10] Xue Li and James F Gilchrist. Large-area nanoparticle films by continuous automated langmuir–blodgett assembly and deposition. *Langmuir*, 32(5):1220–1226, 2016.

[11] Evangelia Antonopoulou, Connor F Rohmann-Shaw, Thomas C Sykes, Olivier J Cayre, Timothy N Hunter, and Peter K Jimack. Numerical and experimental analysis of the sedimentation of spherical colloidal suspensions under centrifugal force. *Physics of Fluids*, 30(3):030702, 2018.

[12] RC Hayward, DA Saville, and Ilhan A Aksay. Electrophoretic assembly of colloidal crystals with optically tunable micropatterns. *Nature*, 404(6773):56–59, 2000.

[13] Daniel J Harris, Hua Hu, Jacinta C Conrad, and Jennifer A Lewis. Patterning colloidal films via evaporative lithography. *Physical review letters*, 98(14):148301, 2007.

[14] Mayuresh Kulkarni, Subhadarshinee Sahoo, Pankaj Doshi, and Ashish V Orpe. Fingering instability of a suspension film spreading on a spinning disk. *Physics of Fluids*, 28(6):063303, 2016.

[15] Chih-Ting Liu, Chia-Chan Tsai, Chien-Wei Chu, Mu-Huan Chi, Pei-Yun Chung, and Jiun-Tai Chen. Dewetting of polymer thin films on modified curved surfaces: preparation of polymer nanoparticles with asymmetric shapes by anodic aluminum oxide templates. *Soft matter*, 14(15):2772–2776, 2018.

[16] Laurent Malaquin, Tobias Kraus, Heinz Schmid, Emmanuel Delamarche, and Heiko Wolf. Controlled particle placement through convective and capillary assembly. *Langmuir*, 23(23):11513–11521, 2007.

[17] Yasushi Mino, Satoshi Watanabe, and Minoru T Miyahara. Fabrication of colloidal grid network by two-step convective self-assembly. *Langmuir*, 27(9):5290–5295, 2011.

[18] Satoshi Watanabe, Koji Inukai, Shunsuke Mizuta, and Minoru T Miyahara. Mechanism for stripe pattern formation on hydrophilic surfaces by using convective self-assembly. *Langmuir*, 25(13):7287–7295, 2009.

[19] Ryuichi Sakamoto, Yoshiki Hataguchi, Ryosuke Kimura, Katsumi Tsuchiya, and Yasushige Mori. Stripe and network formation of particle arrays fabricated by convective self-assembly. *Chemistry Letters*, 41(10):1207–1209, 2012.

[20] Robert D Deegan, Olgica Bakajin, Todd F Dupont, Greb Huber, Sidney R Nagel, and Thomas A Witten. Capillary flow as the cause of ring stains from dried liquid drops. *Nature*, 389(6653):827–829, 1997.

[21] Robert D Deegan, Olgica Bakajin, Todd F Dupont, Greg Huber, Sidney R Nagel, and Thomas A Witten. Contact line deposits in an evaporating drop. *Physical review E*, 62(1):756, 2000.

[22] E Rio, A Daerr, François Lequeux, and Laurent Limat. Moving contact lines of a colloidal suspension in the presence of drying. *Langmuir*, 22(7):3186–3191, 2006.

[23] H Bodiguel, F Doumenc, and B Guerrier. Pattern formation during the drying of a colloidal suspension. *The European Physical Journal Special Topics*, 166(1):29–32, 2009.

[24] Khellil Sefiane. Patterns from drying drops. *Advances in colloid and interface science*, 206:372–381, 2014.

[25] Maryam Parsa, Souad Harmand, and Khellil Sefiane. Mechanisms of pattern formation from dried sessile drops. *Advances in colloid and interface science*, 254:22–47, 2018.

[26] Mengmeng Wu, Xingkun Man, and Masao Doi. Multi-ring deposition pattern of drying droplets. *Langmuir*, 34(32):9572–9578, 2018.

[27] Yasushi Mino, Satoshi Watanabe, and Minoru T Miyahara. Colloidal stripe pattern with controlled periodicity by convective self-assembly with liquid-level manipulation. *ACS applied materials & interfaces*, 4(6):3184–3190, 2012.

[28] Hongta Yang and Peng Jiang. Large-scale colloidal self-assembly by doctor blade coating. *Langmuir*, 26(16):13173–13182, 2010.

[29] Maël Le Berre, Yong Chen, and Damien Baigl. From convective assembly to landau- levich deposition of multilayered phospholipid films of controlled thickness. *Langmuir*, 25(5):2554–2557, 2009.

[30] Charles Loussert, Frédéric Doumenc, Jean-Baptiste Salmon, Vadim S Nikolayev, and Béatrice Guerrier. Role of vapor mass transfer in flow coating of colloidal dispersions in the evaporative regime. *Langmuir*, 33(49):14078–14086, 2017.

[31] Mohamed Asbahi, FuKe Wang, Zhaogang Dong, Joel KW Yang, and Karen SL Chong. Directed self-assembly of sub-10 nm particle clusters using topographical templates. *Nanotechnology*, 27(42):424001, 2016.

[32] Hugues Bodiguel, Frédéric Doumenc, and Béatrice Guerrier. Stick- slip patterning at low capillary numbers for an evaporating colloidal suspension. *Langmuir*, 26(13):10758–10763, 2010.

[33] Rajneesh Bhardwaj, Xiaohua Fang, Ponisseril Somasundaran, and Daniel Attinger. Self-assembly of colloidal particles from evaporating droplets: role of dlvo interactions and proposition of a phase diagram. *Langmuir*, 26(11):7833–7842, 2010.

[34] Hua Hu and Ronald G Larson. Marangoni effect reverses coffee-ring depositions. *The Journal of Physical Chemistry B*, 110(14):7090–7094, 2006.

[35] Emma L Talbot, Lisong Yang, Arganthael Berson, and Colin D Bain. Control of the particle distribution in inkjet printing through an evaporation-driven sol–gel transition. *ACS applied materials & interfaces*, 6(12):9572–9583, 2014.

[36] Yongjoon Choi, Jeongin Han, and Chongyoup Kim. Pattern formation in drying of particle-laden sessile drops of polymer solutions on solid substrates. *Korean Journal of Chemical Engineering*, 28(11):2130–2136, 2011.

[37] David Brutin. Influence of relative humidity and nano-particle concentration on pattern formation and evaporation rate of pinned drying drops of nanofluids. *Colloids and Surfaces A: Physicochemical and Engineering Aspects*, 429:112–120, 2013.

[38] Susanna Baesch, Kyle Price, Philip Scharfer, Lorraine Francis, and Wilhelm Schabel. Influence of the drying conditions on the particle distribution in particle filled polymer films: Experimental validation of predictive drying regime maps. *Chemical Engineering and Processing-Process Intensification*, 123:138–147, 2018.

[39] Ashish Pathak and Mehdi Raessi. Steady-state and transient solutions to drop evaporation in a finite domain: Alternative benchmarks to the d2 law. *International Journal of Heat and Mass Transfer*, 127:1147–1158, 2018.

[40] Tibor Poós and Evelin Varju. Mass transfer coefficient for water evaporation by theoretical and empirical correlations. *International Journal of Heat and Mass Transfer*, 153:119500, 2020.

[41] Alexander F Routh and William B Russel. Horizontal drying fronts during solvent evaporation from latex films. *AIChE Journal*, 44(9):2088–2098, 1998.

[42] Bin Yang, James S Sharp, and Michael I Smith. Shear banding in drying films of colloidal nanoparticles. *Acs Nano*, 9(4):4077–4084, 2015.

[43] Ludovic Pauchard, Berengere Abou, and Ken Sekimoto. Influence of mechanical properties of nanoparticles on macrocrack formation. *Langmuir*, 25(12):6672–6677, 2009.

[44] Wai Peng Lee and Alexander F Routh. Why do drying films crack? *Langmuir*, 20(23):9885–9888, 2004.

[45] Tak-Sing Wong, Ting-Hsuan Chen, Xiaoying Shen, and Chih-Ming Ho. Nanochromatography driven by the coffee ring effect. *Analytical chemistry*, 83(6):1871–1873, 2011.

[46] Robert D Deegan. Pattern formation in drying drops. *Physical review E*, 61(1):475, 2000.

[47] Lucas Goehring, William J Clegg, and Alexander F Routh. Solidification and ordering during directional drying of a colloidal dispersion. *Langmuir*, 26(12):9269–9275, 2010.

Chapter 4

Control of surface morphology during evaporation of colloidal suspension containing ionic surfactant under periodic airflow

Contents

4.1 Introduction

This chapter is presented also in the form of a scientific publication. In this fourth chapter, the roles of surfactant on the dynamic of the drying front and the resulting 3D surface morphology was investigated. We show that adding aliquots of sodium dodecyl sulfate (SDS) affects the drying front dynamic under a modulated drying rate as well as the resulting surface morphology. The patterns period was found to decrease with increasing [SDS] and exhibit the same tendency as the surface tension. Furthermore, the onset and the first line of drying front was found to advance with a velocity, which decrease with increasing [SDS]. On the other, the second line of the drying front was found to advance rapidly during airflow and recedes back to the onset line once the airflow stops. These dynamics were found to follow a similar tendency of the surface tension which suggests that the surface tension plays a significant role in this process. In this chapter also, we explore the role of salt (potassium chloride, KCl) on the formation of the periodic patterns. In particular, we want to understand how the screening of electrostatic repulsions between particles affects the particle deposition under the periodic airflow.

4.2 Control of surface morphology during evaporation of colloidal suspension containing ionic surfactant under periodic airflow

Essa shawail[a], *Yahya Rharbi*[a,b]
(a) Univ.Grenoble Alpes - LRP, F-38041 Grenoble, FRANCE
(b) CNRS, LRP , F-38041 Grenoble, FRANCE
Corresponding Author Email: yahya.rharbi@univ-grenoble-alpes.fr

Keywords: Colloidal suspension, drying front, surface patterning, evaporation, triple line, Surfactant, ionic strength.

Abstract

Surface patterning via convective-assembly takes advantage of targeted deposition of the particles at the drying front during drying colloidal suspensions. This can be achieved by precise control of the dynamic of the drying front and the mechanism of particle deposition in this region. In our previous work, we have shown that the surface patterning can be obtained via a periodic displacement of the drying front by modulating the drying speed over time. This has been found to allow precise control of the displacement and stopping of the drying front and hence the extent of particle deposition in each regime. Through the temporal modulation of the drying rate, periodic 3D surface patterns with controlled period and amplitude were constructed. This work investigates the roles of sodium dodecyl sulfate surfactant (SDS) on surface patterns. We show that adding aliquots of SDS affects both the dynamics of the drying front as well as the resulting surface morphology. It was found that the pattern period decreases with increasing [SDS] and exhibits the same tendency as the surface tension. Furthermore, the onset and the first line of the drying front was found to advance at a velocity that decreases with increasing [SDS]. As for the second line of the drying front, it was found to advance rapidly during airflow and recedes back towards the onset line once the airflow stops. These dynamics were found to follow a similar tendency of the surface tension which suggests that the surface tension plays a significant role in this process. Furthermore, we explore the role of salt (potassium chloride, KCl) on the formation of the periodic patterns. In particular, we want to understand how the screening of electrostatic repulsions between particles affects the particle deposition under the periodic airflow.

Introduction

Surface patterning during drying of droplet has become a pivotal part of modern science and technology. [1–6] Such process remains active areas of research in diverse industrial applications such as inkjet printing,[7–9] coating,[10] electronics application,[11] material science[12, 13] and bio-medical application.[14]. One way to make such a structured surface of films by using colloidal particles. The colloidal particles can be functionalized at the nanometric level, this can be used as an individual brick to make the multi-structured system. Various methods have been proposed in this field to organise the position of the colloidal particle on a substrate. For example, lithography,[15] electrostatic deposition,[16] spin-coating,[17] Langmuir-Blodgett,[18] fingering instabilities,[19] spontaneous dewetting[20]. Among these methods, the convective deposition technique appears as a simple method for assembling colloidal particles at the drying front.[21–23]. The nature of this process is basically based on the drying at the triple line. Indeed, such process has attracted intensive attention since Deegan and his group published their famous work on the coffee ring.[24, 25] They have shown that the particles are driven towards the pinned triple line imposed by capillary flow and thus deposited at the droplet edge leading to coffee ring effect.

The physical phenomena of the triple line dynamic is involved in this process. This phenomena plays a crucial role on the surface structure, therefore, for most patterns methods, the pattern deposition is controlled via the triple line movement as the drop evaporates .[25–30] However, such process remains difficult task as the system consists of three components (particle, substrate, and liquid) and still not understood adequately yet. Therefore, efforts have been ameliorated to control the dynamics of triple line during evaporation in order to achieve a unique pattern.[31–33] When drying concentrated solutions of sessile drops, the triple line becomes the drying front and it is the interface between suspension/air/dried film. Two drying fronts have been observed during drying colloidal suspension, a front near the edge followed by a second front.[34] The former is reversible, while the second front represents an irreversible change in the nature of the dispersion.

The surface pattern can be more ordered if the triple line dynamic is precisely controlled. One way to achieve that by using dip coating technique, for example, by immersing a substrate vertically into solvent and withdrawal it with a controlled velocity. In both Landau-Levich and capillary regimes,[35] uniform films with modulated thickness can be achieved by controlling evaporation rate, triple line speed, the suspension and substrate properties. The contact line undergoes a stick-slip mechanism at certain conditions within the capillary regime of the dip coating leading to ordered structure.[36] This results from the synergy between capillary flow which brings the fluid towards the triple line and the capillary forces which controls the line retraction. The periodic structure surface of colloids suspension can be achieved by periodic movement of the triple line via mechanically moving the substrate, doctor blade or the suspension. In such a pro-

cess, the triple line is located at the desired position governed by particle deposition at the front imposed by convective flow.[21] Topographical templates have been introduced as a potential method to deposit the particles into the desired locations where the capillary flows close to drying front plays a crucial role in this process.[37] In our previous work we have shown that the surface patterning can be achieved via periodic moving of the drying front by time modulating the drying rate. We showed that the moving and the arrest of the drying front can be tuned via the control of the evaporation rate in certain colloidal suspensions with finely controlled ionic strength and we demonstrate that this can be used to govern particles deposition on demand. This was found to yield a fine control of the moving and arrest of the drying front and consequently the magnitude of particle deposition in each regime. Through time modulation of the drying rate, 3D periodic surface arrays with controlled period and amplitude were constructed. However, the physical chemistry of the suspension can control this structure because the dynamic of the triple line is highly sensitive to the property of the suspension.[34]
Indeed, adding surfactant leads to change in various aspects during the evaporation process such as spreading of colloidal suspension on the substrate, the contact angle, pinning of the drying front, and modifies the drying process.[38–43] The presence of surfactant in the suspension was found to enhance the drying process yielding different scenarios.[44, 45] Early study have shown that even a small amount of surfactant can influence the deposition phenomena during a drying drop of polymer and exhibiting uniform deposition.[46] The surfactant can generate a surface tension gradient along the droplet interface, consequently, affecting the deposition mechanism at the drying front.[47] Indeed, Marangoni flow imposed by surfactant concentration gradients alters the particles assembly resulting in different deposition patterns.[48–51] This eddy drives the particles either towards the drying front or the center. However, Marangoni flow can eliminate the outward flow and produce inward flow towards the center leading to reverse coffee-stain.[52, 53] Furthermore, the high surfactant concentration in the dispersion can lead to adsorb surfactant in both substrate and particles, hence, affecting the final surface morphology. This effect becomes much greater in the presence of the Marangoni flow.[51] The effect of surfactant on the dynamics of the triple line has been investigated in order to understand the physics deposition phenomena.[54] The combination between particles and surfactant concentration was found to enhance the onset of the dynamic contact angle hysteresis on surfaces and yield a decrease in its value.[55, 56] Lately, the effect of surfactant on the deposition pattern during evaporation has been extended in order to generate a new strategy for controlling the assembly deposition.[57] A recent study investigated the impact of sodium dodecyl sulfate or SDS on the deposition pattern during drying by using the convective assembly technique. The study showed that the presence of SDS in suspensions has a vital role on the resulted surface morphology.[58] This work investigates the roles of surfactant on the dynamic of drying front and the resulting 3D surface morphology during drying colloidal suspension under periodic air-

flow. We show that adding aliquots of sodium dodecyl sulfate (SDS) affects the drying front dynamic under a modulated drying rate as well as the resulting surface morphology. The patterns period was found to decrease with increasing [SDS] and exhibit the same tendency as the surface tension. Furthermore, the onset of drying front was found to advance with a velocity, which decrease with increasing [SDS]. On the other hand, the endset of the drying front was found to advance rapidly during airflow and recedes back to the onset line once the airflow stops. These dynamics were found to follow a similar tendency of the surface tension which suggests that the surface tension plays a significant role in this process.

Experimental

Materials

The material used during the preparation of the particles are the monomers (styrene, Aldrich, 99%), (BA, 99% Aldrich) and distilled water. Both of the surfactant sodium dodecyl sulfate (SDS, Aldrich, 99%) and the initiator potassium persulfate (KPS, Aldrich, 98%) were used as received.

Preparation of the polymer suspensions

Polystyrene and butyl polyacrylate suspensions were prepared in batch emulsion polymerization from styrene, butyl acrylate, SDS surfactant, and the potassium persulfate initiator. Monomers, surfactant, and water were mixed in a standard three-neck round flask (500 mL) with a condenser under nitrogen flow and heated to 74^0 C after that the initiator was added when the mixture reached the desired temperature. The particle size was controlled by varying the amount of SDS. To clean the synthesized latex, a mixture of anionic and cationic exchange resins (DOWEX Marathon MR3, Aldrich) was used. The suspensions were mixed with 5 wt. % resin, agitated gently for several minutes, and then filtered to remove the resin. During cleaning, the conductivity decreased, and it was monitored after each step of cleaning. This procedure was repeated for several times until a constant conductivity value was obtained. In this part, the roles of surfactant on the dynamic of the drying front and the resulting 3D surface morphology was investigated. The concentration of [SDS] in the suspension is varied from 0 to 31 mmol/L.

Polymer and Particle Characterization

The measurement of particle diameters (D) has been carried out by dynamic light scattering (DLS). This measurement was conducted on a Zetasizer (Malvern 5000) device with an angle of 90^0 by using a HeNe laser. Differential Scanning Calorimetry (DSC) mesurements were carried out on a Mettler-Toledo DSC823 device with heating and cooling speeds 10^0 C / min, in a temperature range from -50^0 C up to 140^0 C. The T_g of PS is 100^0 C while for PBA T_g is -49^0 C.

Surface tension and contact angle measurements

The Digidrop GBX apparatus is used to measure the surface tension of the suspension by the pendant drop method. The procedure is based on capturing the images of liquid drop which hangs from dosing needle during its growth until its detachment. The software automatically calculates the surface tension. Several measurements were taken in each experiment, however, the performing calculation is made just for the last ten images.

This process was repeated several times at the ambient conditions. The surface tension was measured for both the mixture PS/PBA and water in the presence of different concentration of SDS (Figure 4.5).
The Digidrop GBX optics apparatus was also used to measure the contact angle of the drop between the liquid surface and the solid substrate. The principle of this method is based on the analysis of a video images coming from a CCD sensor. The software can then analyze the digitized image of the drop and determines its geometric characteristics. This software offers a measurement method that calculates the values of the left angle, the right angle and their average value. The measurement of the contact angle on the solid substrate for (PS / PBA) mixture with different [SDS] are shown in (Supporting Formation Figure S4.1). The contact angle decreases with increasing [SDS] from 23^0 in the absence of SDS to around 3.5^0 above CMC.

Drying system

The drying system is a home built device equipped with a small flat fan (Figure 4.1a). The fan speed is controlled using PMW signal and monitored using tachometer leading to constant speed from 565 rpm to 4200 rpm. This yields an air flow of $2x10^{-4}$ to $1.6x10^{-3}$ m^3/s. Taking into consideration the opening of the fan (0.7 x 3.2 cm) , the velocity of the air were set 7.86, 24.6, 35.5, 43.9 and 48.72 cm/s. In all the experiments the air flow was limited in order for the sessile drop to remain stable and this set an upper limit of air flow of 43.85 cm/s. The periodic air flow is periodically tuned by opening and closing a shutter on the fan gate using an arduino controlled servo for different time intervals t_{open} and t_{close} which was varied between 10s and 60s. The period of airflow is calculated as $\tau_p = t_{open} + t_{close}$ leading to a period between 20 s and 120s. The fraction of opening time is estimated as $\phi_t^{open} = t_{open}/(t_{open} + t_{close})$ leading to ϕ_t^{open} between 10% to 90%. The drying system was either placed on Mettler balance to measure the drying rate during periodic air flow or on a microscope to observe the evolution of the structure throughout the drying. In all cases, the distance between the drop and the fan opening was set to $\sim$ 6 cm. The substrate, glass microscope slides (1x 76 x 26 mm), which were previously cleaned using alcohol and distilled water and left to dry. The glass slide is first placed on the drying system and then a $\sim$ 0.05 ml of the latex suspension were deposited using the glass slide leading to a circular drop of around $\sim$ $1cm$. The drying environment was kept at 23^0C and humidity ratio of 34%. The mass loss during drying was measured using a Mettler balance with precision 0.01 mg connected to a computed with home-built software. When periodic drying the mass loss was monitored during gate closure periods. Several suspensions were used for the drying process PBA (97.5 nm) and PS (64 nm) as well as their blends. The initial concentration of the suspensions is 10 wt.%. The blends were prepared by mixing the cleaned PBA and one of the two PS suspensions at different fractions between PS/PBA between 50% and 50%. The following experiments

are carried out with blends PS/PBA of 50%/50%.
SDS solution of 50 g/l was prepared and aliquots of this solution is added to the cleaned PS/PBA suspension in order to obtain the desired SDS molar concentration in the blends between 0 to 31 mmol/l. KCl solution of 50 g/l was prepared and small amount of this solution is added under agitation to the cleaned blend suspension to reach the desired KCl concentration between 0 and 10 mmol/l.

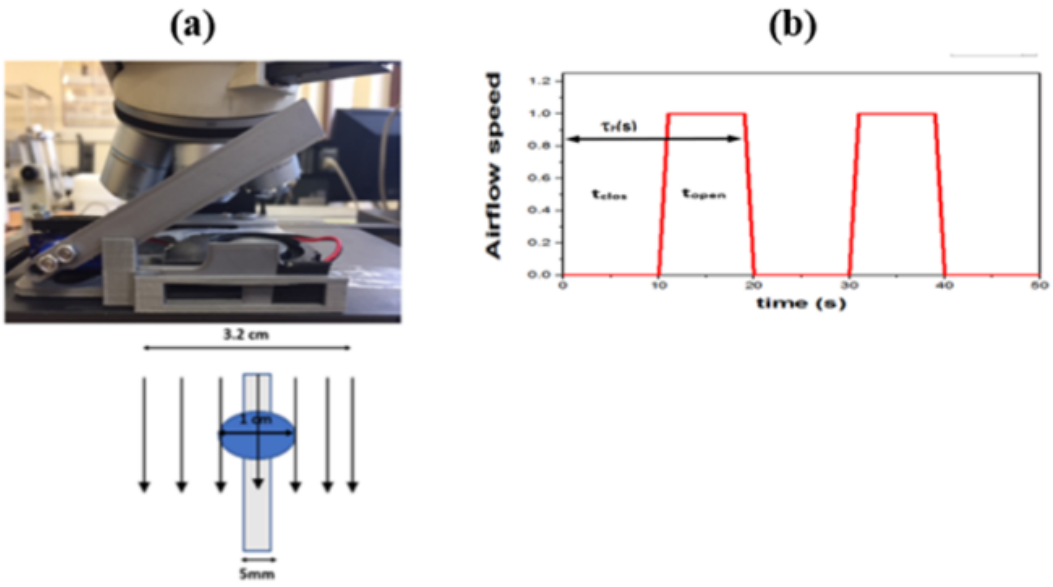

Figure 4.1: (a) A photo of the drying system under a microscope. The system is composed of fan and an arduino controlled shutter. The bottom schema depict the process of drying the sessile drop (1 cm diameter) under a laminar air flow (3.5 cm wide). The long rectangle depicts the zone of interest for the morphology observations and analysis (b) A diagram depicting the periodic opening and closing of the shutter for a time t_{open} and t_{close} for a period of $\tau_p = t_{open} + t_{close}$.

Observation and analyses

The stripe patterns were observed using optical microscope (LEICA, DMLM) during drying using 5x or10x objectives and Motic camera. The light source intensity was reduced in order to reduce the heat effect on the drying. The image analysis was performed using Image J software and home developed program in the Matlab. Glass microscope slides were used in these experiments. Substrates were cleaned with water and alcohol. A modified contact profilemeter device SM7 was used to characterize the film thickness profiles. This device give a depth precision down to 100 nm. This was carried out on cracks free films. The stress on the film was reduced in order to reduce the damage to the film. When films are cracked, a tiny portion of the film was adhered to the glass substrate and the measurement were carried with even slighter stress.

Results

Periodic patterns during drying cleaned suspension under periodic airflow

Drying a cleaned PS/PBA suspension (50/50%) on a glass substrate in free air generates a film with high edges. This results from the capillary flow of particles toward the edge due to the high drying rate on the film border as it was explained by the coffee ring effect.[24, 25] In these conditions, pinning of the drying front on the border leads to a flow and accumulation of particles on the border and when the particle concentration reaches the close-packed fraction 0.64,[59] the dry front advances toward the film center. It has also been shown that the drying front is composed of a reversible and irreversible zones which are distinguishable at low ionic strength and become closer with increasing the ionic strength.[34]
When air is blown on the clean suspension, the drying front moves faster toward the film center. This is due to the high drying rate imposed by the airflow. One should bear in mind that the magnitude of airflow was kept low in order not to perturb the drop shape and only enhances the drying rate. On the other hand, when airflow is periodically modulated between on and off state with a time period τ_p and opening/closing time of (50/50%), periodic lines appear on the top of the drying film as observed by optical microscopy Figure 4.2 (above). The distance between these lines is almost the same for a large part of the film border and extends to a large section of the film leading to a determination of a reliable spatial period λ_p. The spatial period λ_p is directly related to the time period τ_p and increases almost linearly with increasing τ_p. As explained in our previous work, a periodic deposition patterns resulting from periodic drying of colloidal suspension with well resolved line spacing λ_p as those were observed in this work. The λ_p was found to increase with increasing τ_p. The formation of surface structure was

attributed to the dynamic of pining and depinning of the drying front, which yields a preferential deposition of particles on the drying front.

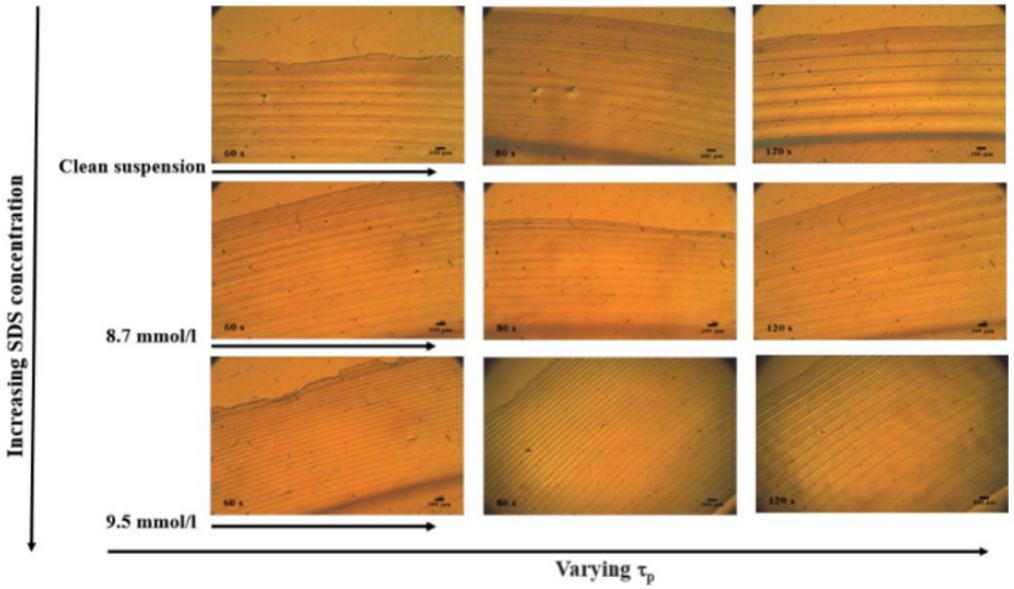

Figure 4.2: Optical microscopy images of stripes pattern of films made by drying sessile drops of (50/50%) blend of (PS/ PBA) under periodic air flow different time periods τ_p (Horizontal). The suspension contains different [SDS]: (Upper) 0 SDS, (middle) 8.7 mmol/l and (below) 9.5 mmol. The periodic airflow is controlled by a fan with arduino controlled shutter. The $t_{open}/\, t_{close}$ was 50/50 and airflow rate 24.6 cm/s. The drying was carried out on glass substrate at room temperature 23^0C and humidity ratio of 34%.

SDS effect on the periodic patterns during drying suspension under periodic airflow

Adding SDS slightly above the CMC (10 mmol/L) modifies drastically the periodic structure. Indeed, the spatial period λ_p is reduced and eventually, the periodic structure almost disappears for a SDS concentration a few times of the CMC at least in the limit of our experimental detection. This behavior is reproducible for all time period τ_p investigated here, which suggests that surfactant is crucial in the dynamic of the drying front and consequently on the periodic structure formation. When the same experiment was repeated with SDS concentration varying between 0 mmol/L and CMC, the structure remains periodic, however, the distance between lines progressively decrease with increasing SDS concentration (Figure 4.2). This suggests that SDS affects mainly the advanced mechanism of deposition line and consequently the distance between the de-

position lines. The spatial period of λ_p estimated from microscopy images progressively decrease with increasing SDS concentration for all the time periods τ_p investigated here. At [SDS] few times CMC, the period does not evolve any more and the lines become too close to be detected leading to a low resolution of periodic structure (Figure 4.3c). Figure 4.4 shows the evolution of the spatial period λ_p vs. the time period τ_p for various SDS concentration from 0 up to 3 times the CMC. As shown before λ_p increases with increasing τ_p for all the cases investigated here. Generally the magnitude of growth of λ_p vs. τ_p decreases with [SDS] (Figure 4.4b). However, one can notice two behaviors, below CMC and above. Below CMC, λ_p increases linearly with increasing τ_p, while above CMC, λ_p become less sensitive to τ_p at high τ_p. To quantify the effect of SDS on the spatial period one can consider the slope of λ_p vs. τ_p or the λ_p value at certain τ_p values. Indeed, the λ_p vs. [SDS] and the slope vs. [SDS] show the same tendency; they decrease slightly with [SDS] below CMC and decreases rapidly at the CMC finally remains almost unchanged above CMC (Figure 4.5). This suggests that the CMC is a critical parameter in setting up the periodic pattern. This behavior is similar to the dependence of surface tension on [SDS]. Indeed the surface tension dependence on [SDS] exhibit the same behavior as λ_p. Which confirm that the periodic structure formation is most likely dominated by the surface tension.
Furthermore above cmc, the periodic structure with narrow λ_p appears only in the first 100 µm and then becomes shallow with large period and eventually disappears.

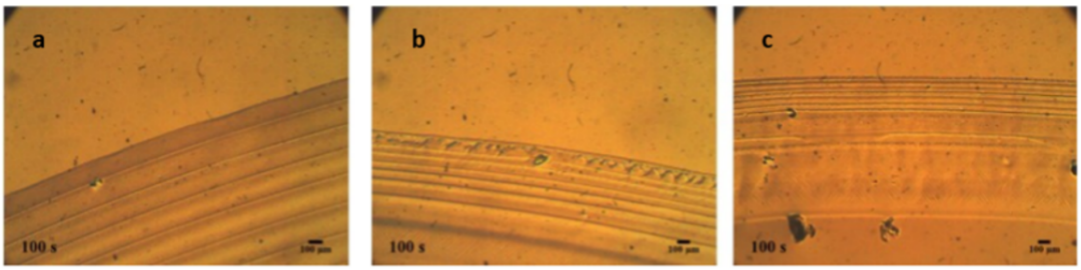

Figure 4.3: Optical microscopy images of stripes pattern of films made by drying 50/50% blends of PS (64nm) and PBA (97.5nm) at 10 wt % under periodic air flow at $\tau_p = 100$ s.The suspension contain: a) 0 SDS, b) 8.7 mmol and c) 13.9 mmol/l. The $t_{open}/\ t_{close}$ was 50/50 and the airflow rate 24.6 cm/s. The periodic airflow is controlled by a fan with arduino controlled shutter.The drying was carried out on glass substrate at room temperature 23^0C and humidity ratio of 34%.

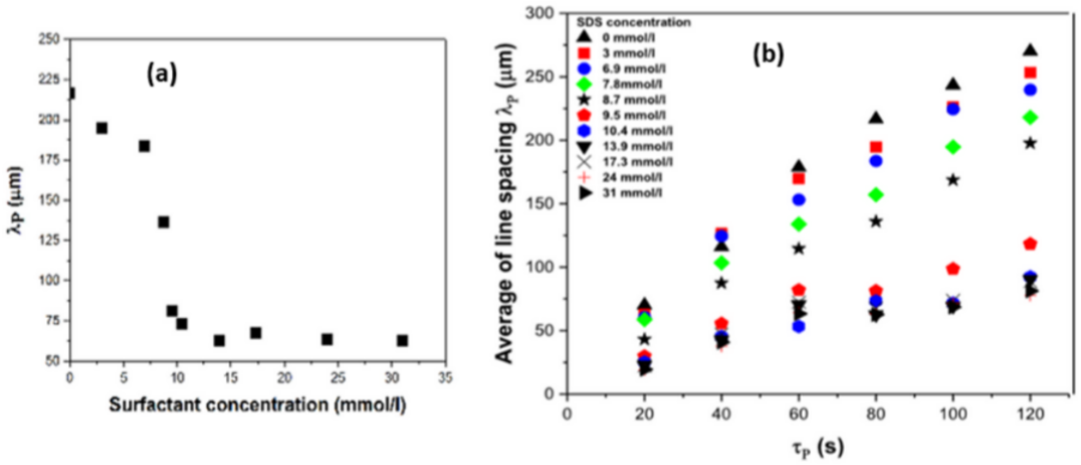

Figure 4.4: (a) Average line spacing λ_p of the periodic patterns of the dry films estimated from microscopy images and plotted as a function of [SDS], where λ_p is calculated at $\tau_p = 80$s.(b) Average line spacing (λ_p) for various SDS concentration from 0 up to 3 times the CMC plotted vs. τ_p. The films are made by drying sessile drops of (50/50%) blend of (PS/ PBA) at different concentrations of SDS under periodic air flow with fixed $t_{open}/\ t_{close}$ (50/50%) and variable τ_p between 20 s to 120 s.The drying was carried out on glass substrate at room temperature 23^0C and humidity ratio of 34% and airflow rate 24.6 cm/s.

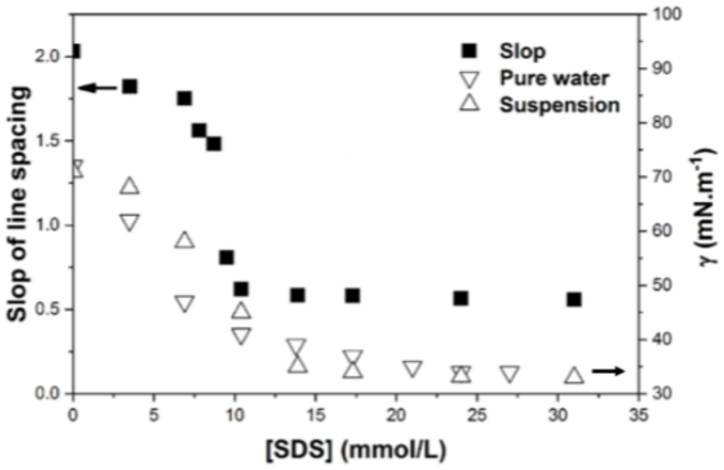

Figure 4.5: Slope of line spacing λ_p vs.τ_p (■) calculated from Figure 4.4b and plotted vs. [SDS]. The surface tension measurement (γ) obtained by the drop pendent method and plotted as a function of SDS concentration for: Particles suspension (△) and pure water (▽).

3D morphology of the periodic pattern in the presence of SDS.

The periodic patterns seen in optical microscopy correspond to a structure of hills and valley build up during the drying. The analysis of these structures using a profilometer gives a profile of oscillating hills and valleys for which we can extract three characteristic parameters; the average period (λ_p) the average height (h_p) and average width (w_p). In the absences or very low [SDS], h_p was found to increase from almost 0.2 μm to 1.1 μm with increasing τ_p between 20s to 120s with $t_{open}/\, t_{close}$ (50/50%) (Figure 4.6). However, adding SDS below CMC lead to a reduction of both h_p in a similar manner as λ_p and eventually becomes undetectable for our experimental conditions. When [SDS] is above CMC, both the λ_p and h_p close to the border (less than 100 μm becomes too small to be reliably quantified. Furthermore far from the border the film is flat and the h_p becomes to small to be measured.

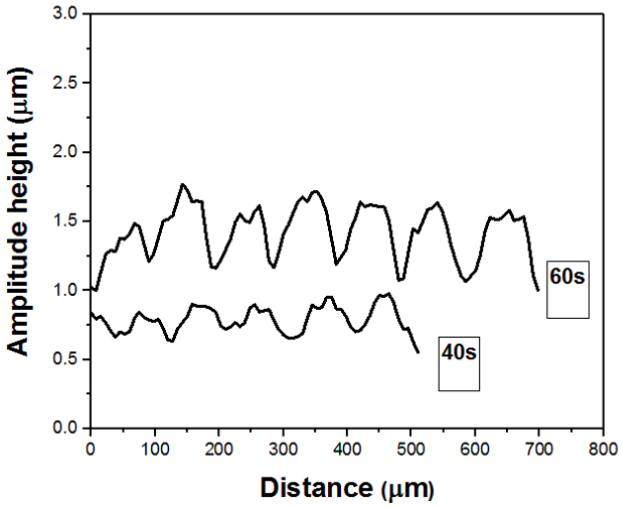

Figure 4.6: Height profile of film made by drying (50/50%) PS(64nm)/PBA(97.5 nm) blends containing negligible SDS concentration. The film are made by drying sessile drop under periodic airflow for time period $\tau_p = 40$s and $\tau_p = 60$s. The height profile was measured using contact a profilemeter. The $t_{open}/\, t_{close}$ was set to 50/50%. The drying was carried out on glass substrate at room temperature 23^0C and humidity ratio of 34%. The profiles are estimated by taking the film surface as a baseline and shifted vertically for clarity.

Effect of SDS concentration on the behavior of the drying front dynamics

The dynamic of the drying front under periodic airflow was investigated in order to understand the mechanism of patterns formation. The drying front seen in our visualisation is a zone of a typical width between 65 μm to 117 μm depending on the experimental conditions (in the conditions of low airflow speed), depicting the transition between the liquid state and solid state.[34] This area is composed of 2 domains with different aspects separated by 3 lines (Figure 4.7-4.10). The manifestation of these zones depends on the geometry if the drop as well as the physical chemistry of the suspension ([SDS], [KCl]. For example in the absence of SDS or at low [SDS], The first zone is characterized by a change in the film coloration in with a typical width of 26 μm -58.5 μm (in our experimental condition of low air flow speed), starting at an onset line (OL) and ending at a first line (FL) (Figure 4.7). This zone corresponds to the transition between a colloidal gel to a solid film. The second zone is a wider area characterized by shear bands lines particularly during air flow regime and extends to about starting at the FL and extending to a second line (SL) (Figure 4.7). When particles are incorporated as tracer in the suspension to characterise the flows, no activity is seen in this zone. For [SDS] above cmc the contrast of the first line becomes low leading to detection uncertainty with increasing [SDS]. On the other hand, the SL is seen throughout the drying process (Figure 4.8). In all cases, the drying front region advances, unidirectionally, from the border of the film towards the center with a velocity which dependent on the magnitude of airflow. Under periodic airflow, in the absence of SDS, the OL and FL lines moves periodically; it advances during airflow and almost arrest when airflow stops (Figure 4.7, Figure 4.11 and Figure S4.2a). Although it is clear that the second line SL advances ahead of the OL, the contrast is not sufficient to resolve its position with the required precision to state on the periodicity of the movement. On the other hand, adding SDS, modifies the drying front dynamic under modulated air flow for all the three lines of the drying front as well as for the two zones. At [SDS] above CMC, the SL line advances rapidly during airflow, while the OL one advances very slowly (Figure 4.8, Figure 4.11 and Figure S4.3). When the airflow stops, the OL stops advancing while the SL line recedes back and approaches the onset line (Figure 4.11, Figure S4.3). The receding distance (h_{rec}) is estimated from the descending part of Figure 4.11b, averaged and plotted in Figure 4.12a. h_{rec} was found to increase with increasing [SDS], slightly below CMC, then rapidly in the vicinity of CMC and levels off above CMC (Figure 4.12 a). On the other hand, the advancing distance (h_{adv}) of the SL, taken from the ascending part of Figure 4.11b, decreases with increasing [SDS], slightly below CMC, then rapidly in the vicinity of CMC and levels off above CMC (Figure 4.12a).

The effective OL advancing resulting from an advancing and receding mechanisms calculated as the difference between the h_{adv} - h_{rec} is plotted in Figure 4.12b. This shows that the average OL advances is sensitive to [SDS] and follows the same tendency as the

tension, which suggests that the surface tension plays an important role in controlling this process.

Furthermore, Figure 4.13 shows the velocity of the advancing and receding of the OL line during periodic air flow. Two information can be noted here: i) the velocity of the advancing part decreases with increasing [SDS] for all τ_p values investigated here.ii) As for the velocity of receding part, it was estimated for [SDS] above CMC and was found to give almost similar value.

These evolution of the drying fronts dynamic with increasing [SDS] could either be the result of a change in the surface tension of the suspension which leads to a major modifications of the contact angle or to a modification of the ionic strength resulting from the counter ions of the SDS. To elucidate this question KCl salt is added to the suspension instead of SDS and the evolution of the drying front with increasing [KCl] is investigated. The 2 zones and the 3 lines appears through out the drying process (Figure 4.9). The SL advances steadily during the two drying regimes and throughout the drying process and does not show any sign of receding as in the case of the SDS. The OL and FL shows slight periodic movement with advancing and stopping steps (Figure S4.4). This suggests that the effect of the receding of the SL and slow advancing of the OL in the presence of SDS is unlikely to results from the variation of the ionic strength.

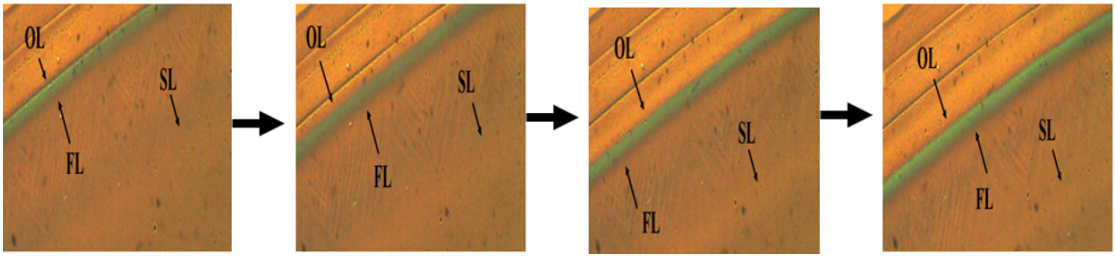

Figure 4.7: Onset line (OL), first line (FL) and second line (SL) of the drying front during 4 stages of drying a clean 50/50% (PS/PBA) blend in the absence of SDS and KCl. The drying was carried out under periodic airflow with $\tau_p = 80$ s and $t_{open}/\ t_{close}$ (50/50%) on glass substrate at room temperature 23^0C and humidity ratio of 34% and airflow rate 24.6 cm/s.

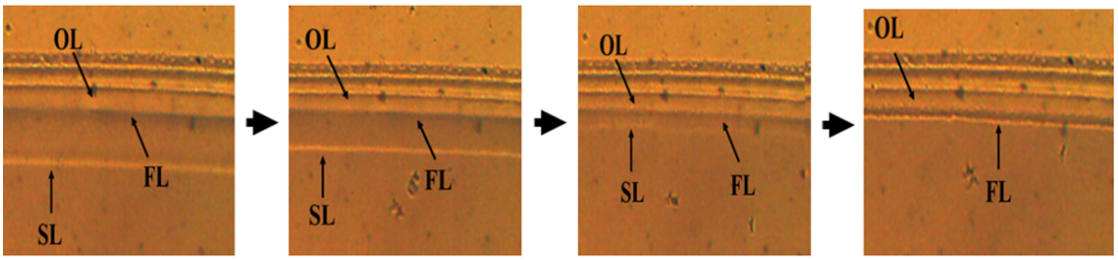

Figure 4.8: Onset line (OL), first line (FL) and second line (SL) of the drying front during 4 stages of drying a clean 50/50% (PS/PBA) blend in the presence of SDS for [SDS] above cmc ([SDS] = 13.9 mmol/L). The drying was carried out under periodic airflow with $\tau_p = 80 sand t_{open}/\ t_{close}$ (50/50%) on a glass substrate at room temperature 23^0C and humidity ratio of 34% and airflow rate 24.6 cm/s.

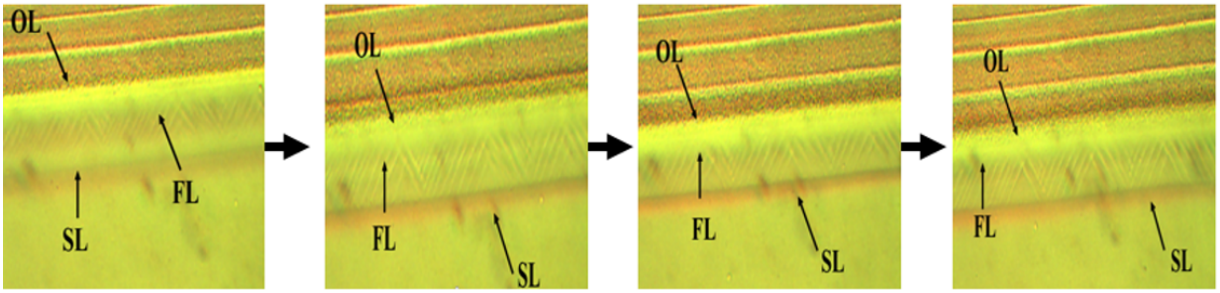

Figure 4.9: Onset line (OL), first line (FL) and second line (SL) of the drying front during 4 stages of drying a clean 50/50% (PS/PBA) blend in the presence of [KCl] ([KCl] = 5 mmol/L). The drying was carried out under periodic airflow with $\tau_p = 80 sand t_{open}/\ t_{close}$ (50/50%) on a glass substrate at room temperature 23^0C and humidity ratio of 34% and airflow rate 24.6 cm/s

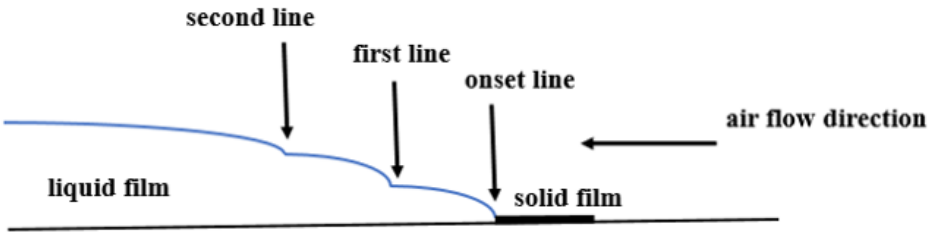

Figure 4.10: Schema depicting the two zones of the drying front during drying a sessile drop under a laminar air flow. The onset line (OL) close to solid film, second line (SL) close to liquid film and the first line (FL) is located between OL and SL.

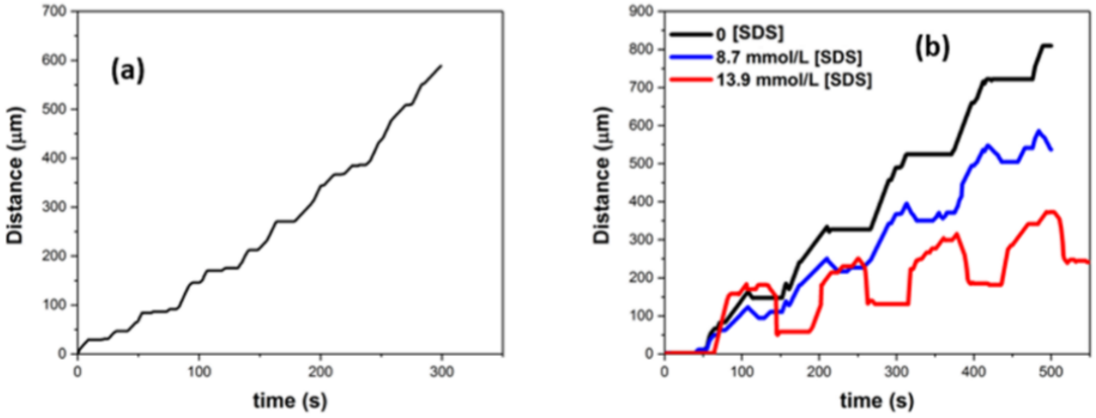

Figure 4.11: Position of the drying front estimated from microscopy visualisation plotted vs. the drying time, during drying a (50/50%) blend of(PS/PBA) : (a) drying under no air flow in the absence of SDS, b) the suspension is dried under time modulated air flow for different SDS concentration [SDS] = 0, 8.7, and 13.9 mmol. The drying was carried out under periodic air flow with $\tau_p = 80s$ and $t_{open}/\ t_{close}$ (50/50%) at room temperature 23^0C and humidity ratio of 34% and airflow rate 24.6 cm/s.

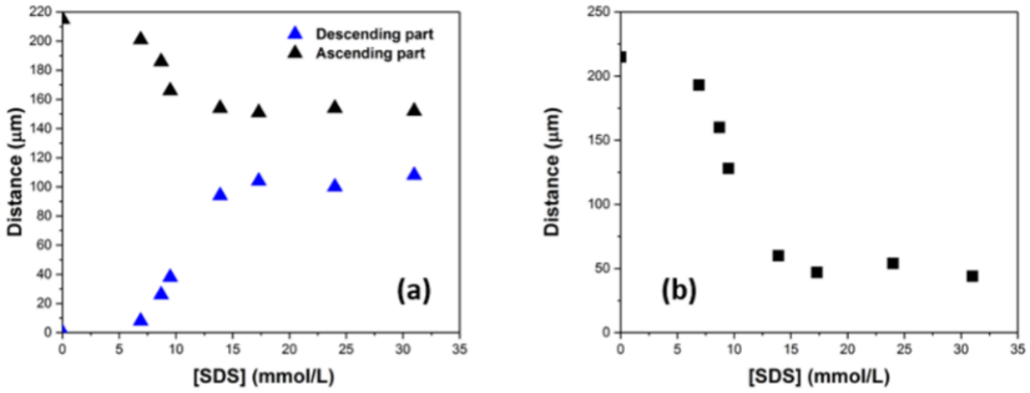

Figure 4.12: (a) Average magnitude of the ascending and descending part of the second line (SL) of the drying front plotted as a function of [SDS]. This was estimated from Figure 4.11b during drying a blend of (PS/PBA) under periodic air flow with $\tau_p = 80s$ and $t_{open}/\, t_{close}$ (50/50%) at room temperature 23^0C and humidity ratio of 34% and airflow rate 24.6 cm/s. (b) The difference between the ascending and the descending parts of the drying front taken from Figure 4.12a and plotted vs.[SDS].

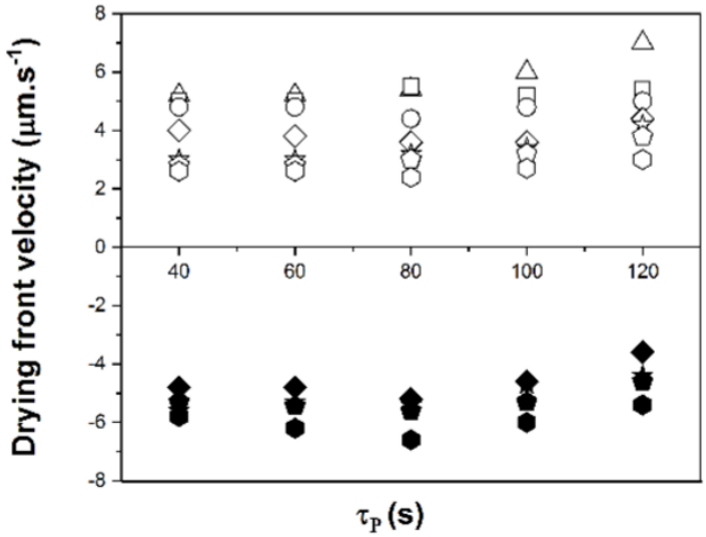

Figure 4.13: The averages drying front velocity in both the advancing and the receding state during drying a mixture of PS/PBS (50/50%) containing different amount of SDS at air flow rate 24.6 cm/s. In open position: 0 (△), 6.9 mmol/l (□), 8.7 mmol/l (○), 13.9 mmol/l (◇), 17.3 mmol/l (☆), 24 mmol/l (⬠), 31 mmol/l (⬡). While in close position: 13.9 mmol/l (◆), 17.3 mmol/l (★), 24 mmol/l (⬟), 31 mmol/l (⬢).

Discussion

Mechanism of pattern formation in the absences of SDS

Drying a latex suspension under periodic airflow most likely modulates the drying rate between two states: a slow evaporation regime for t_{close} under no airflow, and a fast evaporation regime for t_{open} under airflow. On clean suspensions and in the absence of SDS, the periodic 3D structure results from the periodic repetition of two different regimes of particle deposition on the drying front. The magnitude of particle deposition is controlled by how the drying front advances from the film border to the center. In the absence of SDS, the OL and FL of drying front advances when air flows and arrests when air stops. During the arrests regime, capillary flux resulting from the coffee ring effect leads to particles deposition at the drying front.[24] Indeed, because the drying rate is enhanced at the drying front, capillary flux brings particles to the drying front leading to an enhanced accumulation and therefore to the formation of hills. During airflow, the drying front advances faster which limits particle deposition, lesser their accumulation, and therefore creates valleys.

Beyond the simple model described above, the hills amplitude likely to result from the competition between the magnitude of the capillary flux and the advancing velocity of the drying front. Therefore, one could account for this 3D structure by taking into account the horizontal drying gradient, the drying rate as well as the magnitude of the capillary flux, and how it is influenced by the suspension viscosity. This problem raises the question: what is the drying front and how to quantify it in optical microscopy visualization?. The drying front is usually considered to be a sharp transition line between a reversible and irreversible state of the colloidal suspension and in the case of stable particles to the close-packed concentration 0.64.[60] However, the drying front has also been found to correspond to a large transition zone between the reversible and the irreversible states. [34] In the absence of airflow, the horizontal concentration gradient within the drying front area improves due to the particles deposition by capillary flow, especially when the drying front is not advancing, leading to hills formation. The drying rate gradient also enhances the concentration gradient in the vicinity of the drying front in the absence of airflow. Furthermore, the airflow enhances the vertical drying rate, concentrates the suspension, and causes the concentrated but reversible areas near the drying front to go into an irreversible state, which generates rapid advance of the drying front. The conjunction of the rapid advance of the drying front with slower capillary flux yields a limited particle accumulation on the drying front and valleys formation. The reduction in hills amplitude with a decrease of τ_p can also be explained in terms of this model. Reducing τ_p with the constant $\frac{t_{close}}{\tau_p}$ (0.5), decreases t_{close}, which gives a limited accumulation of particles at the drying front and reduces the hills amplitude. An alternative explanation is that the hills amplitude depends on λ_p and not on t_{close}. This model

can also predict the observed patterns period. Indeed, because the deposition and accumulation of the particles occur during the drying front arrest regime, the spatial period λ_p most likely corresponds to the distance between the successive stopping positions.

Pattern formation in the presence of SDS

The addition of SDS considerably affects the 3D patterns as well as the dynamics of the drying front (Figure 4.2) and (Figure 4.11). These results raise two issues: i) can we quantify patterns morphology using the drying front dynamic as in the case of [SDS] = 0 and ii) why the drying front recedes in the presence of SDS. Figure 4.12a shows that the amplitude of the drying front advancing decreases while that of receding increases with increasing SDS in the range of CMC. The difference between these distances almost gives a similar value to the spatial period λ_p (Figure 4.12b). This comforts the previous finding according to which the spatial period λ_p equals the distance between two successive arresting regimes. As for the hills and valleys amplitudes, they decrease with increasing [SDS] up to CMC and eventually vanish or become undetectable, at least for our detection limit for [SDS] above 2 CMC. The hills amplitude h_p decreases with increasing SDS, following the same trend as the reduction of λ_p. It should be borne in mind that τ_p remains constant when varying [SDS], which suggests that the reduction of the hills amplitude is mainly due to the decrease of λ_p with increasing [SDS] rather than a change in t_{close}. Therefore the hills amplitude h_p is controlled by the distance between two successive stopping positions of the drying front.

Dynamic behavior of the drying front

It is most likely that the formation of the periodic patterns to be controlled by the dynamic of the drying front and how it advance and how it stops and recedes. The average advancing velocity of the onset line (V_{onset}) decreases with increasing [SDS] and undergoes an important change at the CMC, which similar to the behavior of the patterns period λ_p (Figure 4.4), which infers that the patterns period is controlled by the advancing and stopping of the onset line of the drying front. The decrease of (V_{onset}) with increasing [SDS] can either be geometrical effect due to reduction of the film thickness with increasing [SDS] as the contact angle decreases (Figure S4.1 in Supporting Formation) or to the reduction of the surface tension. On the other hand, the second line advances during airflow and recedes back close to the position of the onset line once air flow stops. The amplitude of this forward and backward movement increase with increasing [SDS] and undergoes an important variation at the CMC (Figure 4.11b) which strongly suggests that the surface tension plays an important role in this process. Furthermore, the distance between the advancing and receding positions shows the same behavior as spatial period λ_p Figure 4.12b, which comfort the conclusion that the period of the patterns is mainly defined by the difference between the positions of the onset of drying front.

To acquire further information about the transition from reversible to irreversible in the drying front area, large particles were added to the suspension and their motion was observed throughout the drying process. No motion was detected ahead of the onset line, which suggests that this zone corresponds to an irreversible solid. On the other hand, a very limited motion was detected between the onset line (OL) and the SL lines which comfort the conclusion that this is a reversible-to-irreversible transitional zone. [34]. Yet no strong flux is observed within this zone contrary to the observed flux beyond SL.

At the first glance, the backward-forward movement could be attributed to the solutal or thermal Marangoni effect which is well known to induce a reverse flow close to the drying front.[52, 61] The addition of SDS below CMC yields a change in surface tension between 72 mN/m and 32 mN/m (Figure 4.5). [SDS] increases in the drying front area as a result of radial drying, which could yield a reduction of $(\gamma_{air-liquid})$ in this zone and can create $(\Delta\gamma_{air-liquid})$ gradient which in turns initiates Marangoni effect and a reverse flow. However, Marangoni flow is visualized in these experiments using the large probe particles and is found much slower than the receding process and therefore can not account for the observation. Furthermore, the Marangoni effect is expected to saturate above CMC where $(\gamma_{air-liquid})$ is less sensitive to [SDS].[53, 62] This is contrary to the observed mechanism where the backward-forward amplitude reaches a maximum close to CMC.

The receding could also be attributed to the transition between two regimes of the contact angles. The contact angle decreases with increasing [SDS] from 23^0 in the absence of SDS to around 3.5^0 above cmc, which could be an argument in favor of this explanation (See Figure S4.1 in Supporting Formation). Indeed, [SDS] increases within the drying front area due to the high drying rate in this zone during airflow, leading to a reduced $(\gamma_{air-liquid})$ and smaller contact angle. When airflow stops, the Osmotic pressure redistributes SDS which could induce a return of the contact angle to its initial state and generates a receding of the drying front. Though such a mechanism can account for the observed results below CMC, it is expected to saturate and disappear above, which is contrary to the observed results. Therefore, this process cannot account for the backward-forward mechanism, particularly above CMC. The suspension viscosity is found to decreases with increasing [SDS] due to the ionic-strength of the SDS counter ions, which screens the electrostatic repulsion between the particles. The suspension viscosity is an inhibiting parameter for the capillary flux and therefore could affects the backward-forward movement. Controlled drying experiments were repeated in the suspension containing controlled ionic strength using KCl. No receding was observed in these experiments as in the case of SDS, which suggests that viscosity does not play a role in this process (See Figure S4.4 in Supporting Formation). The colloidal interactions and their stability diagram was found to play an important role in defining the shape and behavior of the drying front zone. [34] Adsorbing SDS on the particle modifies the interactions of the particles and consequently could also modify the drying font

behavior.[63] In the absence of SDS, the particles of this study were analyzed in both conductivity and elemental analysis and were found to contain 300-700 sulfate groups on their surface.[64] Part of the added SDS, adsorbs on the particle surface, which could enhance the short-range repulsion between the particles by adding sulfate charges to their surface and therefore extend their stability domain.[65] During airflow the drying front region become more concentrated but could remain reversible due to the SDS stabilization. Once stopping airflow, the concentrated domain redisperses via osmotic pressure, which could induce the backward movement of the endset line.[63] .

Conclusion

Periodic surface patterns were made by drying colloidal suspensions under time modulated drying rate conditions with alternating on / off airflow. The effects of sodium dodecyl sulfate (SDS) surfactant on the dynamics of the drying front and on the resulting 3D surface morphology were investigated. Periodic surface patterns have been observed for low [SDS], with a period λ_p. λ_p decreases with increasing [SDS], shows a sharp change at CMC, and follows the same trend as surface tension. This underlines the importance of surface tension in the mechanism of periodic pattern formation. Profilometer measurements show that these structures consist of hills and valleys whose amplitude decreases with increasing [SDS]. Above CMC, the period and the hills become too small to be discernible. The periodic structure was found to result from the alternation of two different regimes of particle deposition on the drying front. The particle deposition is controlled by the advance dynamics and stop of the drying front during its movement under periodic airflow. In the absence of SDS, the drying front area advances during the airflow and stops when airflow stops. In the presence of SDS, the onset of the drying front advances with a low velocity. On the other hand, the endset or SL of the drying front was found to advance rapidly during airflow and to recede back to the onset line once the airflow stops. These dynamics were found to follow a similar trend of the surface tension which suggests that the surface tension plays a significant role in this process.

*Supporting information

Control of surface morphology during evaporation of colloidal suspension containing ionic surfactant under periodic airflow

Essa shawail[a], *Yahya Rharbi*[a,b]
(a) Univ.Grenoble Alpes - LRP, F-38041 Grenoble, FRANCE
(b) CNRS, LRP , F-38041 Grenoble, FRANCE
Corresponding Author Email: yahya.rharbi@univ-grenoble-alpes.fr

content

Figures S4.1-S4.4

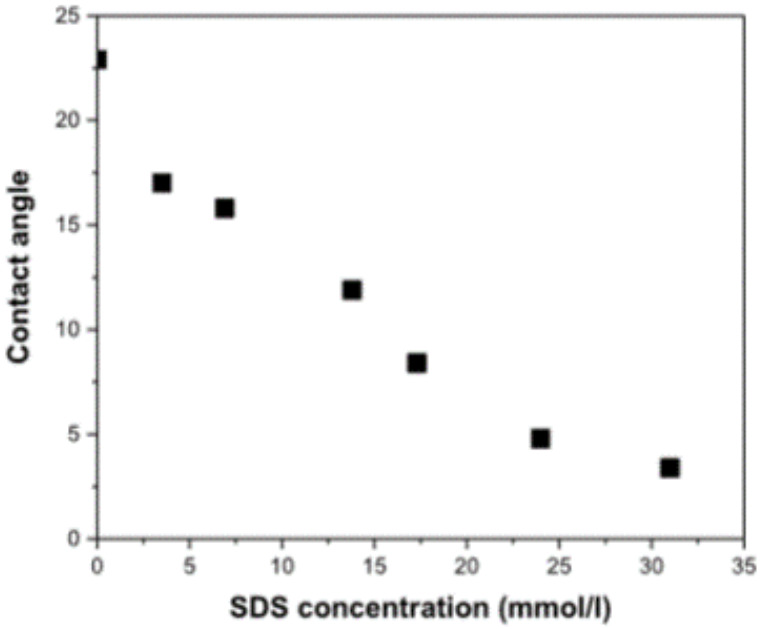

Figure S4.1: Contact angle of PS/PBA blends (50/50%) containing SDS plotted vs. SDS concentration. The contact angle is measured on glass substrate at room temperature 23^0C and humidity ratio of 34%.

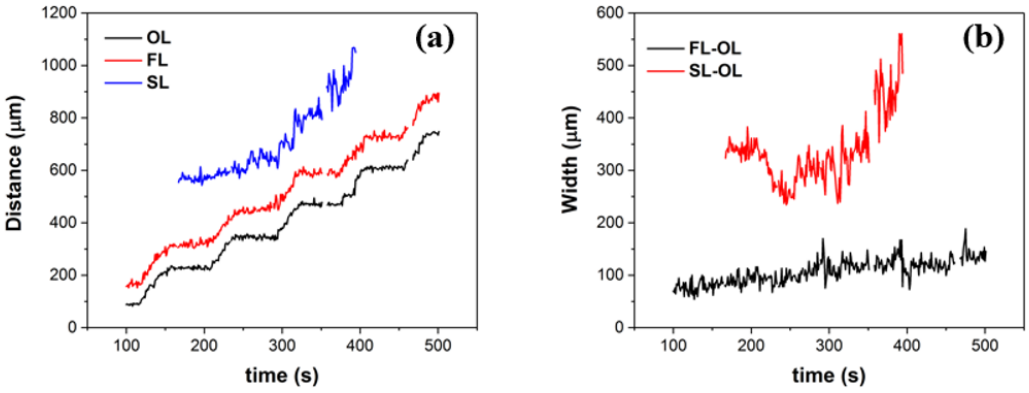

Figure S4.2: a) Position of the three lines of the drying front (OL, FL, and SL) estimated from microscopy visualisation plotted vs. the drying time, during drying a clean (50/50%) blend of(PS/PBA) in the absence SDS under periodic air flow. The drying was carried out with $\tau_p = 80s$ and $t_{open}/\, t_{close}$ (50/50%) at room temperature 23^0C and humidity ratio of 34% and airflow rate 24.6 cm/s. b) Time evolution of the distance between OL and Fl and OL and SL.

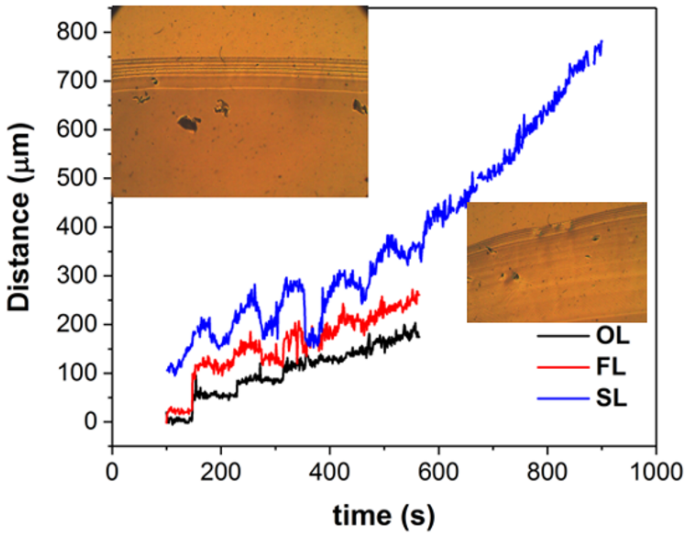

Figure S4.3: Position of the three lines of the drying front (OL, FL, and SL) estimated from microscopy visualisation plotted vs. the drying time, during drying a clean (50/50%) blend of(PS/PBA) in the presence of SDS ([SDS] = 13.9 mmol/L under periodic air flow. The drying was carried out with $\tau_p = 80s$ and $t_{open}/\ t_{close}$ (50/50%) at room temperature 23^0C and humidity ratio of 34% and airflow rate 24.6 cm/s.inset: images of the drying front at different drying times.

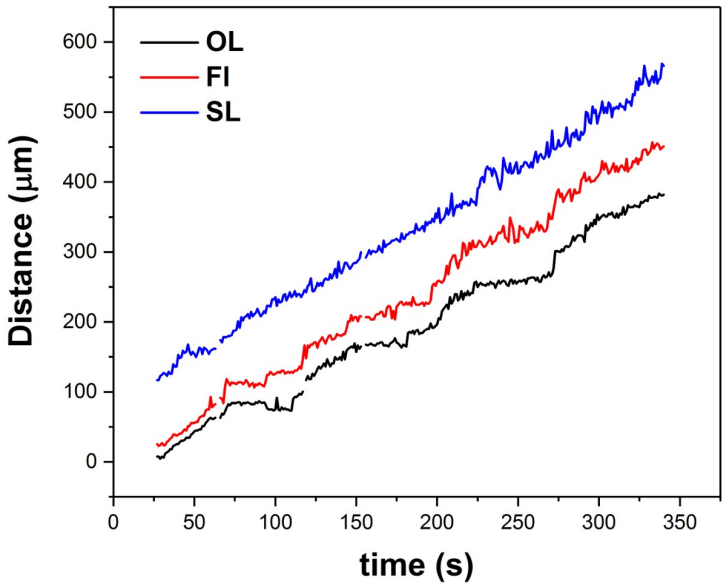

Figure S4.4: Position of the three lines of the drying front (OL, FL, and SL) estimated from microscopy visualisation plotted vs. the drying time, during drying a clean (50/50%) blend of(PS/PBA) in the presence of KCl ([KCl] = 5 mmol/L) under periodic air flow. The drying was carried out with $\tau_p = 80s$ and $t_{open}/\ t_{close}$ (50/50%) at room temperature 23^0C and humidity ratio of 34% and airflow rate 24.6 cm/s.

Bibliography

[1] Leonid Shmuylovich, Amy Q Shen, and Howard A Stone. Surface morphology of drying latex films: Multiple ring formation. *Langmuir*, 18(9):3441–3445, 2002.

[2] C Nadir Kaplan, Ning Wu, Shreyas Mandre, Joanna Aizenberg, and Lakshminarayanan Mahadevan. Dynamics of evaporative colloidal patterning. *Physics of Fluids*, 27(9):092105, 2015.

[3] Udita Uday Ghosh, Monojit Chakraborty, Soham De, Suman Chakraborty, and Sunando DasGupta. Contact line dynamics during the evaporation of extended colloidal thin films: Influence of liquid polarity and particle size. *Langmuir*, 32(48):12790–12798, 2016.

[4] A Susarrey-Arce, A Marin, A Massey, A Oknianska, Y Díaz-Fernandez, JF Hernández-Sánchez, E Griffiths, Johannes GE Gardeniers, Jacobus Hendrikus Snoeijer, Detlef Lohse, et al. Pattern formation by staphylococcus epidermidis via droplet evaporation on micropillars arrays at a surface. *Langmuir*, 32(28):7159–7169, 2016.

[5] Maryam Parsa, Souad Harmand, and Khellil Sefiane. Mechanisms of pattern formation from dried sessile drops. *Advances in colloid and interface science*, 254:22–47, 2018.

[6] Duyang Zang, Sujata Tarafdar, Yuri Yu Tarasevich, Moutushi Dutta Choudhury, and Tapati Dutta. Evaporation of a droplet: From physics to applications. *Physics Reports*, 2019.

[7] Emine Tekin, Patrick J Smith, and Ulrich S Schubert. Inkjet printing as a deposition and patterning tool for polymers and inorganic particles. *Soft Matter*, 4(4):703–713, 2008.

[8] Dan Soltman and Vivek Subramanian. Inkjet-printed line morphologies and temperature control of the coffee ring effect. *Langmuir*, 24(5):2224–2231, 2008.

[9] Laxmidhar Nayak, Smita Mohanty, Sanjay Kumar Nayak, and Ananthakumar Ramadoss. A review on inkjet printing of nanoparticle inks for flexible electronics. *Journal of Materials Chemistry C*, 7(29):8771–8795, 2019.

[10] Hyoungsoo Kim, François Boulogne, Eujin Um, Ian Jacobi, Ernie Button, and Howard A Stone. Controlled uniform coating from the interplay of marangoni flows and surface-adsorbed macromolecules. *Physical review letters*, 116(12):124501, 2016.

[11] Berend-Jan de Gans and Ulrich S Schubert. Inkjet printing of well-defined polymer dots and arrays. *Langmuir*, 20(18):7789–7793, 2004.

[12] Angkur Jyoti Dipanka Shaikeea and Saptarshi Basu. Evaporating sessile droplet pair: Insights into contact line motion, flow transitions and emergence of universal vaporisation pattern. *Applied Physics Letters*, 108(24):244102, 2016.

[13] Rajarshi Guha, Farzad Mohajerani, Ahana Mukhopadhyay, Matthew D Collins, Ayusman Sen, and Darrell Velegol. Modulation of spatiotemporal particle patterning in evaporating droplets: applications to diagnostics and materials science. *ACS applied materials & interfaces*, 9(49):43352–43362, 2017.

[14] Khellil Sefiane. On the formation of regular patterns from drying droplets and their potential use for bio-medical applications. *Journal of Bionic Engineering*, 7(4):S82–S93, 2010.

[15] Huaixia Zhao, Jiajia Xu, Guangyin Jing, Lizbeth Ofelia Prieto-López, Xu Deng, and Jiaxi Cui. Controlling the localization of liquid droplets in polymer matrices by evaporative lithography. *Angewandte Chemie International Edition*, 55(36):10681–10685, 2016.

[16] Lauryanne Teulon, Yannick Hallez, Simon Raffy, Francois Guerin, Etienne Palleau, and Laurence Ressier. Electrostatic directed assembly of colloidal microparticles assisted by convective flow. *The Journal of Physical Chemistry C*, 123(1):783–790, 2018.

[17] Yuanyi Zhang, Colton A D'Ambra, Reika Katsumata, Ryan L Burns, Mark H Somervell, Rachel A Segalman, Craig J Hawker, and Christopher M Bates. Rapid and selective deposition of patterned thin films on heterogeneous substrates via spin coating. *ACS applied materials & interfaces*, 11(23):21177–21183, 2019.

[18] Xue Li and James F Gilchrist. Large-area nanoparticle films by continuous automated langmuir–blodgett assembly and deposition. *Langmuir*, 32(5):1220–1226, 2016.

[19] Mayuresh Kulkarni, Subhadarshinee Sahoo, Pankaj Doshi, and Ashish V Orpe. Fingering instability of a suspension film spreading on a spinning disk. *Physics of Fluids*, 28(6):063303, 2016.

[20] Chih-Ting Liu, Chia-Chan Tsai, Chien-Wei Chu, Mu-Huan Chi, Pei-Yun Chung, and Jiun-Tai Chen. Dewetting of polymer thin films on modified curved surfaces: preparation of polymer nanoparticles with asymmetric shapes by anodic aluminum oxide templates. *Soft matter*, 14(15):2772–2776, 2018.

[21] Ryuichi Sakamoto, Yoshiki Hataguchi, Ryosuke Kimura, Katsumi Tsuchiya, and Yasushige Mori. Stripe and network formation of particle arrays fabricated by convective self-assembly. *Chemistry Letters*, 41(10):1207–1209, 2012.

[22] Yasushi Mino, Satoshi Watanabe, and Minoru T Miyahara. Colloidal stripe pattern with controlled periodicity by convective self-assembly with liquid-level manipulation. *ACS applied materials & interfaces*, 4(6):3184–3190, 2012.

[23] Tatsuya Hanafusa, Yasushi Mino, Satoshi Watanabe, and Minoru T Miyahara. Controlling self-assembled structure of au nanoparticles by convective self-assembly with liquid-level manipulation. *Advanced Powder Technology*, 25(2):811–815, 2014.

[24] Robert D Deegan, Olgica Bakajin, Todd F Dupont, Greb Huber, Sidney R Nagel, and Thomas A Witten. Capillary flow as the cause of ring stains from dried liquid drops. *Nature*, 389(6653):827–829, 1997.

[25] Robert D Deegan, Olgica Bakajin, Todd F Dupont, Greg Huber, Sidney R Nagel, and Thomas A Witten. Contact line deposits in an evaporating drop. *Physical review E*, 62(1):756, 2000.

[26] E Rio, A Daerr, François Lequeux, and Laurent Limat. Moving contact lines of a colloidal suspension in the presence of drying. *Langmuir*, 22(7):3186–3191, 2006.

[27] G Guéna, C Poulard, and A-M Cazabat. The dynamics of evaporating sessile droplets. *Colloid Journal*, 69(1):1–8, 2007.

[28] Anaïs Gauthier, Marco Rivetti, Jérémie Teisseire, and Etienne Barthel. Role of kinks in the dynamics of contact lines receding on superhydrophobic surfaces. *Physical review letters*, 110(4):046101, 2013.

[29] Xuemin Ye, Xiangshan Zhang, Minglan Li, Chunxi Li, and Shuai Dong. Contact line dynamics of two-dimensional evaporating drops on heated surfaces with temperature-dependent wettabilities. *International Journal of Heat and Mass Transfer*, 128:1263–1279, 2019.

[30] Asher P Mouat, Clay E Wood, Justin E Pye, and Justin C Burton. Tuning contact line dynamics and deposition patterns in volatile liquid mixtures. *Physical Review Letters*, 124(6):064502, 2020.

[31] Wu-Zhi Yuan and Li-Zhi Zhang. Pinning–depinning mechanisms of the contact line during evaporation of microdroplets on rough surfaces: A lattice boltzmann simulation. *Langmuir*, 34(26):7906–7915, 2018.

[32] Aiting Gao, Jie Liu, Lijun Ye, Clarissa Schonecker, Michael Kappl, Hans-Jurgen Butt, and Werner Steffen. Control of droplet evaporation on oil-coated surfaces for the synthesis of asymmetric supraparticles. *Langmuir*, 35(43):14042–14048, 2019.

[33] Steven Armstrong, Glen McHale, Rodrigo Ledesma-Aguilar, and Gary G Wells. Pinning-free evaporation of sessile droplets of water from solid surfaces. *Langmuir*, 35(8):2989–2996, 2019.

[34] Lucas Goehring, William J Clegg, and Alexander F Routh. Solidification and ordering during directional drying of a colloidal dispersion. *Langmuir*, 26(12):9269–9275, 2010.

[35] Charles Loussert, Frédéric Doumenc, Jean-Baptiste Salmon, Vadim S Nikolayev, and Béatrice Guerrier. Role of vapor mass transfer in flow coating of colloidal dispersions in the evaporative regime. *Langmuir*, 33(49):14078–14086, 2017.

[36] Oscar Giraldo, Jason P Durand, Harikrishnan Ramanan, Kate Laubernds, Steven L Suib, Michael Tsapatsis, Stephanie L Brock, and Manuel Marquez. Dynamic organization of inorganic nanoparticles into periodic micrometer-scale patterns. *Angewandte Chemie*, 115(25):3011–3015, 2003.

[37] Mohamed Asbahi, FuKe Wang, Zhaogang Dong, Joel KW Yang, and Karen SL Chong. Directed self-assembly of sub-10 nm particle clusters using topographical templates. *Nanotechnology*, 27(42):424001, 2016.

[38] KS Birdi and DT Vu. Wettability and the evaporation rates of fluids from solid surfaces. *Journal of adhesion science and technology*, 7(6):485–493, 1993.

[39] AR Harikrishnan, Purbarun Dhar, Sateesh Gedupudi, and Sarit K Das. Effect of interaction of nanoparticles and surfactants on the spreading dynamics of sessile droplets. *Langmuir*, 33(43):12180–12192, 2017.

[40] S Chandra, M Di Marzo, YM Qiao, and Paolo Tartarini. Effect of liquid-solid contact angle on droplet evaporation. *Fire safety journal*, 27(2):141–158, 1996.

[41] Victoria Dutschk, Konstantin G Sabbatovskiy, Martin Stolz, Karina Grundke, and Victor M Rudoy. Unusual wetting dynamics of aqueous surfactant solutions on polymer surfaces. *Journal of colloid and interface science*, 267(2):456–462, 2003.

[42] Merve Dandan Doganci, Belma Uyar Sesli, and H Yildirim Erbil. Diffusion-controlled evaporation of sodium dodecyl sulfate solution drops placed on a hydrophobic substrate. *Journal of colloid and interface science*, 362(2):524–531, 2011.

[43] Jung-Hoon Kim, Sung Il Ahn, Jae Hyun Kim, Jong Soo Kim, Kilwon Cho, Jin Chul Jung, Taihyun Chang, Moonhor Ree, and Wang-Cheol Zin. Evaporation of sessile droplets of dilute aqueous solutions containing sodium n-alkylates from polymer surfaces: Influences of alkyl length and concentration of solute. *Langmuir*, 24(20):11442–11450, 2008.

[44] Qingfeng Yan, Li Gao, Vyom Sharma, Yet-Ming Chiang, and CC Wong. Particle and substrate charge effects on colloidal self-assembly in a sessile drop. *Langmuir*, 24(20):11518–11522, 2008.

[45] Manos Anyfantakis, Zheng Geng, Mathieu Morel, Sergii Rudiuk, and Damien Baigl. Modulation of the coffee-ring effect in particle/surfactant mixtures: the importance of particle–interface interactions. *Langmuir*, 31(14):4113–4120, 2015.

[46] Tadashi Kajiya, Wataru Kobayashi, Tohru Okuzono, and Masao Doi. Controlling the drying and film formation processes of polymer solution droplets with addition of small amount of surfactants. *The Journal of Physical Chemistry B*, 113(47):15460–15466, 2009.

[47] Alvaro Marin, Robert Liepelt, Massimiliano Rossi, and Christian J Kähler. Surfactant-driven flow transitions in evaporating droplets. *Soft Matter*, 12(5):1593–1600, 2016.

[48] E Kientz and Y Holl. Distribution of surfactants in latex films. *Colloids and Surfaces A: Physicochemical and Engineering Aspects*, 78:255–270, 1993.

[49] Merve D Doganci, Belma U Sesli, H Yildirim Erbil, Bernard P Binks, and Ibrahim E Salama. Liquid marbles stabilized by graphite particles from aqueous surfactant solutions. *Colloids and Surfaces A: Physicochemical and Engineering Aspects*, 384(1-3):417–426, 2011.

[50] Veronica L Morales, Jean-Yves Parlange, Mingming Wu, Francisco J Perez-Reche, Wei Zhang, Wenjing Sang, and Tammo S Steenhuis. Surfactant-mediated control of colloid pattern assembly and attachment strength in evaporating droplets. *Langmuir*, 29(6):1831–1840, 2013.

[51] Merve D Doganci and H Yildirim Erbil. Shape and diameter control of c60 fullerene micro-stains by evaporation of aqueous sds–fullerene dispersion drops. *Colloids and Surfaces A: Physicochemical and Engineering Aspects*, 432:104–109, 2013.

[52] Hua Hu and Ronald G Larson. Marangoni effect reverses coffee-ring depositions. *The Journal of Physical Chemistry B*, 110(14):7090–7094, 2006.

[53] Tim Still, Peter J Yunker, and Arjun G Yodh. Surfactant-induced marangoni eddies alter the coffee-rings of evaporating colloidal drops. *Langmuir*, 28(11):4984–4988, 2012.

[54] Xin Zhong and Fei Duan. Surfactant-adsorption-induced initial depinning behavior in evaporating water and nanofluid sessile droplets. *Langmuir*, 31(19):5291–5298, 2015.

[55] AR Harikrishnan, Purbarun Dhar, Prabhat K Agnihotri, Sateesh Gedupudi, and Sarit K Das. Correlating contact line capillarity and dynamic contact angle hysteresis in surfactant-nanoparticle based complex fluids. *Physics of Fluids*, 30(4):042006, 2018.

[56] AR Harikrishnan, Purbarun Dhar, Prabhat K Agnihotri, Sateesh Gedupudi, and Sarit Kumar Das. Wettability of complex fluids and surfactant capped nanoparticle-induced quasi-universal wetting behavior. *The Journal of Physical Chemistry B*, 121(24):6081–6095, 2017.

[57] Xiaoxiao Shao, Fei Duan, Yu Hou, and Xin Zhong. Role of surfactant in controlling the deposition pattern of a particle-laden droplet: Fundamentals and strategies. *Advances in colloid and interface science*, page 102049, 2019.

[58] Kedar Joshi and James F Gilchrist. Effect of added surfactant on convective assembly of monosized microspheres. *Applied Physics Letters*, 116(8):083702, 2020.

[59] James G Berryman. Random close packing of hard spheres and disks. *Physical Review A*, 27(2):1053, 1983.

[60] Alexander F Routh and William B Russel. Horizontal drying fronts during solvent evaporation from latex films. *AIChE Journal*, 44(9):2088–2098, 1998.

[61] Xuefeng Xu and Jianbin Luo. Marangoni flow in an evaporating water droplet. *Applied Physics Letters*, 91(12):124102, 2007.

[62] Alejandro Cifuentes, Jose L Bernal, and Jose C Diez-Masa. Determination of critical micelle concentration values using capillary electrophoresis instrumentation. *Analytical Chemistry*, 69(20):4271–4274, 1997.

[63] C Bonnet-Gonnet, L Belloni, and B Cabane. Osmotic pressure of latex dispersions. *Langmuir*, 10(11):4012–4021, 1994.

[64] Chourouk Mathlouthi. *Étude des propriétés thermodynamiques et dynamiques des polymères confinés en géométrie nanoparticules*. PhD thesis, 2016.

[65] Jacob N Israelachvili. *Intermolecular and surface forces*. Academic press, 2011.

Chapter 5

General conclusion

In this work we have introduced a fast and simple method for producing ordered surface morphologies via evaporation of polymer colloidal suspensions by time modulating the drying rate. These processes were carried out by drying suspensions of PS, PBA formed by suspension of hard and soft particles of PS, PBA and their mixture. The ionic strength of these suspensions was highly controlled by first well cleaning these suspensions from all ionic strength, surfactant, and then control it by adding this ionic strength or surfactant if necessary. First of all, the drying rate, the dynamic of drying front, and structure of the surface morphology were investigated in free air and under extensive airflow. This processes were investigated under time modulating airflow. A system was built to control the air flow by stopping and blown air periodically. In the first part, the drying rate was investigated under free air, blown air, and periodically blown air. Blown air on these suspensions was found to enhance the drying rate in which the drying rate increases as the airflow rate increases. We showed that the magnitude of drying rate depends on the amount of fraction of opening and closing time.
In very low ionic strength and in the absence of SDS the effect of periodic air flow on the 3D surface morphology and dynamic of drying front were investigated in PS, PBA, and their blends. We have shown that periodic surface structure are formed when we blow air periodically. These structures were found to be highly periodic and depend on the period of opening and closing time τ_p. The height of these profiles ranged between (0.1 and 1.1) μm. We showed that the dynamic of the drying front was also found to be enhanced by drying rate during the periodic airflow. The drying front was found to move in a periodic way; it advances during airflow and almost arrest when airflow stops. This was found to yield a fine control of the moving and arrest of the drying front and consequently the magnitude of particle deposition in each regime. These structures were predicted via a model which takes into consideration the kinetic of the particle deposition and the dynamic of drying front. The solid concentration profile and the height of the profile were estimated at different times and radial position based on the mass conservation laws. The general tendency of the observed moving and arrest of the drying

front and the resulting surface morphologies were predicted using such model. The 3D perioding structure is also predicted with this simple model to a great extent and particularly reproduce the dependence of the height profile on the period of τ_p.
Second, we investigated the roles of surfactant on the dynamic of drying front and the resulting 3D surface morphology. We show that adding aliquots of sodium dodecyl sulfate (SDS) affects the drying front dynamic under a modulated drying rate as well as the resulting surface morphology. Furthermore, the onset and the first line of drying front was found to advance with a velocity, which decrease with increasing [SDS]. On the other, the endset (second line) of the drying front was found to advance rapidly during airflow and recedes back to the onset line once the airflow stops. These dynamics were found to follow a similar tendency of the surface tension which suggests that the surface tension plays a significant role in this process. We attributed this mechanism to several possible effect such as Marangoni effect, distinction between drying front and irreversible front, contact angle variation. The reduction of surface tension at the front create surface tension gradient which in turns initiates Marangoni effect and a reverse flow toward the center. Further, increasing [SDS] at the drying front during air flow reduces the contact angle. This could interpreted as fast movement of the drying front. When air stops, the SDS redistribut imposed by Osmotic pressure leading to a return of the contact angle to its initial state and generate a receding of the drying front. Further, presence of SDS in the suspension can lead to particles stabilization, in this case during high drying rate, the irreversible zone lags behind the drying front. Therefore, once air stops, the zone located between the drying front and the irreversible zone redisperese again which generate a receding in the drying front.
Furthermore, we have investigated the effect of ionic strength on surface periodicity under time modulating the drying rate. Presence of salt such KCl in the colloidal suspension plays important role on the deposition patterns. The drying front was found to move in almost periodic way leading to generate 3D surface morphology similar to that observed during drying the cleaned suspension.
Although we have investigated the effect of particles concentration and particles size on the particles deposition behavior under periodic airflow. In the case of particles concentration, we found that changing the concentration of the particles does not effect the periodicity and exhibit a periodic structure surface. While increasing the particles size in the suspension up to 4 times was found to enhance the particles deposition leading to generate a more uniform film.